Mn_{12}-ACETATE THIN FILM PATTERNS AND THEIR INTERACTION WITH SUPERCONDUCTORS

A Dissertation

by

KYONGWAN KIM

Submitted to the Office of Graduate Studies of
Texas A&M University
in partial fulfillment of the requirements for the degree of

DOCTOR OF PHILOSOPHY

December 2007

Major Subject: Physics

Mn_{12}-ACETATE THIN FILM PATTERNS AND THEIR INTERACTION WITH SUPERCONDUCTORS

A Dissertation

by

KYONGWAN KIM

Submitted to the Office of Graduate Studies of
Texas A&M University
in partial fulfillment of the requirements for the degree of

DOCTOR OF PHILOSOPHY

Approved by:

Chair of Committee,	Winfried Teizer
Committee Members,	Valery Pokrovsky
	Joseph Ross
	Mosong Cheng
Head of Department,	Edward Fry

December 2007

Major Subject: Physics

ABSTRACT

Mn_{12}-acetate Thin Film Patterns and Their Interaction with Superconductors.

(December 2007)

Kyongwan Kim, B.S., Dankook University;
M.S., Dankook University
Chair of Advisory Committee: Dr. Winfried Teizer

Mn_{12}-acetate single-molecule magnets (SMMs) are nano-scale magnets showing a strong magnetic anisotropy, slow relaxation and stepwise magnetic hysteresis curves. Possible applications of Mn_{12}-acetate, e.g. for ultra high density magnetic information storage device, quantum computation, and magnetic molecular electronics, have been suggested due to the unusual magnetic behavior. It is an important prerequisite for the applications to develop a reliable technique to organize the molecules on a surface and to detect the magnetic signals of the molecules. A solution evaporation technique combined with conventional lithography is a simple but reliable method to create Mn_{12}-acetate thin film patterns on the micro/nano-scale. The method is demonstrated with a series of analysis.

A superconducting quantum interference device (SQUID) shows a non-linear I-V (Current vs. Voltage) characteristic that is modulated by a magnetic flux inside the loop, allowing one to sense and analyze an extremely weak magnetic field. The miniaturized SQUID is appropriate for sensing the magnetic flux from the film structure of the

molecular magnets. Theoretical ideas, fabrication, and a measurement technique of the device are presented.

A new interesting system, the so-called superconductor/SMM hybrid, results from the experimental configuration. Understanding this new type of hybrid system is important not only because of the expectation of new phenomena affecting the functionality of superconducting devices, but also because the two coupled substances are fundamentally incompatible phases. The first experimental attempt to investigate the interaction between an aluminum superconducting film and Mn_{12}-acetate SMMs will be discussed.

ACKNOWLEDGMENTS

I sincerely appreciate the encouragement, guidance and support of Dr. Winfried Teizer, chair of my committee, who has been my research adviser. I would also like to thank Dr. Valery Pokrovsky, Dr. Joseph Ross, Dr. Artem Abanov, and Dr. Mosong Cheng for serving on my dissertation committee. I wish to thank Dr. Kim Dunbar and Dr. Hanhua Zhao for providing Mn_{12}-acetate original powder, which is one of the crucial parts of my research. Dr. Glenn Agnolet's advice on cryogenic systems is kindly appreciated. I also wish to thank my labmates for their helpful comments on my research. Especially, I thank Dr. V. Meenakshi for her advice on AFM, XPS, and SQUID magnetometry experiments, Dongmin Seo for his advice on AFM experiment and the solution evaporation technique, Joel Means for his advice on photolithography and cryogenic systems, Arlene Ford for her advice on e-beam lithography and Huachun Xu for his advice on thermal evaporator and e-beam lithography. My thanks are extended to my fellow graduate students, Han-gil Lee and Eunsin Lee, who helped me with their encouraging discussions. Finally, I would like to give my special thanks to my parents, Mr. Dae-sung Kim and Ms. Ok-sun Lee, and my sisters, Ms. Min-jung Kim and Ms. Joo-yeon Kim. Their invisible hands to encourage me and their love have been an impetus to my endeavor for completion of this work.

TABLE OF CONTENTS

LIST OF FIGURES

FIGURE Page

FIGURE Page

FIGURE Page

FIGURE Page

LIST OF TABLES

CHAPTER I

INTRODUCTION

Magnets are very familiar materials that are used in every day life. Since the invention of the compass, the first practical use of a magnet in history, there have been numerous devices produced with many practical applications in the area of magnetism such as sensors, switches, motors, phones, vehicles which run levitated on their track due to a magnetic force, and memory storage devices containing magnetic film patterns which are some of the most widely used commercial examples of the use of magnets to date. In memory devices, a small area of a magnetic film, the so-called domain, is oriented along one particular direction by an external source. The aligned domain maintains its orientation as long as it is not modified by additional effects, memorizing the orientation. It is very similar to a character written on a paper using a pencil in the sense that the character is preserved as long as it is not erased and the paper is not contaminated. Increasing the storage capacity of devices has been an issue since there is a need for greater efficiency in them. As the smallest letter which is still visible leads to a sheet of paper containing the maximum information within its limited size, the smallest area, which is well defined in magnetic ordering, could achieve the maximum magnetic storage capability in principle. However, there has been a convergent opinion that miniaturizing of continuous magnetic domains will face a physical limit and therefore

---

This dissertation follows the style of Physical Review Letters.

discretely well defined small magnets should be employed in order to enable the storage density to be extended beyond the current limit. This issue is not only about the magnetic storage capability, but also about the effect on the development of various kinds of micro/nano-devices that use magnetic elements. Due to the rising concern it has been a common topic to develop small discrete magnetic units and to study the magnetic behavior of these units for the understanding of the basics of magnetism as well as for the next generation of magnetic devices.

Single molecular magnets (SMMs) are nanoscale magnetic particles. As will be described in the next chapter in detail, they have a high spin magnetic moment in the ground state and a high zero-field splitting due to strong magnetic anisotropy. In other words, these molecules are locked in one of the lowest spin energy states at low temperatures exhibiting a high magnetic moment. SMMs also have negligible magnetic interference with each other. These general properties of SMMs allow one to consider them as candidates for being the smallest discrete magnetic units for future devices. In addition, SMMs are also useful specimens for scientists to study fundamental phenomena, which are not understood without including quantum mechanical behavior. Because it is possible to control the size of the SMM crystal structure, where all the magnetic properties of the molecules are identical, the quantum behavior happening in the crystalline system which, coupled with macroscopic devices, yield measurable signals. Most importantly, scientists have observed interesting characteristics, such as steps in magnetic hysteresis curve, which are caused by quantum tunneling of the magnetization.

Although SMMs are novel materials for fundamental studies and have various applications in principle, there are still many barriers to overcome for practical uses of them. The temperature range where these molecules are locked in a stable magnetic state is still too low to make them easily accessible in an ambient environment. In addition, a reliable technique to manipulate and sense the magnetic state of the molecules is needed as well as a technique to position the molecules on a substrate. The main theme of this thesis will be focused on the attempts to work out the challenges pointed out above, including minimization of the area in which SMMs are localized and development of superconducting quantum interference devices (SQUIDs) on the micro/nano scale, which are appropriate for identifying of the magnetic signals from the small magnetic elements. In addition, this thesis will also investigate the influence of SMMs on the properties of superconducting films. This study of SMMs/Superconductor coupled systems is another important subject especially when they are comparable in size scale because this type of coupled structure appears when SMMs are put on miniaturized SQUIDs for further research.

This thesis is composed of a total of six chapters, starting with this introduction. Chapter II will describe the basic background of Mn_{12}-acetate, one of the most widely studied SMMs. The structure of the molecule will be introduced and some notable experimental results will be summarized to give the reader a general idea of the magnetic object.

Chapter III will contain methods to pattern thin films of Mn_{12}-acetate, at the micro and the nano scale. Conventional lithography techniques, such as photolithography and

electron beam lithography (EBL) are combined with a solution evaporation technique. This technique is one of the most robust methods developed to deposit Mn_{12}-acetate thin films in our lab in recent years. The motivation and a complete procedure for patterning the thin films will be described in the first two sections. Because EBL requires a more complicated method to engrave a resist material, which is a crucial step of the patterning work, than photolithography, the third section has been focused on the demonstration of EBL in some detail. The resulting samples are analyzed using atomic force microscopy, X-ray photoelectron spectroscopy, and superconducting quantum interference magnetometry in the last section.

Chapter IV will treat the development of miniaturized SQUIDs. SQUIDs are very useful devices for measuring the magnetic films. A SQUID consists of a superconducting loop which includes two weak-links. When a supercurrent flows along the loop in the presence of magnetic field, there are two significant factors that cause a change in the phase of the electron-pair wave. The first is the tunneling process of the paired electrons through the weak-links and the other factor is the phase shift caused by a magnetic flux penetrating through the loop produced by external magnetic sources. However, a quantum mechanical condition imposes a strong fundamental restriction on the overall phase changes that the total phase difference around any closed superconducting loop must equal to 2π multiplied by any integer. Therefore, as the magnetic field changes, a supercurrent circulating along the loop will be induced in order for the quantum condition to be fulfilled and, as a consequence, less energy is required. The current flowing through the entire device, the so-called measuring current

is coupled with the induced current circulating along the loop. Because the magnetic flux penetrating through the loop modulates this circulating current, the critical measuring current is related to the flux. Hence, one can find a relationship between the critical measuring current and the magnetic flux. Therefore, when a small magnetic object is coupled with a SQUID, the magnetic state of the object can be analyzed by the flux analysis through the critical current measurements. The theoretical background for SQUIDs will be introduced in the first section of Chapter IV and, in the second section, the fabrication of the thin film devices made of aluminum, and measurement technique and analysis will be demonstrated. An approach to make SQUIDs coupled with Mn_{12}-acetate will be also introduced for an investigation of the magnetic properties on the lithographically defined Mn_{12}-acetate film structure. Cryogenic systems for low temperature experiments and a flexible range of magnetic fields are essential for the analysis of SMMs, aluminum SQUIDs, and SMM/Superconductor coupled systems. Therefore, this thesis will discuss how two systems, one with a 1K-pot pumping system and the other with a dilution refrigerator, aided in taking these measurements with a superconducting magnet attached to each system in the last section.

As mentioned earlier, this thesis will also emphasize additional work, which is an extension of the main focus. If one chooses SQUIDs as a tool to study the behavior of SMMs, then the SMMs have to be in close proximity to the superconducting devices somehow. It is worth considering the interaction between SMMs and superconductors when they are close to each other because this coupled aspect is a significant configuration in a micro/nano-SQUIDs measurement. There may be new interesting

phenomena, which may occur from the possible interaction between the magnetic material and the superconductor due to the magnetic flux in the magnetic system and supercurrents in the superconductors. Recent experimental work in identifying new possible phenomena in coupled systems will be covered in Chapter V. Elementary properties of aluminum superconducting films, for instance, critical currents, critical temperatures, and critical fields are measured for a comparative analysis with the results from the aluminum films coupled with SMMs. For the coupled system, SMM films are deposited on/underneath patterned aluminum films, which are parameterized by size and thickness. A preparation of the samples and analysis of the results will be discussed.

The last chapter will deliver the main purpose of this dissertation once more as a means of reminder and organize the entire plot of the research with a summary and conclusion. Issues and problems derived from this work will be also mentioned in the chapter as references for further research.

CHAPTER II

Mn_{12}-ACETATE SINGLE MOLECULAR MAGNETS

Single Molecular Magnets (SMMs) [1-6] are clusters composed of magnetic elements, such as Mn, Fe, and V, that are coupled via bridging atoms. The coupled magnetic cores are surrounded by organic ligands which lead the bond to form the clusters and protect them from additional chemical growth. SMMs have a large spin magnetic ground state, and the magnetic sublevels are split by strong magnetic anisotropy (~62K for Mn_{12}-acetate [2]) yielding magnetic bistability, which is the most important feature for the application as magnetic information storage systems. In addition to the properties the clusters have very weak magnetic interaction between themselves [7]. Due to those typical characters of SMMs it has been proposed to consider them as a potential candidate for the smallest discrete magnetic units for future application of magnetic devices. In chemically synthesized crystal structures SMMs are arranged with equally oriented easy axes along which the spin magnetization of the magnetic molecule is energetically favorable to be aligned. This orientation of the magnetic crystal gives an advantage in controlling the size of the magnetic system without disturbance of magnetic properties of each molecule allowing the study of molecular magnetism in various ranges of system size.

Mn_{12}-acetate is one of the most thoroughly studied SMM to date. This molecule was introduced by Lis in 1980 for the first time [1]. The complete chemical formula is $[Mn_{12}O_{12}(CH_3COO)_{16}(H_2O)_4]\cdot 2CH_3COOH\cdot 4H_2O$. As depicted in Fig. II-1, the

crystalline complex has a tetragonal lattice, with $a = b = 1.7319$ nm, $c = 1.2388$ nm and a crystal lattice belonging to the S_4 crystallographic symmetry group, which contains a 4-fold rotation-reflection symmetric axis. In the figure the circles are drawn with two different gray tones to describe the symmetry group (S_4) of the lattice.

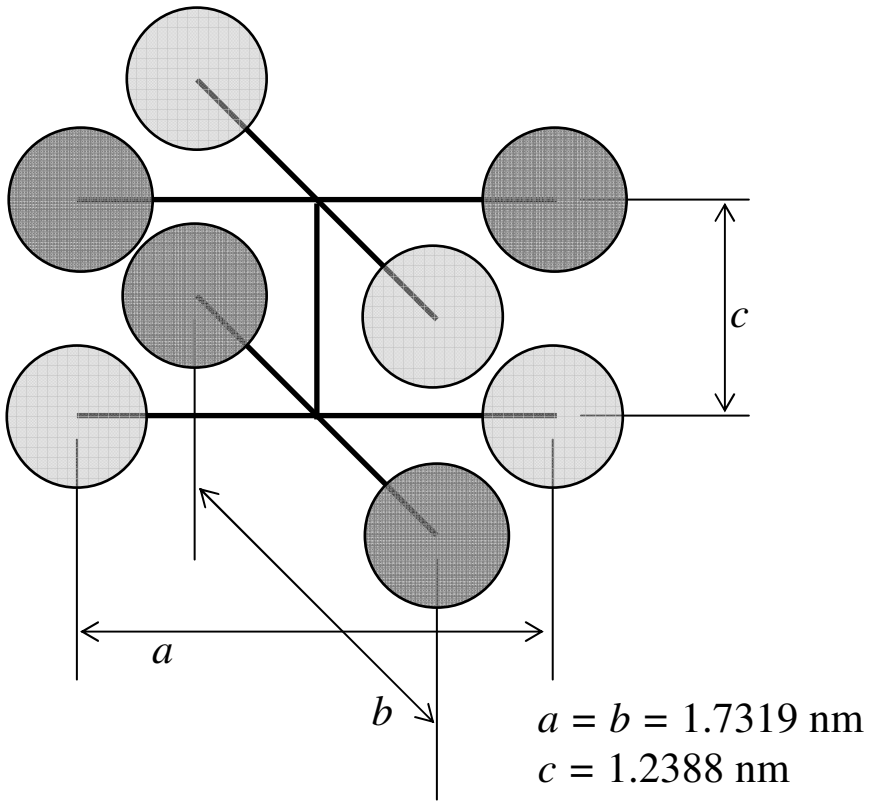

Fig. II-1. Crystal lattice of Mn_{12}-acetate complex with lattice constants.

The magnetic core of Mn_{12}-acetate cluster comprises twelve manganese ions and twelve bridging oxygen ligands. The structure of the core is depicted in Fig. II-2. Four manganese

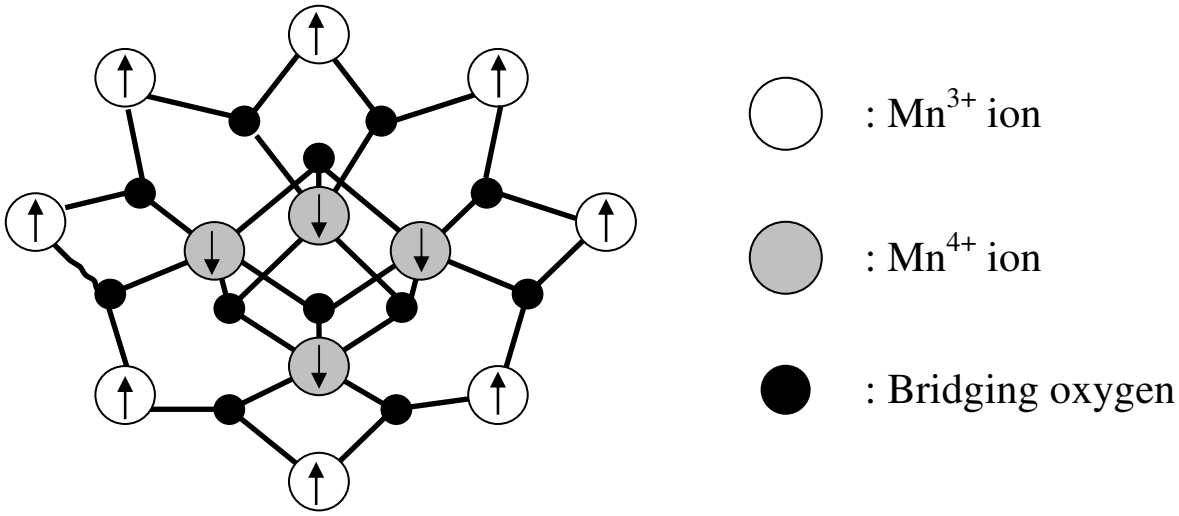

Fig. II-2. Magnetic core structure of Mn_{12}-acetate cluster. The arrows in the circles indicate a configuration of the direction of the effective spin magnetic moments of the ions at ground state.

ions (Mn^{4+}) are coupled via four bridging oxygens forming the central tetrahedron. The basic electron configuration of Mn^{4+} is $3d^3$ and the three electrons in the shell define the effective spin of the ion as 3/2. Eight manganese ions (Mn^{3+}) surrounding the central structure are coupled with the Mn^{4+} ions via either one or two bridging oxygens depending on the site of the ion. The electron configuration of Mn^{3+} is $3d^4$ and the four

electrons in the shell define the effective spin of the ion as 2. Mn^{3+} and Mn^{4+} are antiferromagnetically coupled through the superexchange interaction mediated by the electrons of the oxygen atoms. The effective spins of the ions and the antiferromagnetic coupling give a total spin S_T=10 of the ground state. As shown in Fig. II-3 a total of 16 acetate ligands are involved to bridge the eight outer manganese ions and to link them to

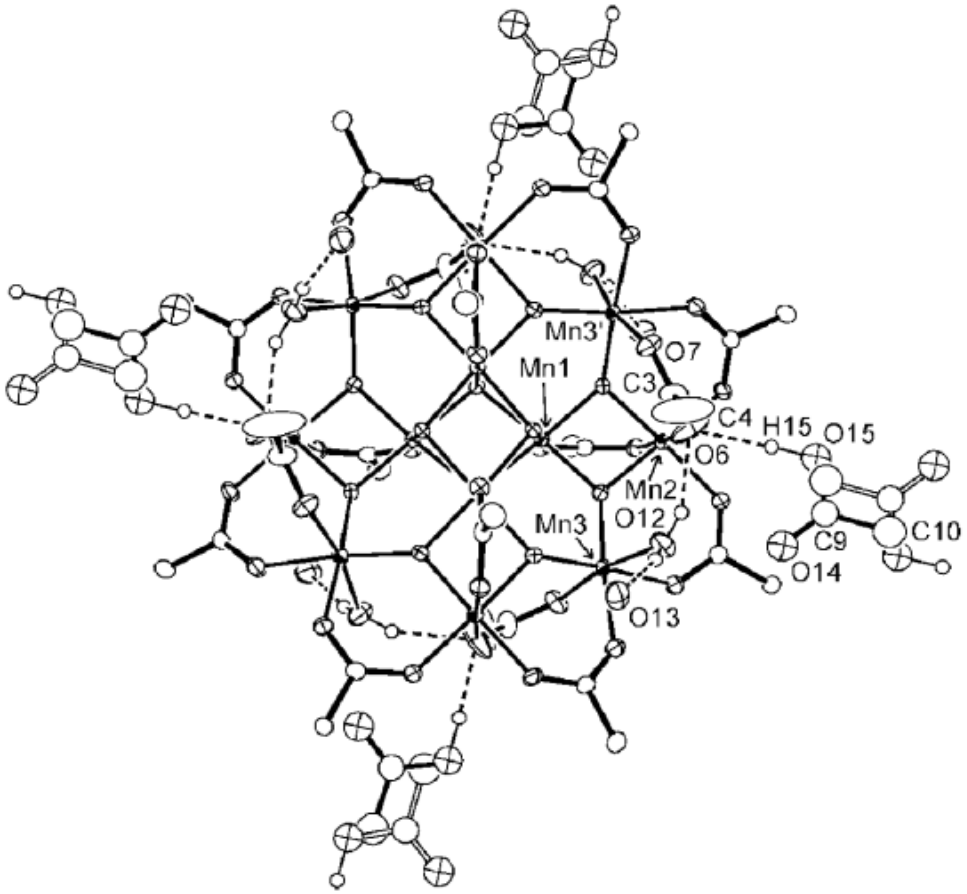

Fig. II-3. Crystal structure of Mn_{12}-acetate (from ref. [6])

the four inner manganese ions, thus protecting the magnetic core of the Mn_{12}-acetate cluster. In addition, four water molecules [Fig. II-3] are connected to four manganese ions among the eight outer ions completing the core molecules described in the square bracket of the full chemical formula above. These core molecules with four water of hydration and two acetic acid molecules build up the overall crystals.

Stepwise magnetization hysteresis curves are one of the fascinating phenomena measured on Mn_{12}-acetate samples [8-12]. Sudden increases and decreases of magnetization indicated in the steps appear in the hysteresis loops cycled at different temperature. All these transitions of magnetization are observed at specific values of magnetic fields. This unusual phenomenon has been explained by thermally assisted quantum tunneling of magnetization [10]. A simple Hamiltonian for the spin *S* system in the presence of an applied magnetic field is given by

$$\hat{\mathrm{H}} = -D\hat{S}_z^2 - g\mu_B \hat{\vec{S}} \cdot \vec{H} \qquad \text{(II-1)}$$

where *D* is the anisotropy energy constant, and *g* is the gyromagnetic factor, or the *g*-factor. μ_B is the Bohr magneton and *H* is the applied magnetic field. Thus, if the applied magnetic field is parallel to the easy axis, the energy eigenvalues for two states, $|S,m\rangle$ and $|S,-m+n\rangle$ are given by $\left(-Dm^2 - g\mu_B mH\right)$ and $\left\{-Dm^2 + Dn(2m-n) + g\mu_B H(m-n)\right\}$, respectively. By equating them to each other we find that the two energy values are identical at the magnetic field $-\frac{Dn}{g\mu_B}$ (~0.42*n* T [13]). In the simplest situation of the

equation II-1, when there is no applied field all the pairs of energy states, e.g. $S_z = 10$ and $S_z = -10$, $S_z = 9$ and $S_z = -9$,… $S_z = 1$ and $S_z = -1$, are identical providing the most probable configuration of resonance tunneling events. As a magnetic field that is parallel to the easy axis is applied a mismatch between the energy states happens suppressing the tunneling. However, when the applied field reaches the value $-\frac{Dn}{g\mu_B}$, the energy states are identical and tunneling occurs again. Therefore, the sudden changes of relaxation resulting in the resonance tunneling are observed as steps in the hysteresis curve at these magnetic fields. Because of the thermal distribution of spin states, the resonance tunneling process depends on the temperature and this fact is explained by the tendency of the relaxation of spins at the resonance field, which is observed differently at the different temperatures.

Slow relaxation of the magnetization is another important feature of the Mn_{12}-acetate. A peak observed in an out-of-phase component of AC-susceptibility, χ", is experimental evidence of the slow relaxation [14]. If the applied field has an ac modulation with a frequency of ω, the real (in-phase) and the imaginary (out-of-phase) components are given by,

$$\chi' = \chi_S + \frac{\chi_T - \chi_S}{1+\omega^2\tau^2} \quad \text{and} \quad \chi'' = \frac{(\chi_T - \chi_S)\omega\tau}{1+\omega^2\tau^2} \tag{II-2}$$

respectively, where $\chi_S = \chi_{\omega\to\infty}$ is the adiabatic susceptibility, $\chi_T = \chi_{\omega\to 0}$ the isothermal susceptibility, and τ is the spin-lattice relaxation time [14]. The first derivative of χ''

with respect to $\omega\tau$ becomes zero when $\omega\tau = 1$ and the second derivative is negative at $\omega\tau = 1$. Therefore, χ'' has a maximum at $\omega\tau = 1$, so the relaxation time is estimated from a peak in the out-of-phase susceptibility. It has been seen that below 2.0K τ becomes of the order of months and that at 1.5K it reaches to about 50 years [15].

In the next chapter a simple and reliable technique to fabricate Mn_{12}-acetate film patterns at the micro/nano scale will be explained, starting from a motivation that is based on the novel magnetic properties described in this chapter.

CHAPTER III

FABRICATION OF Mn_{12}-ACETATE FILM PATTERNS*

Motivation

There have been possible applications of SMMs suggested due to the unusual magnetic behavior [16-19]. Although the blocking temperatures of the SMMs are too low for practical applications, such as ultrahigh density memory storage and quantum computing, as these particular projects have a long term plan, it is an important task to develop a reliable way to create a pattern of the molecules on an intended area and to detect the magnetic signals of each addressed pattern of molecules keeping pace with the progress in synthesizing molecules. Besides the practical use of SMMs, fundamental study, such as electron tunneling phenomena through a small magnetic unit has required well defined magnetic systems like separated SMMs [20-22]. With this general goal, several methods for fabricating thin films and ordered patterns of SMMs on various surfaces have been reported by other groups [23-31]. A few methods of depositing Mn_{12}-acetate on Si/SiO_2 have been found by our group. Pulsed laser deposition (PLD) [32, 33] and matrix assisted pulsed laser evaporation (MAPLE) [33] techniques were employed to reduce thermal decomposition of the SMM structures.

---

*Part of this chapter is reprinted with permission from "Nanopatterning of Mn_{12}-acetate Single-Molecule Magnet Films" K. Kim et al, (2007). *Journal of Applied Physics.* 102, 094306, Copyright © 2007 American Institute of Physics and "Mn_{12}-acetate Film Pattern Generated by Photolithography Methods" K. Kim et al, (2004). *Applied Physics Letter*. 85, 3872, Copyright © 2004 American Institute of Physics

It is known that Mn_{12}-acetate decomposes at ~400K [1], therefore using a conventional evaporation technique, such as thermal evaporation, will not produce a high quality thin film sample. The matrix in the MAPLE technique serves as an additional thermal absorber in the prepared target leading to an even milder evaporation than the PLD technique. Another method studied in our group is the solution evaporation technique [34]. Surface analysis of the resulting film samples revealed that the dissolved Mn_{12}-acetate powder in the solvent remained after all the solution was dried, forming a few molecular layers on a substrate. These techniques to generate Mn_{12}-acetate films can be in principle combined with modern conventional lithography techniques, including photolithography and electron beam lithography (EBL), to create patterns that range in size down to a few tens of a nanometer. This approach of using lithography is more useful than the other methods to organize SMMs since lithographic techniques can be utilized to fabricate advanced devices. In the next section the detailed procedure for the patterning that we used will be demonstrated.

Micro/Nano-fabrication of Mn_{12}-acetate film patterns

Photolithography is a process that selectively removes a segment of photoresist material. As the photoresist material is a light-sensitive polymer, the process is attained by transferring light to the photoresist layer through a photomask, which has a desired pattern that is partially blocked from the light. A series of chemical treatments strips off the part of the starting resist that was either exposed or not-exposed to the light depending on the type of the resist material. Therefore, this technique produces a

selectively exposed Si/SiO_2 surface for the Mn_{12}-acetate film pattern. The detailed process for the patterning using photo-lithography is shown in Fig. III-1. In order to get a clean Si/SiO_2 surface used to fabricate film pattern, a rectangular piece, diced from a silicon wafer was sonicated in acetone and 2-propanol sequentially prior to patterning.

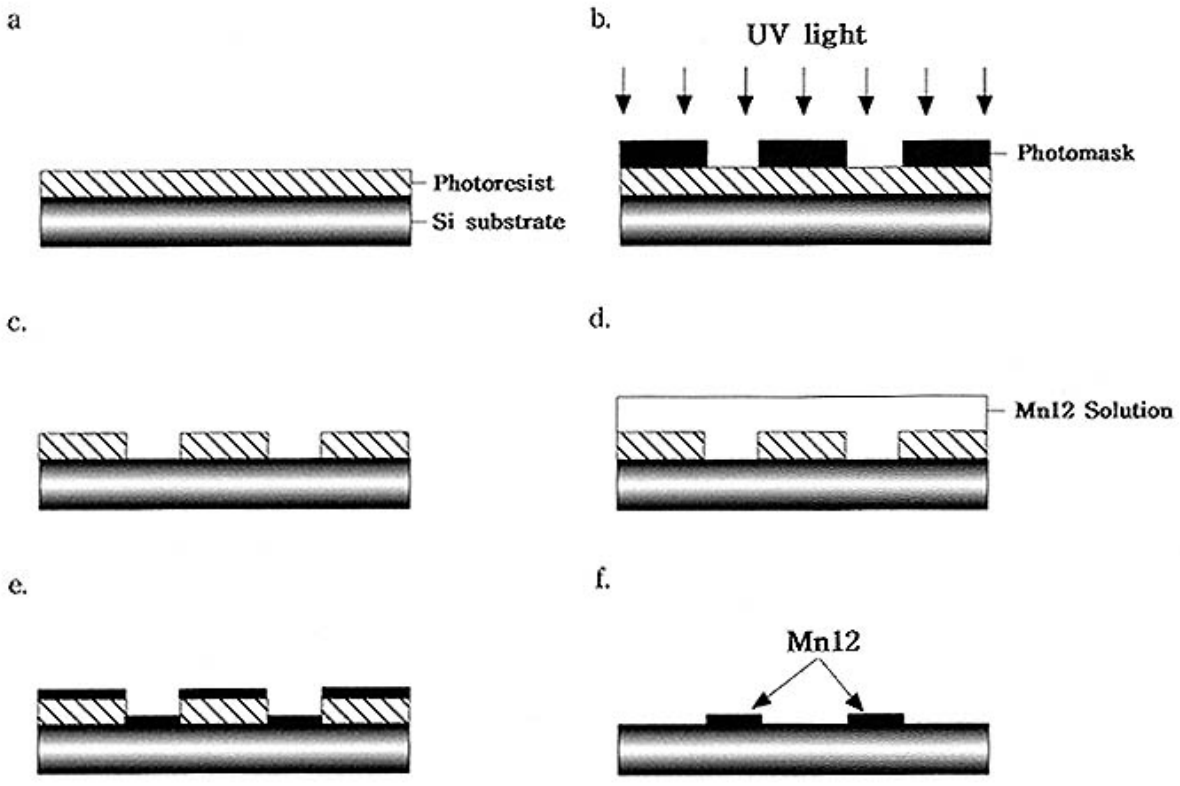

Fig. III-1. Schematic diagram describing the patterning of the Mn12-acetate film using photolithography and solution evaporation method.

Acetone was sprayed onto the surface immediately after the piece was picked out from the acetone bath, then the piece was sprayed with 2-propanol immediately after the piece was picked out from the 2-propanol bath. The wet substrate was fully dried with a N_2 gun. Next, a layer of resist material, SU-8-2002 for photolithography, was spin-coated onto the substrate. SU-8-2002 was coated at 3000rpm for 60s resulting in ~1200nm-thick layer. The photoresist layer was exposed to uniform UV light through a photomask for 50s. After development of the photoresist layer in the SU-8 developer (MICROCHEM), de-ionized water was sprayed on the surface. The resulting sample has the selectively exposed Si/SiO_2 surface as shown in Fig. III-1 (C). A prepared solution ($2\times10^{-4} mol \cdot l^{-1}$ of Mn_{12}-acetate in 2-propanol) was added dropwise to the patterned surface using a pipette. The liquid film was then dried in air. Finally, a lift-off of the resist material using a photoresist remover (MICROCHEM), resulted in a Mn_{12}-acetate film pattern. An optical micrograph of the resulting film pattern reveals rectangular structures with widths greater than ~5μm [Fig. III-2].

EBL [35] is a conventional lithography technique that is used to generate sub-micron (down to ~20nm) patterns. Unlike photolithography that uses a mask for a selective transmission of light, EBL uses an electron beam to create a pattern directly on the surface of the resist. Therefore, the entire patterning procedure of EBL takes additional efforts. Since it requires a more involved process to engrave the resist material than photolithography, the next section will be used to describe the general scheme of EBL. Besides the means to selectively stimulate polymeric resist materials to get a patterned mask, the entire procedure to fabricate sub-micron Mn_{12}-acetate film structures

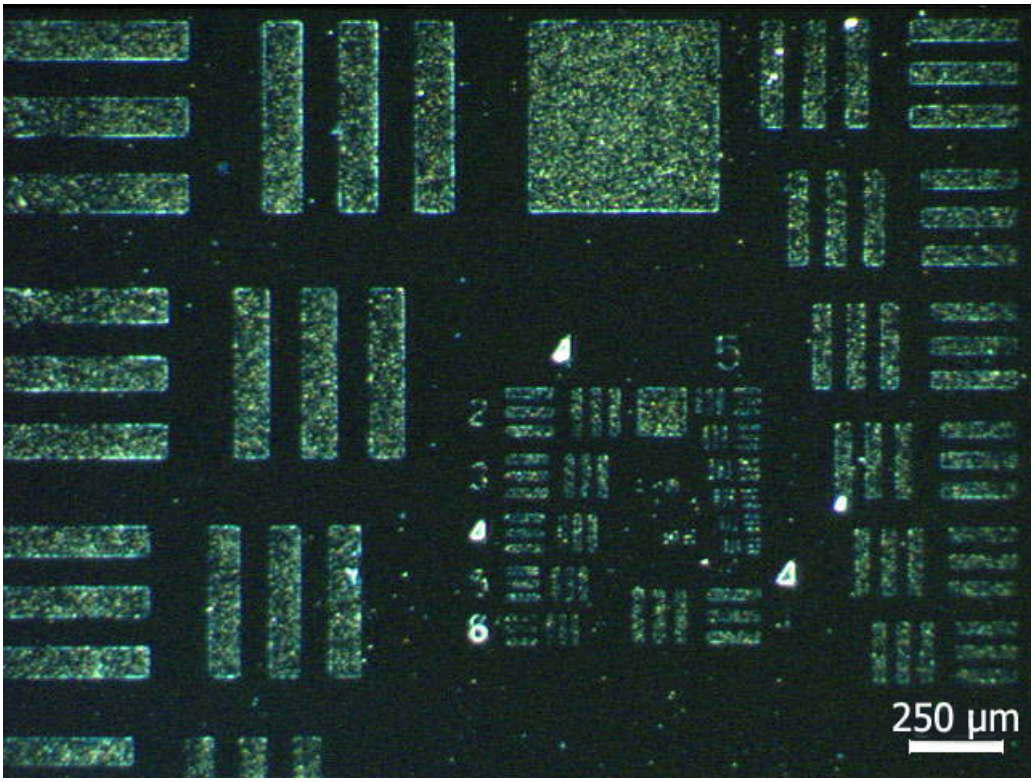

Fig. III-2. Optical micrograph of Mn_{12}-acetate film pattern.

is identical to the micro fabrication process. PMMA (polymethyl methacrylate), a polymer resin with a molecular weight of 950K (Monochlorobenzene, 3%), was spin-coated on the Si/SiO_2 substrate, which was prepared by the same cleaning process used in the previous work, at 4000 rpm for 50 s resulting in a ~200-nm-thick layer. The sample was then baked on a hot plate at 180 °C for 2 min. An electron beam of 30 kV was used to irradiate the surface of the sample to create the desired pattern. This procedure is different from the work done with photolithography since a sample was

exposed by a uniform UV light projected through a mask to develop the entire pattern at once. The sample was then dipped into the customary developer (1:3 Methyl Isobutyl Ketone/2-propanol) for 1 min and then rinsed in 2-propanol for 1 min. Next, a droplet of the prepared Mn_{12}-acetate solution (2.5×10^{-4} mol l^{-1} of Mn_{12}-acetate in 2-propanol) was added onto the patterned surface using a pipette. The resulting liquid film on the surface was then dried in air. The dropping and drying process was repeated a total of 5 times to enhance the thickness of the Mn_{12}-acetate film. Finally, the sample was sprayed with CH_2Cl_2 to remove the majority of the PMMA film and then sonicated in CH_2Cl_2 for less than 1 min to remove the residual PMMA so that only the Mn_{12}-acetate film pattern remains on the Si/SiO_2 substrate (lift-off). The entire procedure was carried out in a clean room environment at ambient temperature. The entire procedure is depicted in Fig. III-3 with the resulting film pattern viewed through a scanning electron microscope (SEM). To maximize the clarity of the image, the sample was scanned at lower energy (10 kV). A magnified image of the line patterns [Fig. III-4] indicates a line width of ~50 nm, about 2 orders of magnitude smaller than the previous photolithographic patterns of Mn_{12}-acetate. As mentioned earlier, a detailed procedure for EBL will be demonstrated in the next sections as well as an in-depth analysis of the fabricated samples.

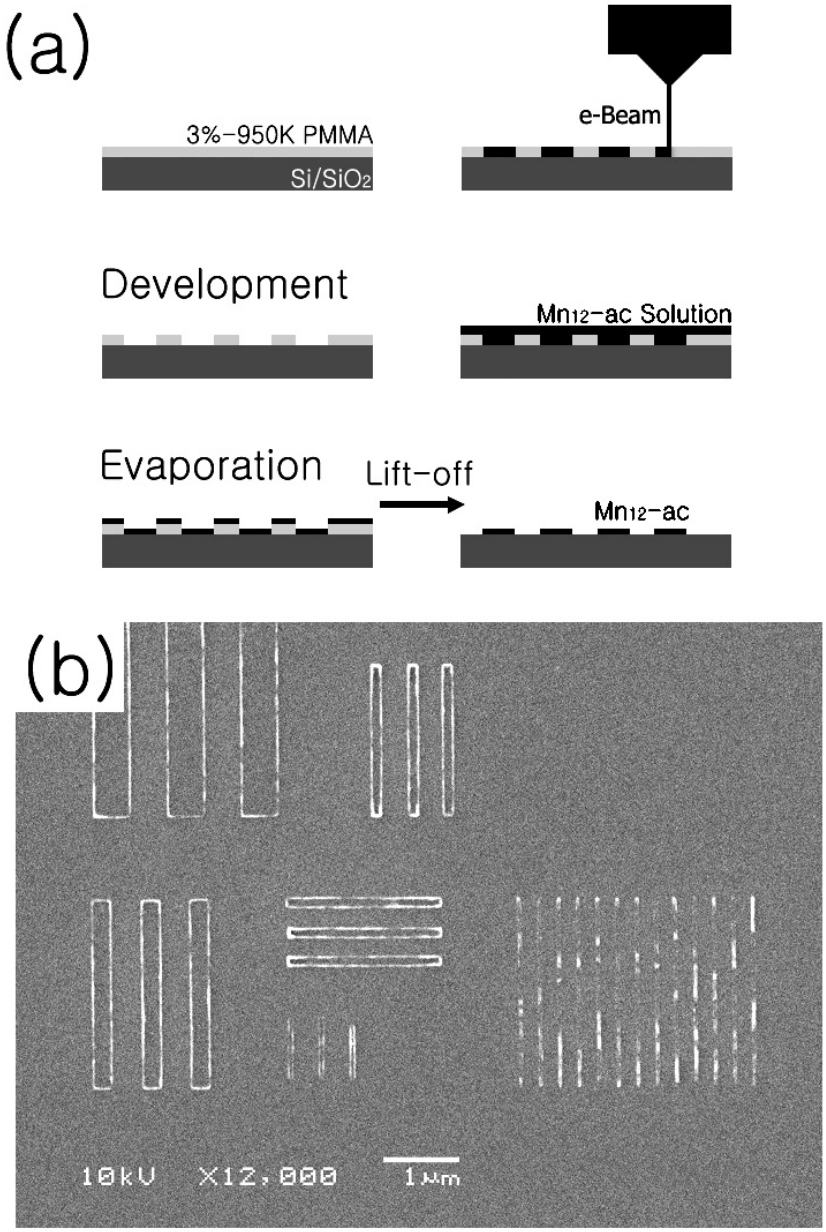

Fig. III-3. (a) Schematic diagram showing the patterning procedure used to make the Mn_{12}-acetate (single-molecule magnet) film. (b) SEM image of the submicron patterns generated by the procedure detailed in (a).

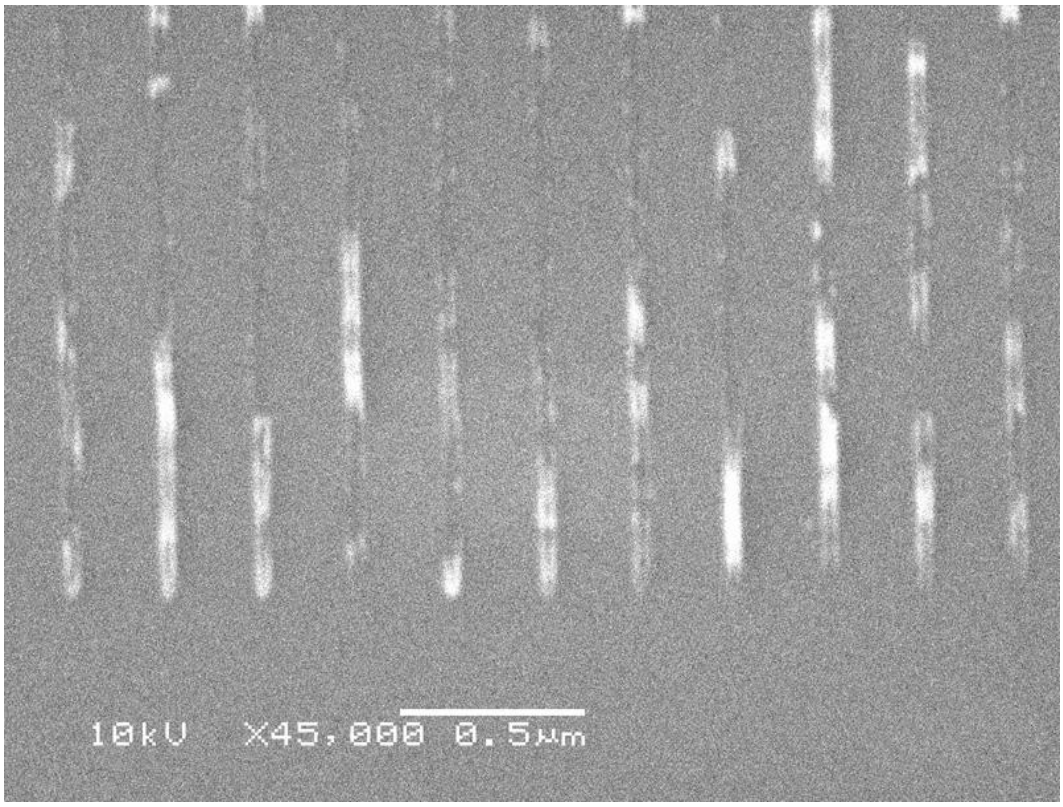

Fig. III-4. SEM image of the line pattern in Fig.III-3 (b) scanned at higher magnification.

Electron beam lithography

In this section the electron beam lithography procedure used to selectively inscribe a layer of PMMA on a substrate is introduced in detail. First, a substrate was cleaned according to the protocol presented in the previous section, and a pipette was used to place a few drops of liquid of 950K (Monochlorobenzene, 3%) PMMA onto the cleaned

substrate until the entire surface was covered with the liquid. The sample was then spun at 4000 rpm, for 50s. A line was scratched near the edges of the sample as a marker using sharp object like the tip of a razor blade as shown in Fig. III-5.

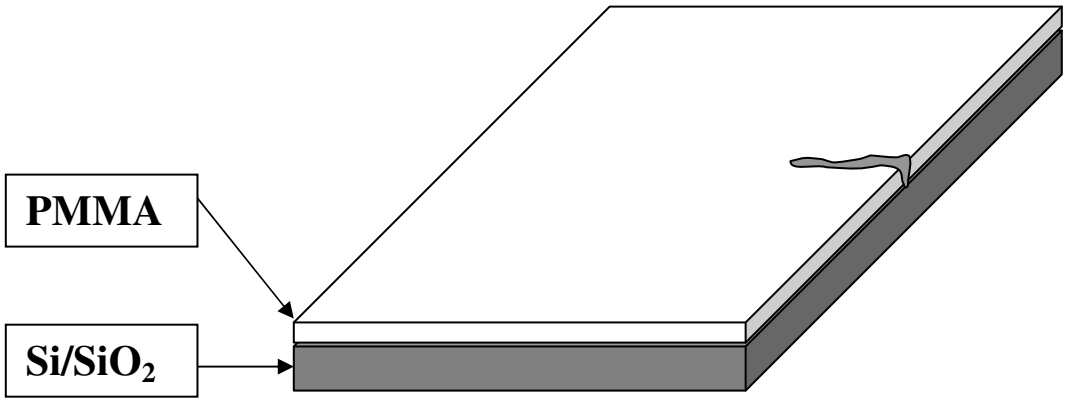

Fig. III-5. A scratch engraved on a sample as a marker.

The prepared sample was then mounted on a stage inside a vacuum chamber of a SEM (JEOL-JSM6460). To prevent an electric discharge in the assembly of the electron gun, the chamber was pumped down until the internal gauge detected a low enough pressure with its sensors. After pumping for an additional 10 min, the filament was turned on at the highest accelerating voltage of 30kV and a low beam spot size. In order

to obtain the best resolution, the largest accelerating voltage (30 kV) which has the shortest wave length of the electron beam was used, and a smaller diameter (~25, which is roughly corresponding to -10 pA beam current) of the beam spot was selected. The spot size for -10 pA varied with the status of the filament and the degree of the beam optimization. The beam was moved to the Faraday cup to adjust the beam status including saturating the filament, tilt and shift, and to measure the true value of beam current used in sample exposure. To saturate the filament the heating current was slowly increased while monitoring the beam current measured with a Keithley 6485 picoammeter. Once the beam current reached the plateau (saturation) over the first peak, the current through the filament was slightly decreased in order that the beam current stayed right below the saturation point. Tilt and shift were iteratively optimized by finding the maximum value of the beam current on a symmetrical distribution of the current. They were adjusted at a smaller (~25) and a bigger (~90) spot size, respectively. Under the optimal tilt and shift circumstance, spot size was then set to correspond to a beam current (-10 pA). The optimized beam was moved to the gold standard sample to adjust focus and stigmatism. In order to obtain an optimal image the grain boundaries of gold were observed while adjusting the SEM knobs for the focus and the stigmatism correction. This procedure was performed at several magnifications until the grains were clearly resolved. Once the best image was achieved the image was switched to the scan mode for the wobbling correction. In this mode a smaller separate square showing a real-time scan image was provided at the center of a frozen image, so that one could realize the movement of the scanned image by comparing the real-time scan image with

the frozen image. Two knobs were used for wobbling correction and adjusted until the movement of the image was minimized in both horizontal and vertical direction. This step was also performed at several magnifications. If the wobbling of the image was too poor to adjust on the gold standard sample, then the adjustment was performed on a grid sample, which provides more clearly angled edges. The optimized image is shown in Fig. III-6.

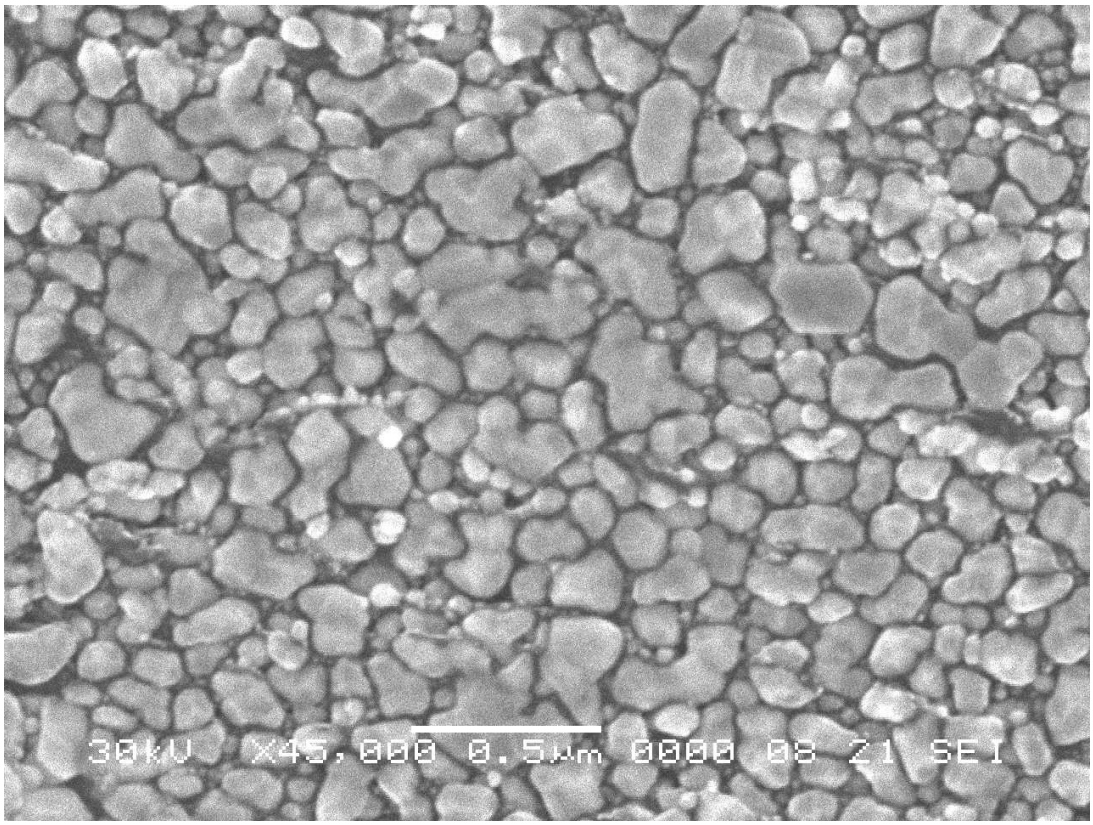

Fig. III-6. SEM image of a gold standard sample scanned at × 45,000.

For the best performance in writing a pattern the function of “lens reset” was applied a couple of times to clean the hysteresis of the lens. After each lens reset, the image was optimized again by following the procedure mentioned above. Next, the beam was moved to the Faraday cup to confirm the beam current. Then, the fully adjusted e-beam was moved to search for the scratch that was created on one of the edges of the substrate [Fig. III-5]. The edge with the scratch was scanned carefully at a suitable magnification in order to allow the area where the pattern would be written on the PMMA surface to be safe from exposure by the scanning beam. Usually a tiny broken section denoting the end of the scratch was found on the edge as shown in Fig. III-7 (a). A starting point of the scratch was readily traced from the broken section. An example for the starting point is shown in Fig. III-7 (b).

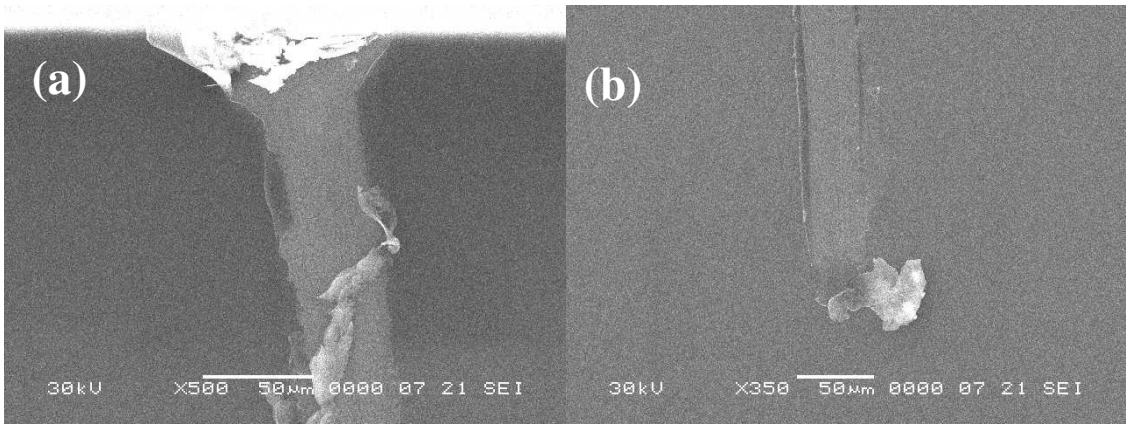

Fig. III-7. (a) The end of the scratched mark on a side of the Si/SiO_2 substrate. (b) The tip of the scratch from which the scratch is drawn.

A section of the particle on the tip of the scratch was chosen as an object for an additional focus adjustment. This step was required because there had been a wide movement of the stage. Once the sharpest boundary of the object at the maximum magnification of the SEM (× 330,000) was achieved (this was done by adjusting the fine-focus), the beam was turned off. The beam was then moved to an intended area that should be close to the object used for the fine-focusing within no overlapping of the scratch with a pattern designed to be written. For the final check of the beam status the e-beam of -10 pA measured in the Faraday cup was injected in to the sample at the maximum magnification, × 330,000, on the e-beam writing mode (NPGS). When the beam was ideally optimized, the pico-ammeter was reading the absolute value of the beam current, dropping as the increase of the back scattered electrons reduced the total current of electrons. With a poorly adjusted beam one could not expect any significant drop of the beam current. That happened often especially when the exposed area was too far from the tip of the scratch due to the size of the designed pattern. In this case the focus was slowly re-adjusted while watching the pico-ammeter carefully. Once the beam was in focus, a significant drop of the beam current was observed. The system was then switched to SEM mode after about 10% of the current drop. Usually it was switched when the beam current dropped down to -7.5 pA from the initial value, which was normally about -8.3 pA due to the back scattered electrons. If a decrease in beam current was successfully achieved, a spot contaminated by the e-beam would be observed in the SEM mode. Once the spot was obtained the SEM knob for the fine-focus was adjusted until the spot image became closer to a circle. After the readjustment the process to

"burn a contamination spot" was repeated at a new surface area ~2 ㎛ apart from the previous spot. The final result for the spot obtained from repeating the step a few times is shown in Fig. III-8. As a final step to write the pattern the beam was turned off and then moved to a desired area. The beam status was changed to Blank mode so that the focused e-beam was controlled by the beam blanker in order for the pattern to be written as intended with NPGS. Required parameters for the e-beam patterning, such as magnification, beam current, center to center distance, and electron dose were entered properly. When the run file was called by the NPGS program the writing procedure was completed. 10 minutes after the filament was turned off, the sample was extracted from the SEM chamber.

Development of the sample revealed a PMMA surface, which had a selectively engraved pattern. To examine the resulting pattern through the SEM, a thin metal layer was deposited onto the patterned PMMA surface. The metal coated surface could be observed either directly or after a lift-off process. For the latter case, a 20~30 nm thick metal film was deposited by thermal evaporation before the lift-off process. Figure III-9 shows an SEM image for a dot-array pattern using the procedure described above. A 30nm thick silver film was deposited onto the PMMA surface of the sample after development, and the sample was dipped in acetone for a lift-off of the resist material.

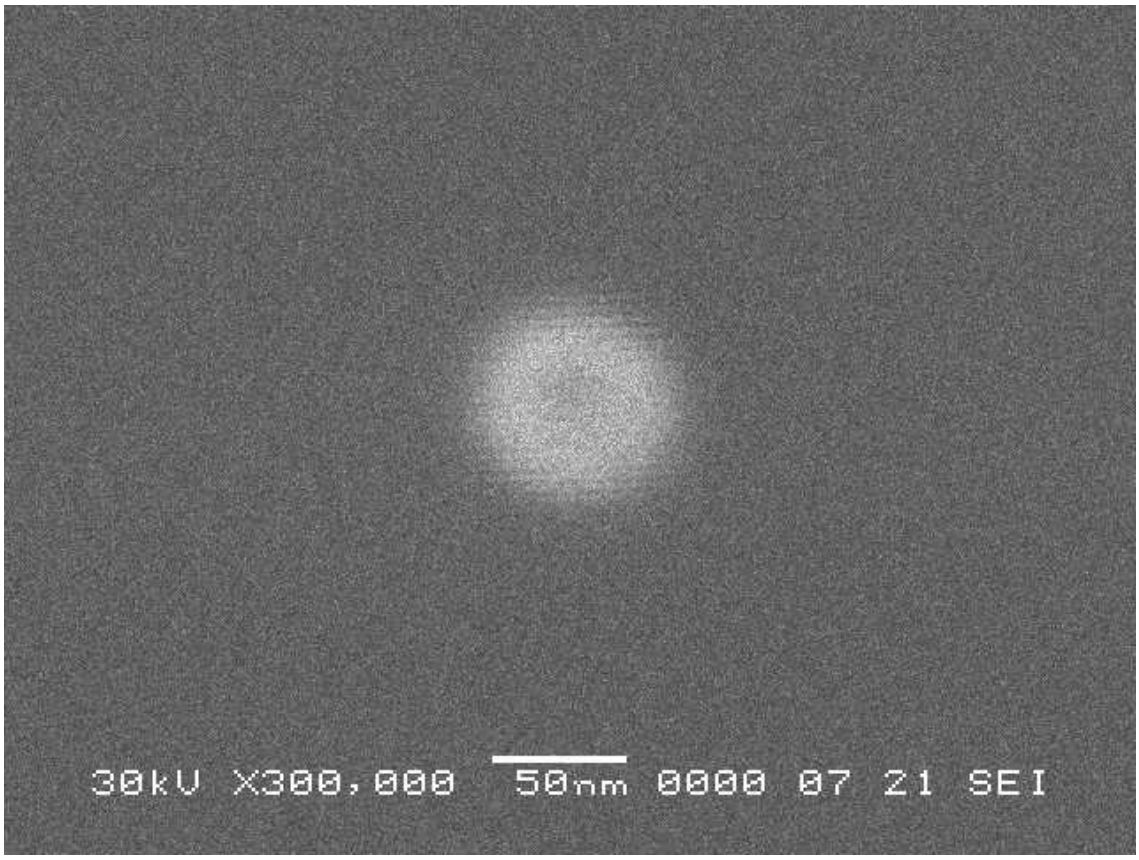

Fig. III-8. SEM image of a contamination spot on the PMMA surface exposed to an optimized e-beam.

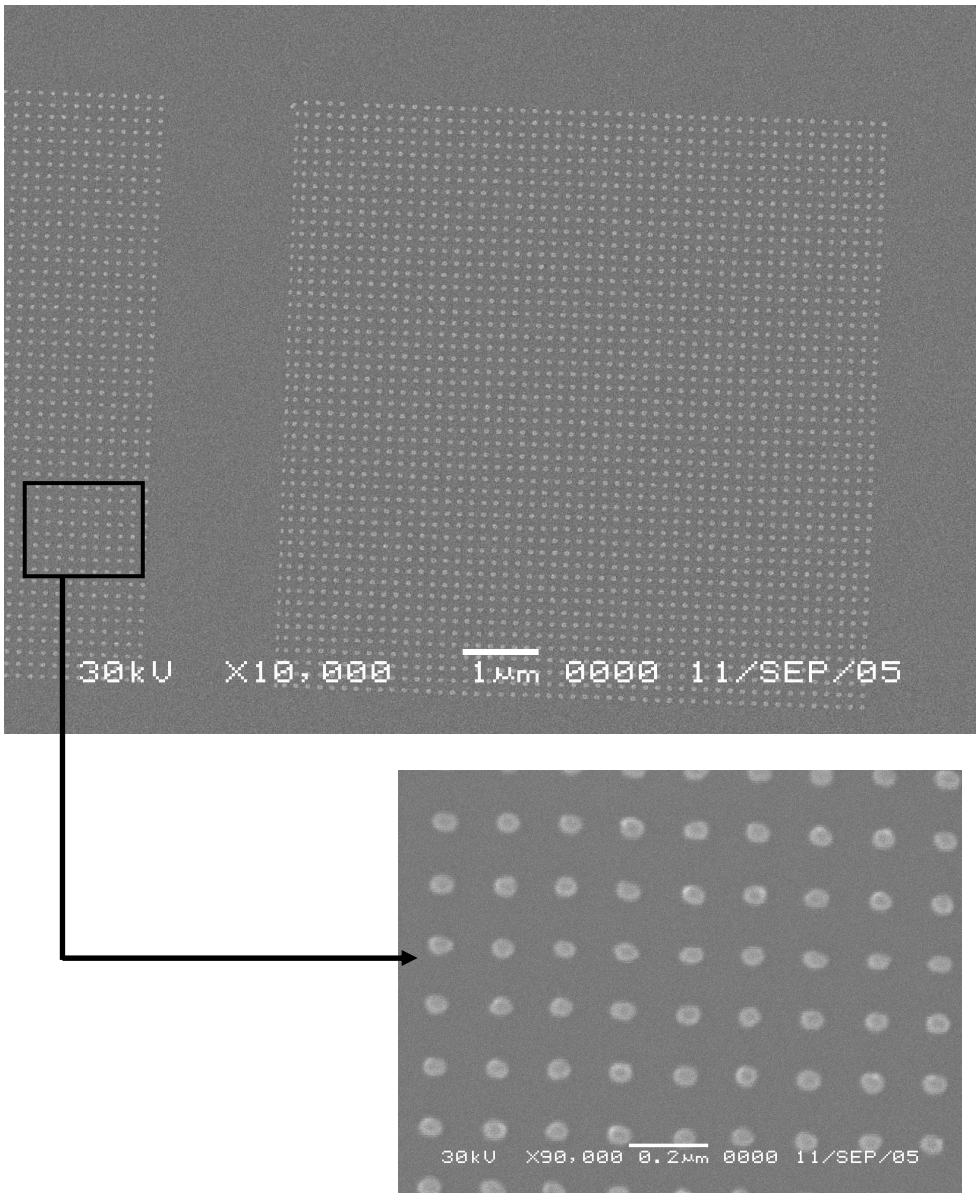

Fig. III-9. SEM image of a dot-array and an enlarged section (bottom) from the box in the top image.

Analysis

The created micro/nano-patterns of the Mn_{12}-acetate film were examined by a series of facilities designed for materials characterization and surface analysis, such as atomic force microscopy (AFM), X-ray photoelectron spectroscopy (XPS), and superconducting quantum interference magnetometry, to investigate the surface characteristics of the resulting patterns which were shown in an earlier section [Fig. III-2 and Fig. III-3 (b)]. A section of the patterned structures was scanned with an AFM (Digital Instruments Nanoscope IIIa) in each case. The scanned data was obtained in the

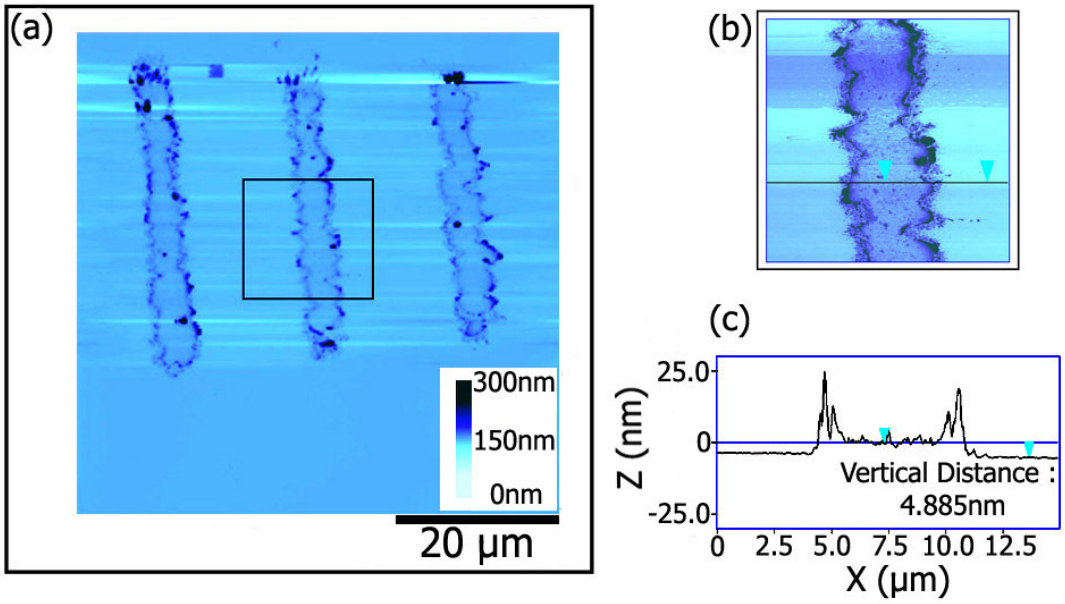

Fig. III-10. (a) AFM line scan image of three bars. (b) Enlarged image from the box in image (a). (c) Height profile of the image (b) to allow for measurement of Mn_{12}-acetate film thickness.

tapping mode using a silicon tip (Nano Devices TAP300) in ambient conditions. The AFM image and the height profile of the optical image [Fig. III-2] with nominal width of 5 μm each is shown in Fig. III-10. The Mn_{12}-acetate samples were deposited within the three bars of the image [Fig. III-10 (a)]. The roughness of the surface within the bars is clearly enhanced, compared to the outside regions, where the resist prevented Mn_{12}-acetate adsorption. The outside regions show the same surface roughness as pure Si/SiO_2 substrates, as seen in the height profile [Fig. III-10 (c)]. For the height profile, the region inside the square of the image was rescanned at a larger scan size [Fig. III-10 (b)]. The height difference between the middle of each bar and the Si surface was measured to be about 5 nm with the AFM. This indicates that the film patterns are composed of approximately two to three Mn_{12}-acetate molecular layers. The AFM image of the line pattern in the SEM image [Fig. III-4] is shown in Fig. III-11 (a). Unlike the SEM image [Fig. III-3 (b)], a greater width is observed for the brighter line sections in Fig. III-11 (a) which points to a rounding effect from the AFM tip. Sections of line height on the molecular level as well as sections of the somewhat larger height profile were observed in the 3D image [Fig. III-11 (b)]. To estimate the typical thickness of the patterned Mn_{12} -acetate film, three bars with nominal widths of 500 nm were scanned. The AFM image and the height profile of the bars are shown in Fig. III-11 (c) and (d), indicating a film thickness of ~7 nm. Fig. III-12 shows AFM line scan images of a sample that contains a square array pattern of a Mn_{12}-acetate film. The height difference between the inner regions of each square surrounded by a higher boundary and the outside wall is estimated from the height profile in Fig. III-12 (b). It indicated that, beside the walls,

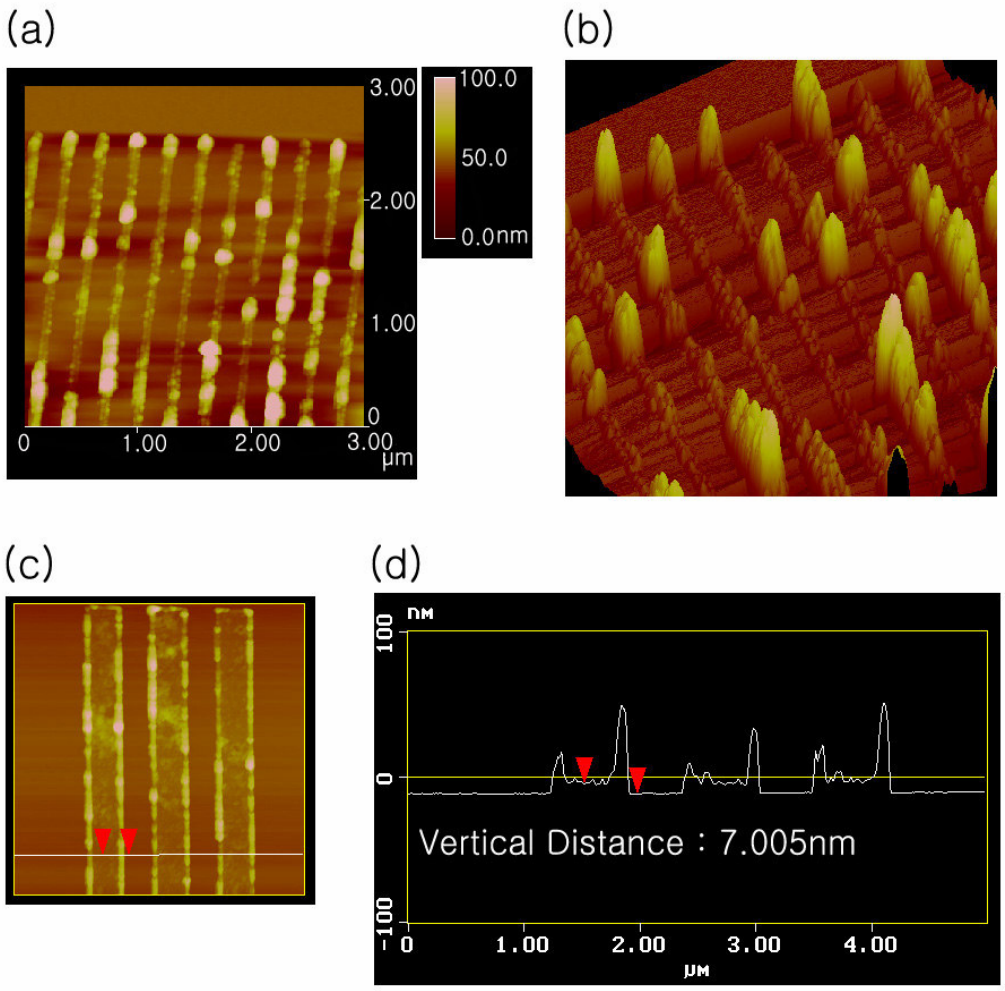

Fig. III-11 (a) AFM line scan image of the line pattern in Fig.III-4. (b) 3D AFM image converted from the image (a). (c) AFM line scan image of three bars in Fig.III-3 (b). (d) Height profile along the white line in the image (c).

the film thickness is about 7 nm, which corresponds to a few molecular layers. From the AFM analysis, it can be concluded that the evaporation method combined with conventional lithography techniques does not result in any significant reduction in Mn_{12}-acetate film thickness.

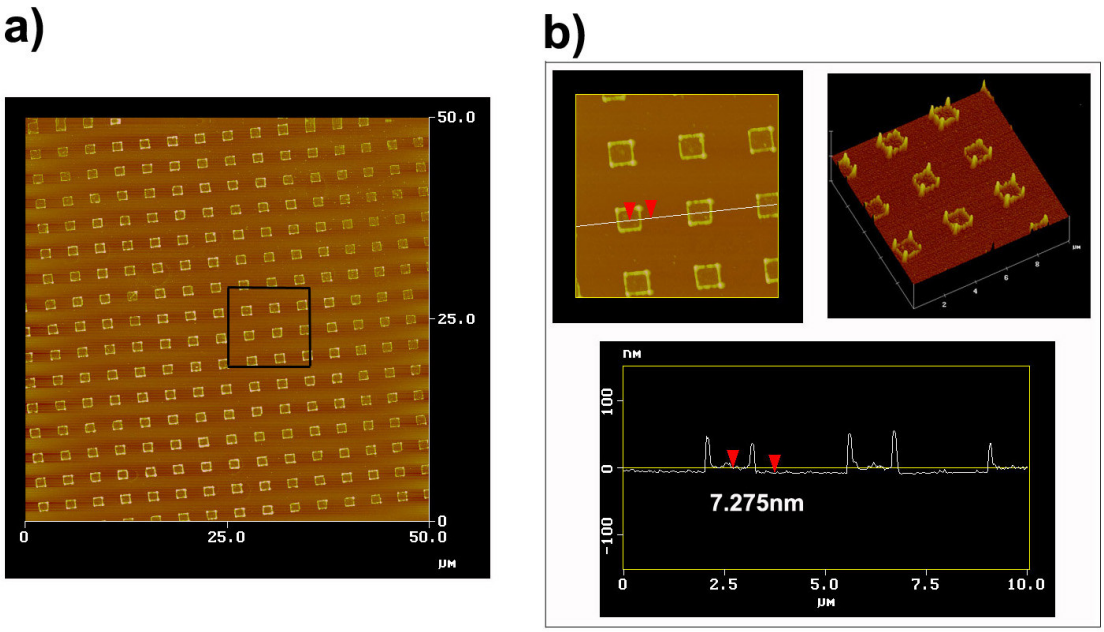

Fig. III-12. (a)AFM line scan image of Mn_{12}-acetate film in square array pattern. (b) Enlarged image from the black box in the image (a) with its 3D image and a height profile along the white line in the line scan image.

It is of interest to ask at this point why higher walls are formed along the edge of the patterns. One plausible explanation invokes the difference in surface tension between the photoresist and the bare Si substrate. As it dries, the Mn_{12}-acetate solution film forms a curved surface along the boundary between two different surfaces, which leads to an inhomogeneous evaporation rate. Therefore, the liquid flows from regions with low evaporation rates to regions with high evaporation rates, thereby transporting the Mn_{12}-acetate solute to curved regions where it accumulates. This phenomenon is also known as the "coffee stain" effect. [36] An actual example of the effect was demonstrated with the Mn_{12}-acetate solution. A droplet of the Mn_{12}-acetate solution cast on a Si/SiO_2 surface formed a domelike shape of liquid pinning down the rim of the domelike liquid to the surface. After all of the solvent was dried in air the solute remained creating a circular pattern which was surrounded by a thick edge as shown in Fig. III-13. A small section of the boundary was scanned with an AFM. The AFM image and the height profile of the bars are shown in Fig. III-14 (a) and (b) revealing a barrier with a nominal width of ~4μm and a vertical height of ~300nm. A small area (5×5 μm^2) outside the stain was scanned with an AFM [Fig. III-14 (c)]. The line scan image for the section shows a smooth surface morphology. That is reasonable because the pinned rim prevented the solution from spreading out past the boundary while the solution evaporated. Therefore there should be a clean Si/SiO_2 surface remaining outside the rim. The line scan image for the section inside the stain [Fig. III-14 (d)] clearly differs from the other. The rough surface image is the reflection of the residual solute which settled down to the substrate during the drying process.

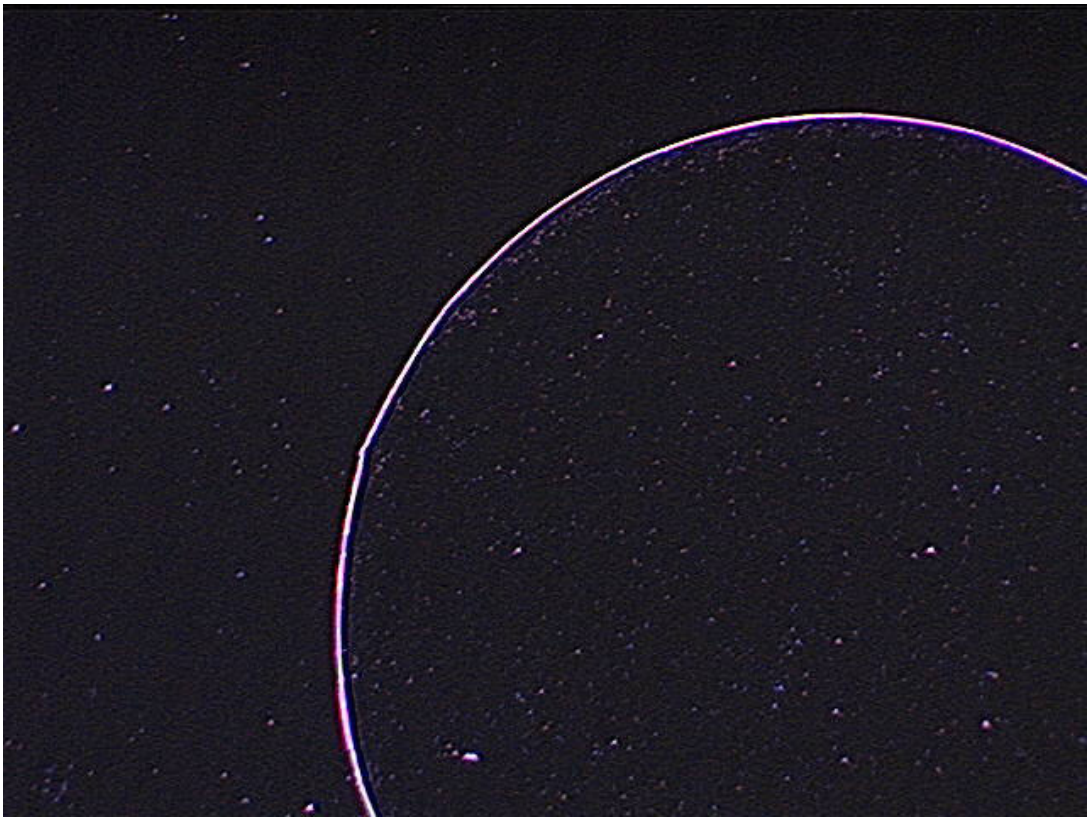

Fig. III-13. Optical micrograph of a Mn12-acetate solution stain on the Si/SiO_2 surface.

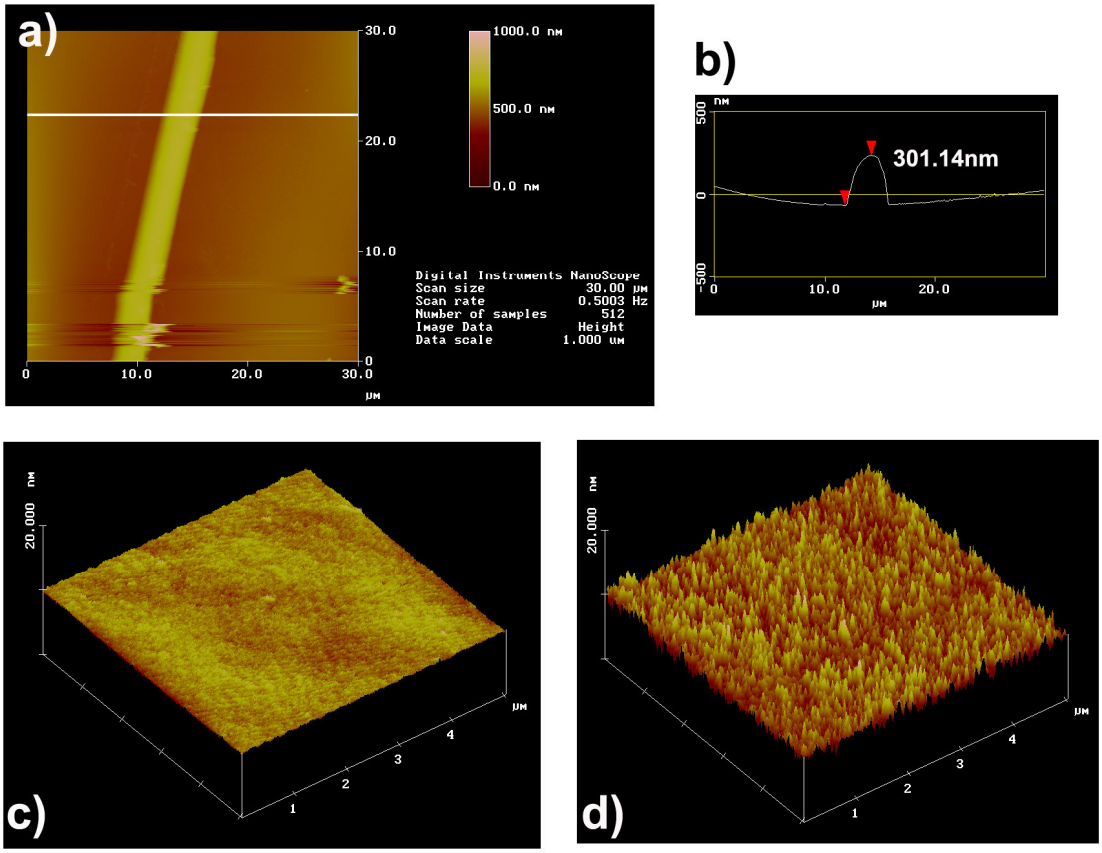

Fig. III-14 (a) AFM line scan image of a small section of the boundary in Fig.III-13. (b) Height profile along the white line in the image (a). (c) 3D AFM image of a small area (5×5 μm^2) outside the stain (left to the barrier). (d) 3D AFM image of a small area (5×5 μm^2) inside the stain (right to the barrier).

Another plausible explanation for the edge effect arises from a meniscus of the solution forming along the step-like boundary of the photoresist. As the solvent evaporates in the dip-and-dry process, the larger abundance of solute per area in the meniscus region leads to a thicker Mn_{12}-acetate film. Although we cannot distinguish which of the effects dominates, both possible reasons emphasize that it is possible to observe a non-uniform surface structure from a resulting pattern created using the solution evaporation technique depending on the topology of the liquid surface.

In order to verify the chemical stability of Mn_{12}-acetate during the patterning process, the lithographically formed Mn_{12}-acetate pattern was investigated by XPS (Kratos Axis System) in the image mode as well as in the spectrum mode. XPS measurements were carried out in vacuum (~2×10^{-8} Torr) with an Al X-ray gun (1486.6 eV). Fig. III-15 (a) shows the intensity versus the binding energy, for the Mn_{12}-acetate film pattern shown in Fig. III-2 acquired in the spectrum mode. The electron pass energy in the analyzer was set at 80 eV. The Mn $2p_{3/2}$ and Mn $2p_{1/2}$ peaks were observed at 642.5 eV and 654.5 eV, respectively. The observation of both Mn peaks in the XPS spectrum indicates the presence of intact manganese core of the Mn_{12}-acetate molecules [37] in the film pattern. Fig. III-15 (b) and Fig. III-15 (c) show an XPS image and an intensity profile of a three bar structure. Because of the limited resolution in the XPS image mode (40 μm), larger patterns were selected. The image was captured in the same vacuum environment for 10,000 sec by scanning at the binding energy for the Mn $2p_{3/2}$ peak (due to its higher intensity) and setting the electron pass energy at 160 eV. In order to reduce the background signal, the image data was also acquired at the 630 eV binding

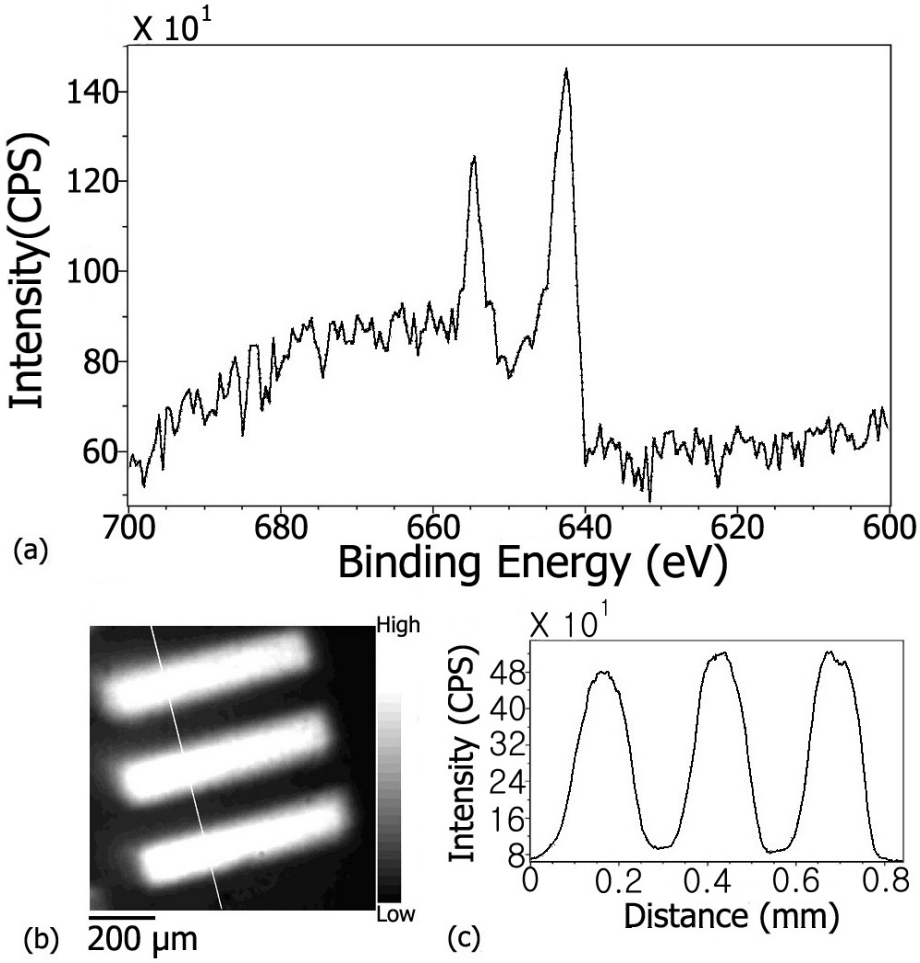

Fig. III-15. (a) XPS spectrum of the Mn_{12}-acetate film pattern. (b) XPS image captured with the binding energy for $Mn2p_{3/2}$ peak. (c) Intensity profile along the white line in the image (b).

energy, and then subtracted from the Mn $2p_{3/2}$ peak image data. The energy 630 eV was chosen roughly based on the background level of the spectrum data [Fig. III-15 (a)]. Because the photoemitted electrons are scattered randomly in space, the pattern boundaries in Fig. III-15 (b) are diffuse and the line profile in Fig. III-15 (c) is rounded. The region including the three bar structure was also scanned at the binding energy for the Si2p peak (100.8 eV) under identical conditions. The image and the intensity profile from the scan was the inversion of the pattern from Fig. III-15 (b) and (c) [Fig. III-16] reflecting a weak signal for the Si buried under the in Mn_{12}-acetate film. The XPS data indicate that the Mn_{12}-acetate film pattern was including manganese ions, which are the most significant elements of the material, after the photolithographic patterning procedure and that Mn_{12}-acetate was defined in the observed pattern.

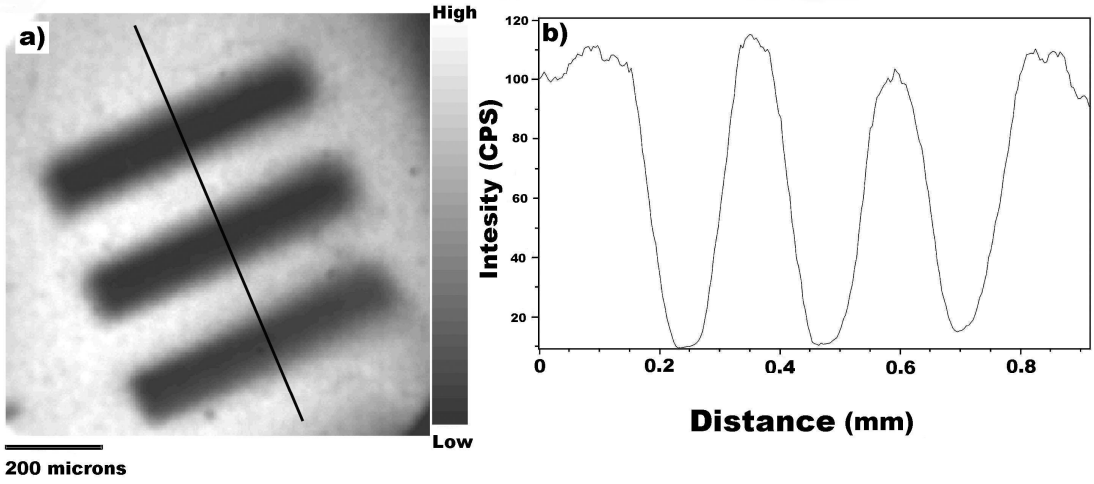

Fig. III-16. (a) XPS image captured with the binding energy for Si2p peak.
(b) Intensity profile along the black line in the image (a).

In order to verify the chemical composition of the thin film patterns generated by the e-beam lithography and the solution evaporation technique using X-ray photoelectron spectroscopy (XPS), a larger bar pattern (width > the minimal resolution in the XPS image mode: ~40 μm) was produced with the procedure which was introduced in the previous section [Fig. III-3 (a)] with a Mn_{12}-acetate solution (2.5×10^{-4} mol l^{-1} of Mn_{12}-acetate in 2-propanol). Fig. III-17 (a) shows the intensity versus the binding energy for the film pattern and the original material. The data was acquired in the spectrum mode of the XPS (Kratos Axis System) in vacuum (~2×10^{-8} Torr) with an Al source ($h\nu$ =1486.6 eV), at an electron pass energy of 80 eV and normalized at the maximum peak for both of them. The Mn $2p_{3/2}$ and Mn $2p_{1/2}$ peaks were observed at 641.8 and 653.3 eV, in agreement with the values for the original powder within the resolution of the XPS system (0.5 eV).[37] Fig. III-17 (b) and (c) show the XPS image and the intensity profile of a large rectangular Mn_{12}-acetate film structure captured in the same vacuum environment for 1500 sec by scanning at the binding energy for the Mn $2p_{3/2}$ peak and setting the electron pass energy at 160 eV. In order to minimize the background signal, the image data was also acquired at 636 eV binding energy, and then subtracted from the Mn $2p_{3/2}$ peak image data. From the XPS data, Mn_{12}-acetate distributed throughout the film pattern is clearly recognized. The same acquisition was carried out at the binding energy for the Si $2p$ peak (99.9 eV) with the background level at 96 eV under identical conditions and the subtracted image is shown in Fig. III-17 (d) indicating the inversion of the pattern from Fig. III-17 (b), as would be expected.

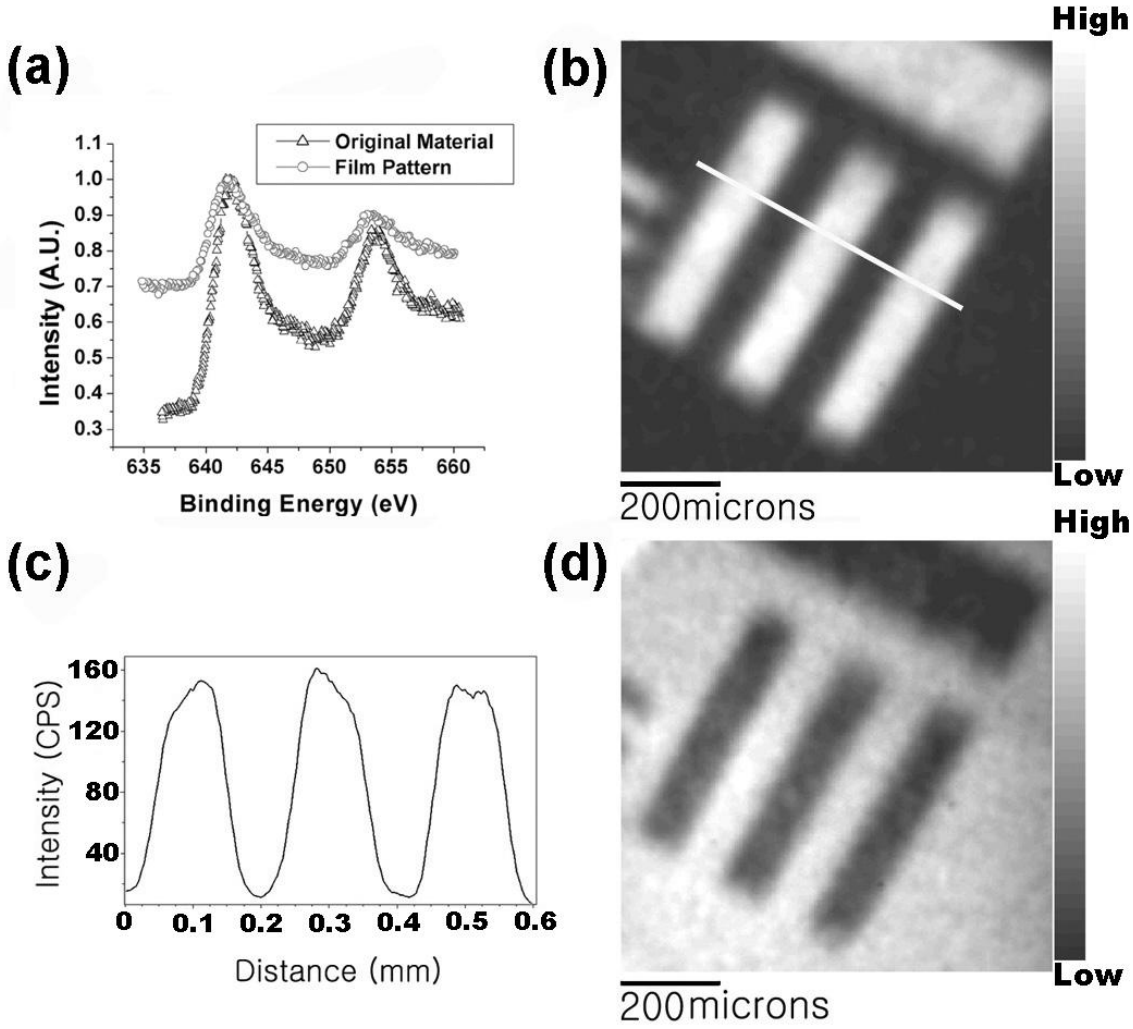

Fig. III-17. (a) XPS spectrum of the Mn_{12}-acetate film pattern and the original material. (b) XPS image of the Mn_{12}-acetate film pattern captured with the binding energy for the Mn $2p_{3/2}$ peak. (c) Intensity profile along the white line in the image (b). (d) XPS image of the Mn_{12}-acetate film pattern captured with the binding energy for the Si $2p$ peak.

In order to extend the success of the Mn_{12}-acetate film production to the fabrication of patterns by lithography and the solution evaporation technique, it was necessary to establish that the Mn_{12}-acetate films were stable in the presence of the solvent as well as the chemicals used in the lithographic steps. The magnetic measurements of powder samples which were derived from films generated through the solution evaporation technique, which is the critical step in the entire patterning procedure, were performed using a Quantum Design SQUID magnetometer MPMS-XL. For the preparation of the samples, the Mn_{12}-acetate molecules were deposited on a glass substrate via the solution evaporation technique. Solutions prepared at twice the previous concentration (5×10^{-4} mol l^{-1} of Mn_{12}-acetate in 2-propanol) were used and the dropping and drying process was repeated over 100 times to obtain a sufficient amount of the Mn_{12}-acetate material in the film. Next, the Mn_{12}-acetate film on the glass surface was scratched off to obtain the powder. The real (χ') and imaginary (χ'') components of the magnetic susceptibility, plotted as a function of temperature (2-11 K) for two different frequencies (1, 35 Hz) are shown in Fig. III-18. The observed frequency shift of the magnetic susceptibility is similar to the original Mn_{12}-acetate powder samples [14], demonstrating the validity of the use of 2-propanol as a reliable solvent for the patterning. Similar magnetic measurements were carried out for the film structure itself. When the Mn_{12}-acetate patterns (on Si substrates, studied by AFM and XPS) were used for SQUID measurements, the output signal from the thin Mn_{12}-acetate film patterns was indistinguishable from the Si/SiO_2 substrate background signal.

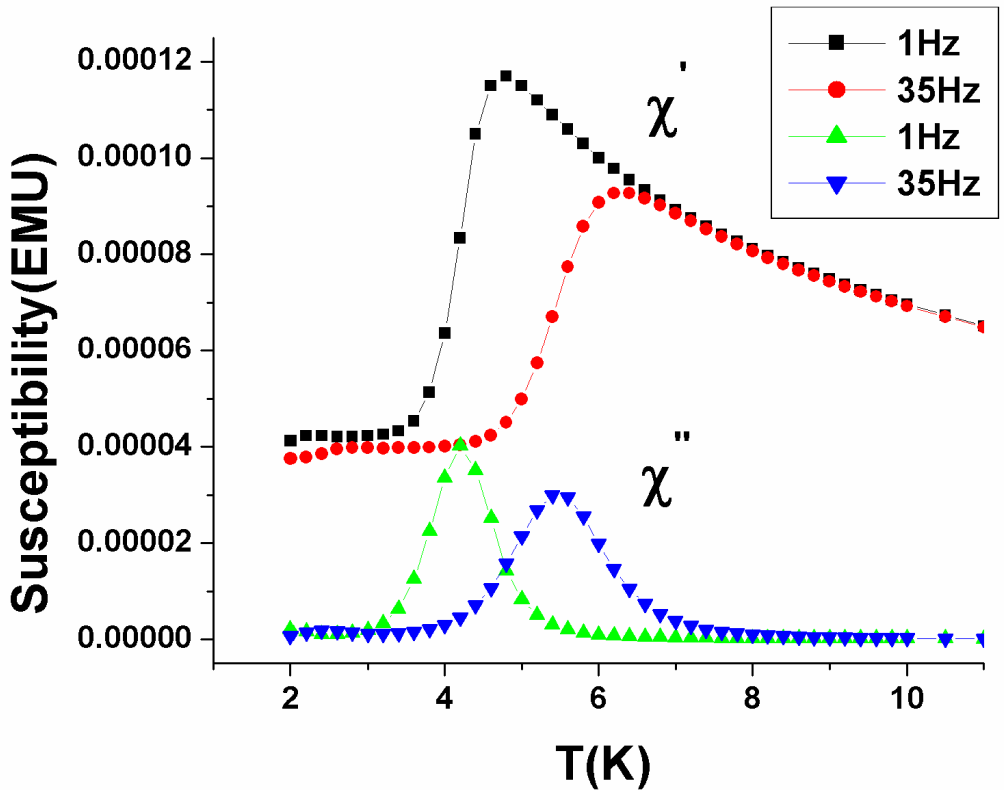

Fig. III-18. Real (χ′) and imaginary (χ″) components of the magnetic ac-susceptibility data for the powder collected from the Mn_{12}-acetate film deposited on a glass surface.

To overcome this problem, small pieces of polyethylene were used as substrates to deposit the films. The output signal from the pure polyethylene piece (without Mn_{12}-acetate films) was negligible as verified by SQUID measurements. The polyethylene pieces were dipped into a Mn_{12}-acetate solution in 2-Propanol and then dried in air. In order to ensure sufficient aggregation of the Mn_{12}-acetate material, a highly concentrated solution (5×10^{-4} mol·L^{-1} of Mn_{12}-acetate in 2-Propanol) was used and the same process of dipping and drying was repeated 50 times. AC-susceptibility data were collected for the Mn_{12}-acetate films on the plastic straw piece. The real (χ') and imaginary (χ'') components of the susceptibility were plotted as functions of temperature (2 K - 11 K) for three selected frequencies (1 Hz, 25 Hz and 50 Hz) as shown in Fig. III-19. The temperatures and shifts for the peak positions were in agreement with the results acquired from the Mn_{12}-acetate powder samples. The noise and scatter in the data are attributed to the nature of the film on a substrate as compared to an oriented powder sample and to the relatively small amount of material of the film sample. The magnetic measurements demonstrated that the films formed by this technique are indeed composed of Mn_{12}-acetate.

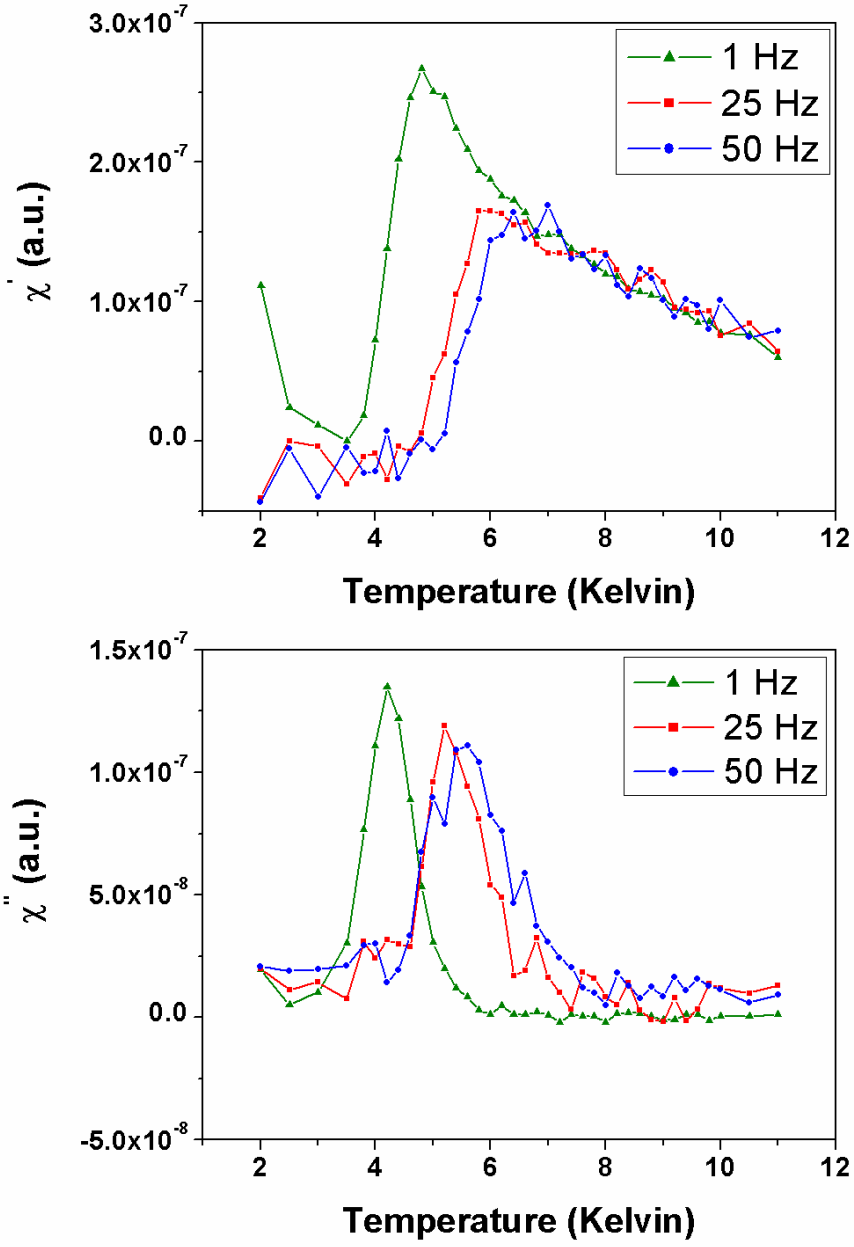

Fig. III-19. Real part (χ') and imaginary part (χ'') of AC-susceptibility data for a Mn_{12}-acetate film deposited on a polyethylene piece as a function of temperature at selected frequencies.

Acetone is the most widely used solvent to remove PMMA resist film. Therefore, it was natural for us to choose acetone as a PMMA remover for the pattering. At the very beginning the Lift-off process [Fig. III-3 (a)] was performed with acetone and the resulting samples revealed inhomogeneous surface morphology when they were observed via an optical microscope, SEM, and AFM, opening the technical prospect for the sub-micro patterning using e-beam lithography. The SEM image of the pattern is shown in Fig. III-20. A result from the AFM analysis of the film pattern shape is shown in Fig. III-21.

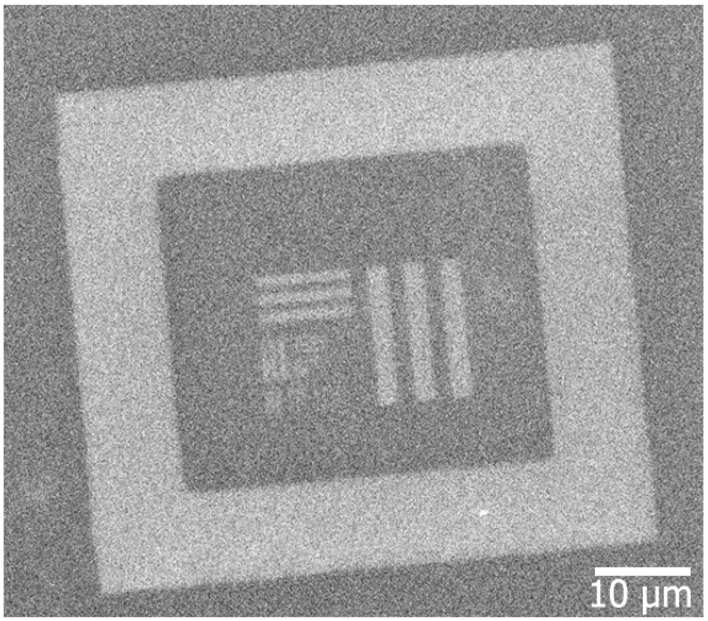

Fig. III-20. SEM image of Mn12-acetate film pattern produced by EBL and a solution evaporation technique using acetone as a PMMA remover.

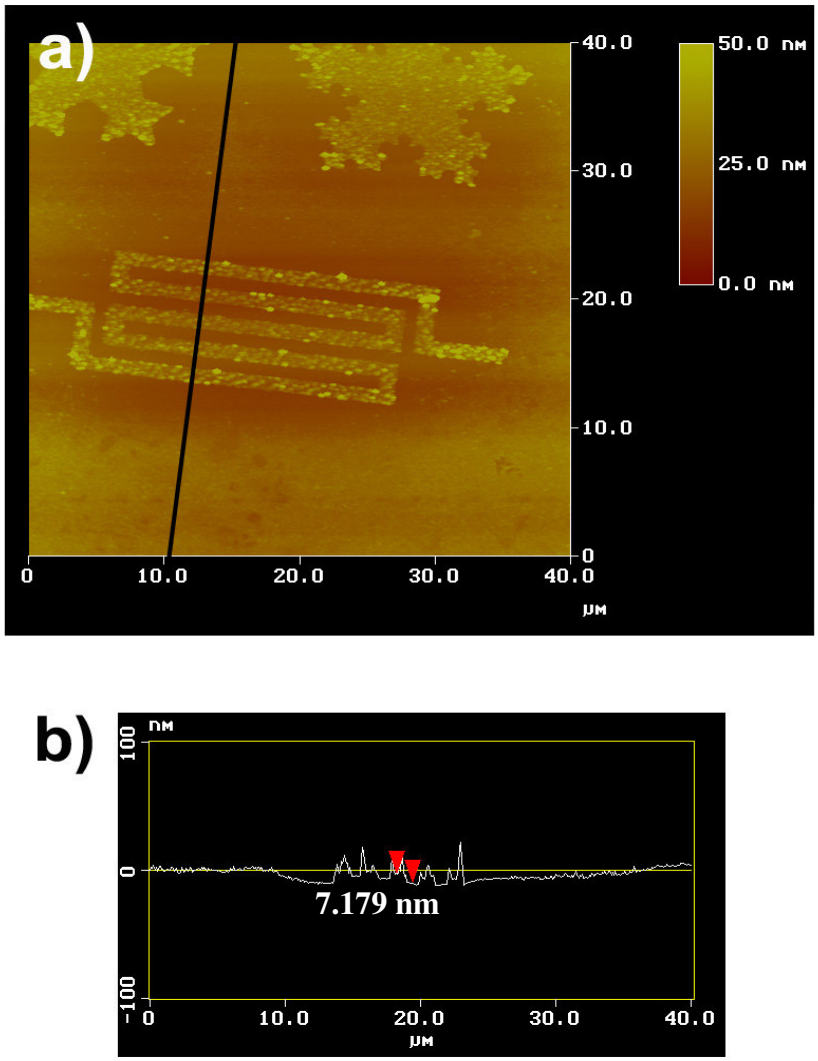

Fig. III-21 (a) AFM line scan image of a Mn12-acetate film pattern. (b) Height profile along the black line in the image (a).

However, the stability of the complexes in the presence of acetone must be confirmed as the patterning procedure includes a lift-off step using acetone. In order to investigate the compatibility of Mn_{12}-acetate and acetone, magnetic ac-susceptibility data of the powder samples were acquired (Quantum Design MPMS-XL SQUID magnetometer). These powder samples were extracted from a Mn_{12}-acetate film dipped in acetone for 1min (the minimal exposure necessary for the patterning). The film used in this experiment was generated by repeating the drop and dry of Mn_{12}-acetate solution in 2-propanol. The magnetic susceptibilities are plotted as a function of temperature (2-7.5 K) for two different frequencies (1, 35 Hz) [Fig. III-22]. The paramagnetic behavior dominating the real component of the susceptibility [Fig. III-22 (a)] indicates that a portion of the film material may be decomposed by the acetone treatment. The peaks at 4-6K, evidence for the existence of the intact Mn_{12}-acetate powder sample[4], are observed in both components, especially in the out of phase signal [Fig. III-22 (b)] where there is no contribution from the paramagnets. The existence of the peaks may be caused by underlaying layers of the film, which were not in direct contact with the acetone and therefore did not experience its deteriorating effect.

For a successful achievement on the nano-patterning of SMMs with this approach, a choice of a safe chemical used to remove the PMMA film that would be harmless to SMMs is crucial. CH_2Cl_2 is another solvent that is widely used as a PMMA remover and it was employed as a substitute for acetone. Unlike acetone, the magnetic susceptibility of the CH_2Cl_2 treated powder supports the conclusion that the integrity of the Mn_{12}-acetate cluster is preserved after the CH_2Cl_2 treatment as shown in Fig. III-23.

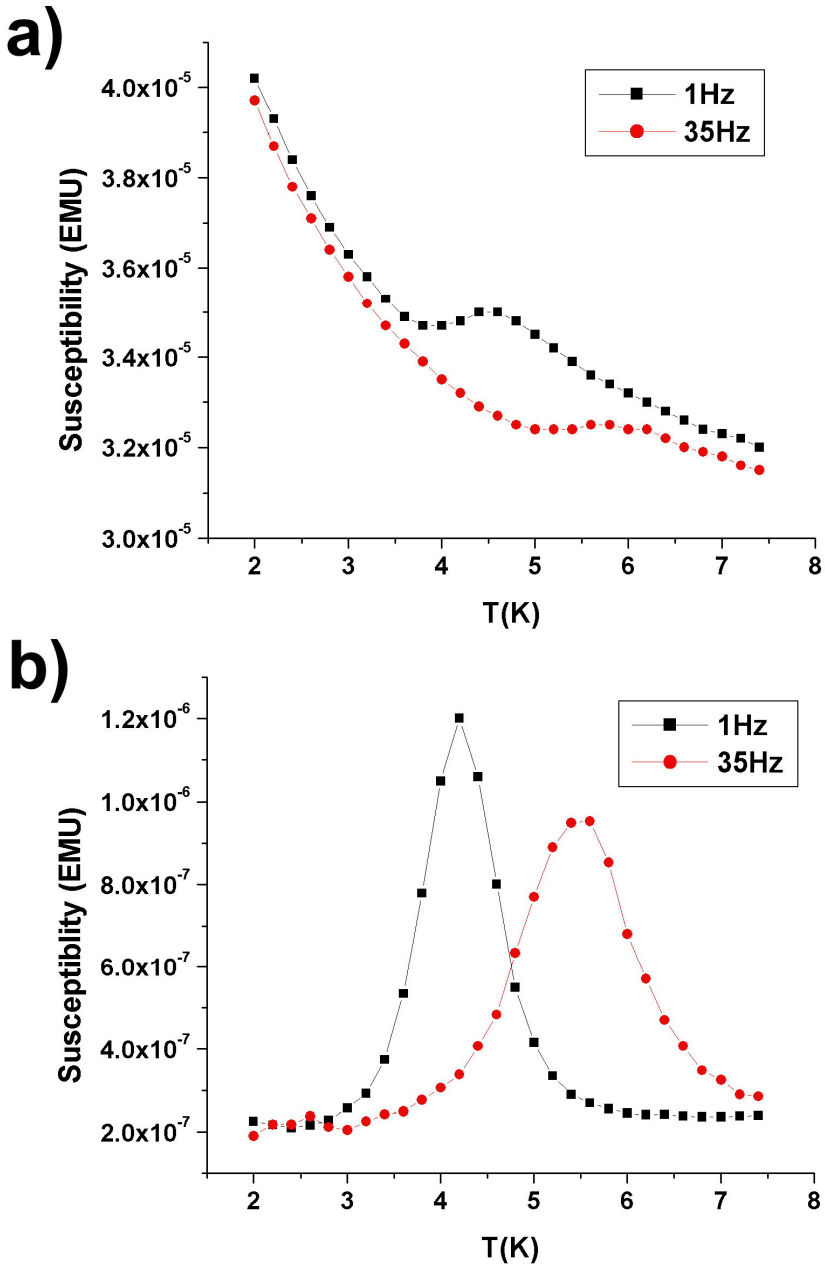

Fig. III-22. Real (a) and imaginary (b) components of the magnetic ac-susceptibility data for powder collected from the Mn_{12}-acetate film after acetone treatment.

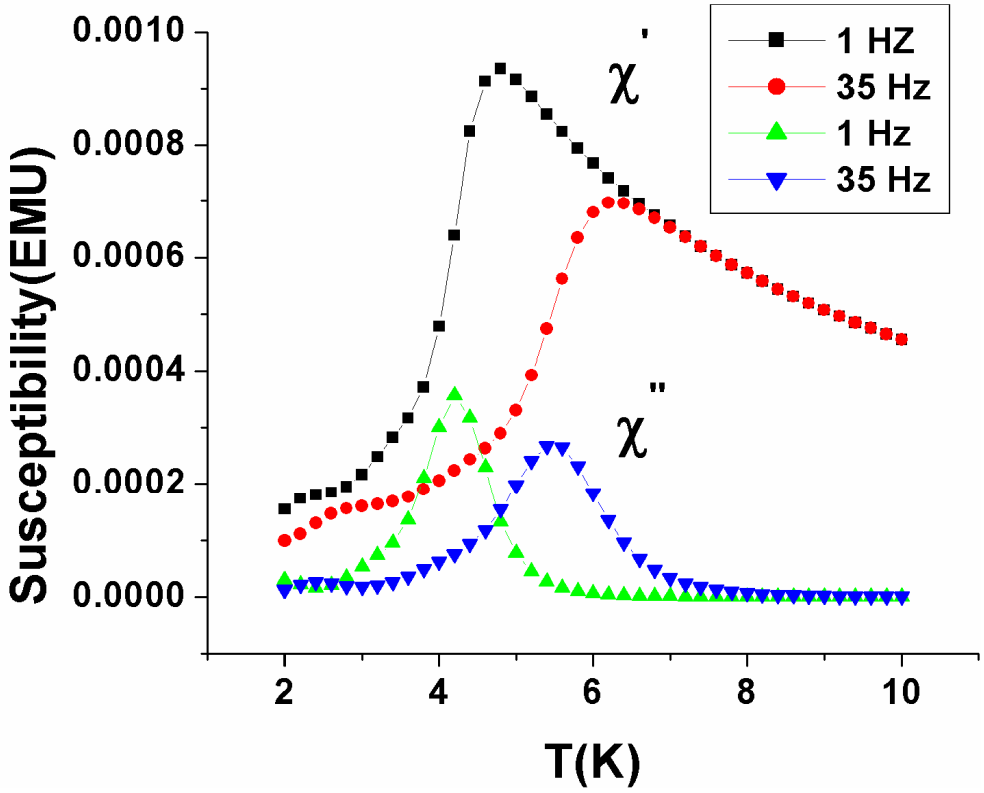

Fig. III-23. Real (χ′) and imaginary (χ″) components of the magnetic ac-susceptibility data for the original Mn_{12}-acetate powder after CH_2Cl_2 treatment.

Throughout this whole chapter the motivation and the entire procedure to create a film pattern of Mn_{12}-acetate in micro/nano-scale were described. From various experiments including SEM and AFM scanning, XPS analysis, and magnetic measurements using a SQUID magnetometer, it has been concluded that the solution evaporation methods to deposit the Mn_{12}-acetate SMMs on a substrate could be combined with a regular lithography technique, such as photolithography and EBL to achieve the goal, as long as suitable chemicals which are not affecting the property of molecules are used for the process. Reversely, this approach can be generally applied to the other species of SMMs if proper chemicals could be found for their treatment. Despite the series of experiments that has been performed, a direct observation of the novel magnetic properties of the SMMs from the created film pattern still remains to be investigated. Several instruments, such as magnetic force microscope, scanning Hall microprobe, spin polarized scanning tunneling microscope, and micro/nano-SQUIDs are being considered for a direct magnetic measurement on such a small magnetic system. The next chapter will treat the development of SQUIDs. A theoretical background will be discussed suggesting a proper design for the device. Experimental results and a technical approach for a direct observation of the magnetic state of a small magnetic system will be addressed.

CHAPTER IV

DEVELOPMENT OF MICRO/NANO SUPERCONDUCTING QUANTUM INTERFERENCE DEVICES (SQUIDs)

Theoretical background

SQUIDs [38-40] are superconducting devices which are composed of a superconducting loop and one or more weak links. These devices show a non-linear I-V (Current vs. Voltage) characteristic that is modulated by a magnetic flux inside the loop, allowing one to sense and analyze an extremely weak magnetic field. A brief theoretical overview of the operational principle of dc SQUIDs will be part of this section.

The basic element of the SQUID considered here includes a loop of superconductor and two weak links, as shown in Fig. IV-1.

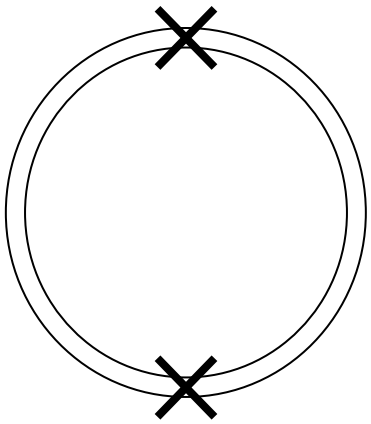

Fig. IV-1. Superconducting loop with two weak links. The cross marks are indicating weak links.

Generally speaking, a weak link means a weak connection between two pieces of superconductor. The specially designed junction has a much lower critical current than the adjacent superconductors, providing a path for a magnetic field to enter into the loop. There are some suitable designs to achieve this purpose, such as the Josephson tunneling junction in which two superconductors are linked via a thin insulating material, a very narrow constriction and a point contact between two superconductors. The supercurrent (resistanceless current), or the current of paired electrons passing through the weak links, increases as the difference of the phase of the electron pair wave across the junction increases, and the supercurrent reaches the critical value when the phase difference is $n\pi/2$, where n is an integer. In other words, the phase difference induced by the tunneling process depends on the supercurrent flowing through the junction. The presence of two weak links in a superconducting loop [Fig. IV-1] takes a significant role in the operation of SQUIDs as will be discussed soon. An applied magnetic field is another strong factor that manipulates the phase of the electron pair wave. In a superconductor all the electron pairs have the same momentum ($\vec{p}$) making the current density uniform. Hence, the paired electrons can be described by a single wave given by

$$\Psi = \sqrt{n} e^{i\frac{\vec{p}}{\hbar}\cdot\vec{r}} \qquad \text{(IV-1)}$$

where n is the density of the electron pairs. The phase difference between two points, 1 and 2, within a path l is

$$(\Delta\phi)_{12} = \frac{1}{\hbar}\int_1^2 \vec{p}\cdot d\vec{l} \qquad \text{(IV-2)}$$

where $d\vec{l}$ is an infinitesimal displacement vector along the path l. The relation of a momentum $\vec{p}$ to electron pair current density $\vec{J}$ is $\vec{J} = \frac{ne}{m}\vec{p}$, where e is the charge of single electron and m is the mass of a single electron, and therefore the phase difference $\Delta\phi$ is rewritten with the current density as

$$(\Delta\phi)_{12} = \frac{m}{\hbar ne}\int_1^2 \vec{J}\cdot d\vec{l}\,. \qquad \text{(IV-3)}$$

In the presence of a magnetic field the momentum for the paired electrons takes the form, $\vec{p} = \vec{p} + \frac{2e}{c}\vec{A}$, where c is the velocity of light and $\vec{A}$ is the vector potential defining the magnetic flux density $\vec{B}$ by $\vec{B} = \vec{\nabla}\times\vec{A}$. Thus, in this case, the phase difference between two points, 1 and 2, is

$$(\Delta\phi)_{12} = \frac{m}{\hbar ne}\int_1^2 \vec{J}\cdot d\vec{l} + \frac{2e}{\hbar c}\int_1^2 \vec{A}\cdot d\vec{l}\,. \qquad \text{(IV-4)}$$

In the equation above, the first and second terms are the phase difference attributed to the supercurrent and the magnetic field, respectively. Actually, in SQUIDs the overall supercurrent is limited by weak links and therefore a very small derivation from the first

term to the phase difference is expected through the piece of superconductor which does not include the weak junctions. So far the two significant factors, the tunneling through a weak link and the magnetic field, that affect the phase shift of the electron pair wave have been considered. Before we see how these factors interfere with each other to create the non-linear I-V curve that is modulated by a magnetic flux, an examination of Josephson tunnel junctions is at hand because all other forms of weak links have similar properties to these junction and the sinusoidal modulation of the tunneling current which is from the Josephson junction will be used for the following explanation for the SQUIDs.

Ψ_1 and Ψ_2 are defined as the wave function of electron pairs on the side 1 and the side 2 , respectively, in the Josephson junction as shown in Fig. IV-2.

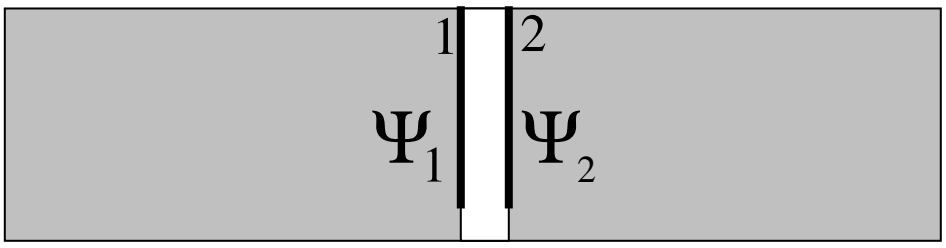

Fig. IV-2. A description of the Josephson junction. Two superconductors (gray) are separated by a thin layer of an insulator (white).

If both of the superconductors are identical and they are at zero potential, then the time-dependent Schrödinger equation for the two amplitudes gives equation (IV-5) [41].

$$i\hbar\frac{\partial\Psi_1}{\partial t} = U_1\Psi_1 + T\Psi_2\,; \qquad i\hbar\frac{\partial\Psi_2}{\partial t} = T\Psi_1 + U_2\Psi_2\,. \tag{IV-5}$$

T is a coupling constant that is a measure of the leakage of Ψ_1 into region 2, and of Ψ_2 into region 1. U_1 and U_2 are the lowest energy values of each superconductor in the absence of T. If a voltage V is applied across the junction, then one can define that $U_1=eV$ *and* $U_2=-e$V where e is the charge of a single electron. Putting $\Psi_1 = \sqrt{n_1(t)}e^{i\phi_1(t)}$ and $\Psi_2 = \sqrt{n_2(t)}e^{i\phi_2(t)}$, where n_1 and n_2 correspond to the density of electron pairs in side 1 and side 2, into the equations (IV-5), we find two relations given by

$$\frac{1}{2\sqrt{n_1}}e^{i\phi_1}\frac{\partial n_1}{\partial t} + i\Psi_1\frac{\partial\phi_1}{\partial t} = -\frac{i}{\hbar}eV\Psi_1 - \frac{i}{\hbar}T\Psi_2\,; \tag{IV-6}$$

$$\frac{1}{2\sqrt{n_2}}e^{i\phi_2}\frac{\partial n_2}{\partial t} + i\Psi_2\frac{\partial\phi_2}{\partial t} = -\frac{i}{\hbar}T\Psi_1 + \frac{i}{\hbar}eV\Psi_2\,. \tag{IV-7}$$

By multiplying (IV-6) and (IV-7) by $\sqrt{n_1}\,e^{-i\phi_1}$ and $\sqrt{n_2}\,e^{-i\phi_2}$, respectively, and equating the real part and imaginary part from the results, we obtain the following equations, with $\Delta\phi = (\phi_2 - \phi_1)$.

$$\frac{\partial n_1}{\partial t} = \frac{2T}{\hbar}\sqrt{n_1 n_2}\sin\Delta\phi\;; \qquad \frac{\partial n_2}{\partial t} = \frac{-2T}{\hbar}\sqrt{n_1 n_2}\sin\Delta\phi\,; \tag{IV-8}$$

$$\frac{\partial \phi_1}{\partial t} = -\frac{eV}{\hbar} - \frac{T}{\hbar}\sqrt{\frac{n_2}{n_1}}\cos\Delta\phi\,; \quad \frac{\partial \phi_2}{\partial t} = \frac{eV}{\hbar} - \frac{T}{\hbar}\sqrt{\frac{n_1}{n_2}}\cos\Delta\phi\,. \tag{IV-9}$$

From (IV-8) we can see that the density of electron pairs in side 1 changes in time depending on the phase difference $\Delta\phi$ and the density of electron pairs in side 2 changes in time with the exactly same rate (with a negative sign) as the other case. The opposite sign emphasizes the conservation of electron pairs in the tunneling process. Because the current flow from side 1 to side 2 is propotional to either $-\frac{\partial n_1}{\partial t}$ or $\frac{\partial n_2}{\partial t}$, we can conclude that the relation of supercurrent (i_s) across the junction to the phase difference is given by

$$i_s = i_c \sin\Delta\phi \tag{IV-10}$$

where i_c is the maximum value of the supercurrent, the so-called critical current, and it is defined through the constant T above. Equation (IV-9) tells us about the relation between the supercurrent and the voltage applying across the junction. By subtracting the left equation in (IV-9) from the right equation in (IV-9), and supposing $n_1 = n_2$ as for identical superconductors 1 and 2, we get

$$\frac{\partial \Delta\phi}{\partial t} = \frac{2eV}{\hbar}. \tag{IV-11}$$

Consequently, the supercurrent is given by (IV-10) and (IV-11) as

$$i_s = i_c \sin\{\Delta\phi(0) + \frac{2eV}{\hbar}t\}. \qquad \text{(IV-12)}$$

A pattern of superconducting film in which two weak links are connected in parallel as in Fig. IV-3 is considered in order to examine how SQUIDs operate.

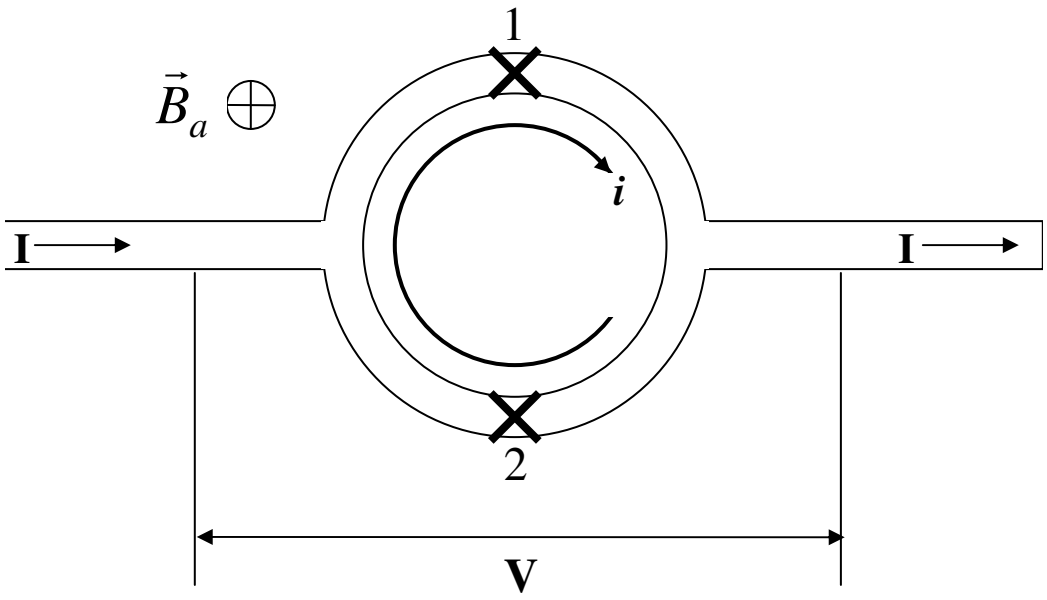

Fig. IV-3. Superconducting quantum interference device (SQUID).

In Fig. IV-3, *i, I,* B_a and *V* are a circulating current, a measuring current, an applied magnetic field, and a voltage across the loop, respectively. As mentioned above there are two significant factors that change the phase of the electron pair wave, namely, an applied magnetic field and the tunneling process. Therefore, it is supposed that the flux generated in the loop by a circulating current is extremely small. Thus the total phase change around the circuit ($\Delta\phi_T$) is written by

$$\Delta\phi_T = \Delta\phi(B) + \Delta\phi_1(i) + \Delta\phi_2(i) \qquad \text{(IV-13)}$$

where $\Delta\phi(B)$ is the phase change produced by the applied field *B,* and the last two terms indicate the phase change caused by the tunneling of the circulating supercurrent *i* through the weak junctions 1 and 2. Due to the weak-links, the circulating current is limited to a maximum value of i_c. Consequently, unless B is very small, not enough current can circulate to cancel the flux in the loop. Although the circulating current is very small, it still can introduce a significant phase change across the junctions as shown in (IV-10). The last term in equation (IV-4) with $\vec{B} = \vec{\nabla} \times \vec{A}$ gives the relation between the phase change around the ring produced by an applied magnetic field and the magnetic flux in the ring

$$\Delta\phi(B) = \frac{2e}{\hbar c}\oint \vec{A} \cdot d\vec{l} = \frac{2e}{\hbar c}\int_s \vec{B} \cdot \hat{n} dS = 2\pi \frac{\Phi}{\Phi_0} \qquad \text{(IV-14)}$$

where $\hat{n}$ is the normal vector of the infinitesimal area dS and Φ_0 is the quantum of magnetic flux

$$\Phi_0 = \frac{hc}{2e} \cong 2.0678\times10^{-7}\, gauss/cm^2 . \qquad \text{(IV-15)}$$

Because of the quantum condition that the total phase difference around a closed route must be 2π multiplied by any integer, the total phase change around the SQUID loop should satisfy

$$\Delta\phi(B) + \Delta\phi_1(i) + \Delta\phi_2(i) = 2n\pi \ ; \ n = \text{integer} \qquad \text{(IV-16)}$$

If, for example, a magnetic field (B_1) is applied to the SQUID loop generating the flux (Φ_1) threading the loop, then the phase change $\Delta\phi(B_1)$ is equal to $2\pi\Phi_1/\Phi_0$ from (IV-14). Because the quantum restriction (IV-16) must be fulfilled, a current i is induced to circulate along the loop yielding the additional phase difference $\Delta\phi_1(i) + \Delta\phi_2(i)$ in order to fill the total phase of 2nπ. If the Φ_1 in between 0 and $\frac{1}{2}\Phi_0$, then the phase change $\Delta\phi(B_1)$ is in between 0 and π as shown in Fig. IV-4 (a). In this situation there are two possible ways for the quantum condition (IV-16) to be fulfilled. In one case a circulating current i could be induced to circulate in the counterclockwise direction, producing a negative phase change at the weak junctions.

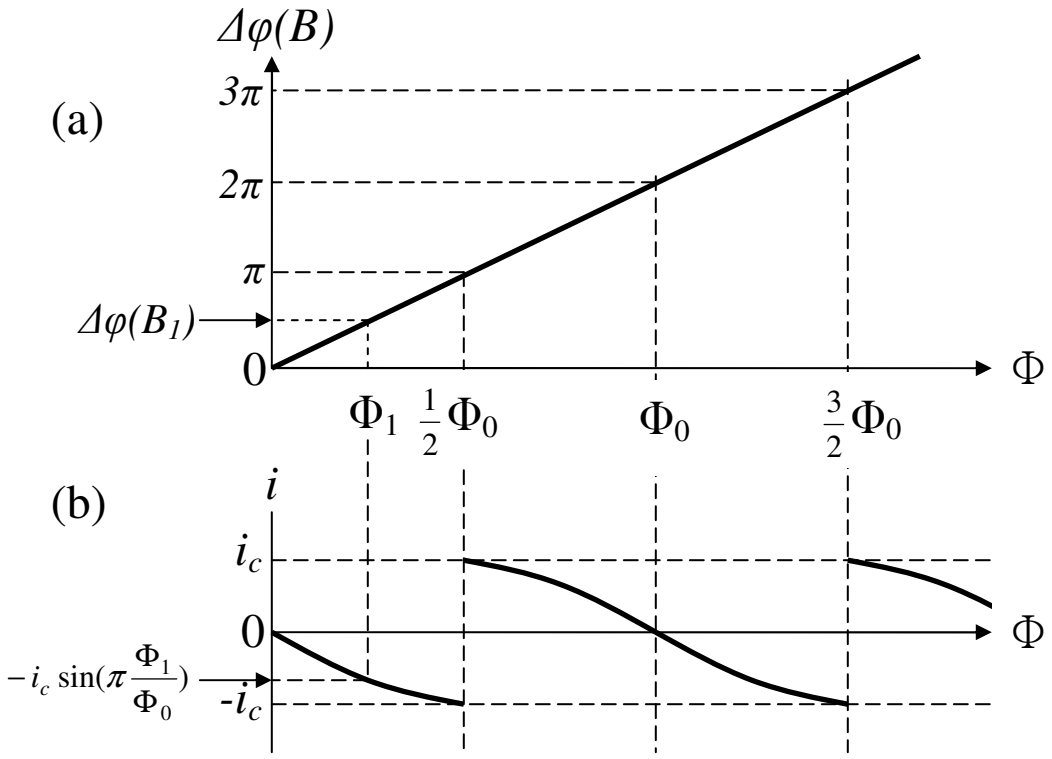

Fig. IV-4.The relation of the magnetic flux enclosed in the SQUID loop to (a) the phase change caused by an applied magnetic field $\Delta\phi(B)$ and to (b) the circulating supercurrent *i* (the negative current *i* circulates in the counterclockwise direction and the positive *i* circulates in the clockwise direction). Modified from ref. [38].

If the junctions are identical, then the total phase change caused by the junctions is $-2\Delta\phi(i)$. Here $\Delta\phi(i) > 0$ and the negative sign means the counterclockwise direction of

the circulating current. This value would exactly cancel the phase change $\Delta\phi(B_1)$ making the total phase change zero. Hence the phase change $\Delta\phi(B_1)$ is equal to $2\Delta\phi(i)$. Therefore, from (IV-10) and (IV-14), the magnitude of the induced circulating current is given by

$$|i| = i_c \sin(\pi \frac{\Phi_1}{\Phi_0}) . \qquad \text{(IV-17)}$$

This value is shown in the negative region for the current in Fig. IV-4 (b).

A circulating current which circulates in the clockwise direction is the other possible source that yields a certain amount of phase change. However, in this case, the phase change from the tunnel junctions is added on $\Delta\phi(B_1)$ to make the total phase difference around the loop to be 2π. Therefore, the phase change $\Delta\phi(i)$ is equal to $\pi(1-\frac{\Phi_1}{\Phi_0})$. In fact the circulating current which is actually induced is the same as previous case because it is clear that $\pi > \pi(1-\frac{\Phi_1}{\Phi_0}) > \pi\frac{\Phi_1}{\Phi_0}$ for the magnetic flux (Φ_1) in between zero and $\frac{1}{2}\Phi_0$.

The phase change is related with the energy of the junction due to the tunneling of electron pairs through it. Using (IV-10), (IV-11), and the electric power of $i \cdot V$, we get the work *W,* which is performed in setting up the current and the consequent phase difference across the junction.

$$W = \int i_c \sin\Delta\phi \cdot \frac{\hbar}{2e}\frac{d\Delta\phi}{dt} \cdot dt = \frac{i_c \hbar}{2e}\left[1 - \cos\Delta\phi\right]. \qquad \text{(IV-18)}$$

It is shown from (IV-18) that, for $0 < \Delta\varphi < \pi$, a smaller phase difference is energetically favorable, therefore in the previous example the current circulating in the counterclockwise direction is naturally induced. In a similar manner, if the magnetic flux (Φ) generated by an applied field is between $\frac{1}{2}\Phi_0$ and Φ_0, then the circulating current will be induced in the clockwise direction making the total flux equal to 2π. Extension of this argument for the induced circulating current to even further phase is shown in Fig. IV-4 (b). The current is changed periodically with the period of a flux quantum (Φ_0).

It is difficult to measure the circulating current directly to learn about the magnetic flux in the loop. One needs to have a better quantity which is easily measured and somehow coupled with either the circulating current or the magnetic flux. One approach is to send a current *I*, the so-called measuring current, through the device as shown in IV-3. One can find how the measuring current depends on the magnetic flux Φ_a generated by an applied magnetic flux density B_a. In the presence of the measuring current $\Delta\phi_1(i)$ and $\Delta\phi_2(i)$ are not equal anymore even if the two junctions are identical because the current passing through the junction 1 is $i + \frac{1}{2}I$ and that through the

junction 2 is $i-\frac{1}{2}I$. From (IV-16) $\Delta\phi_1(i+\frac{1}{2}I)+\Delta\phi_2(i-\frac{1}{2}I)=2\pi(n-\frac{\Phi_a}{\Phi_0})$, and therefore one can suppose that

$$\Delta\phi_1=\pi(n-\frac{\Phi_a}{\Phi_0})+\alpha,\ \ \Delta\phi_2=\pi(n-\frac{\Phi_a}{\Phi_0})+\beta \tag{IV-19}$$

where α and β depend on the current I and $\alpha+\beta=0$. From equation (IV-10) the phase difference across the junction due to the current through them is given by

$$i+\frac{1}{2}I=i_c\sin\left\{\pi(n-\frac{\Phi_a}{\Phi_0})+\alpha\right\},\ i-\frac{1}{2}I=i_c\sin\left\{\pi(n-\frac{\Phi_a}{\Phi_0})+\beta\right\}. \tag{IV-20}$$

Eliminating i by subtracting the right equation from the left equation in (IV-20),

$$I=i_c\left[\sin\left\{\pi(n-\frac{\Phi_a}{\Phi_0})\right\}(\cos\alpha-\cos\beta)+\cos\left\{\pi(n-\frac{\Phi_a}{\Phi_0})\right\}(\sin\alpha-\sin\beta)\right]. \tag{IV-21}$$

Since $\alpha=-\beta$, the final result is

$$I=2i_c\cos\left\{\pi(n-\frac{\Phi_a}{\Phi_0})\right\}\sin\alpha\,. \tag{IV-22}$$

However, the maximum absolute value of $\sin\alpha$ is unity, therefore the maximum amplitude of the measuring current is

$$I_{\max} = 2i_c \left| \cos \pi \frac{\Phi_a}{\Phi_0} \right| . \qquad \text{(IV-23)}$$

It is concluded that the critical measuring current I_c (=$I_{\max}$) depends on an applied magnetic field in a periodic function, as shown in the Fig. (IV-5), allowing one to analyze a magnetic state of a system by analyzing the critical measuring current I. In the following sections a process to create an actual micro/nano SQUID and the result from the device will be presented.

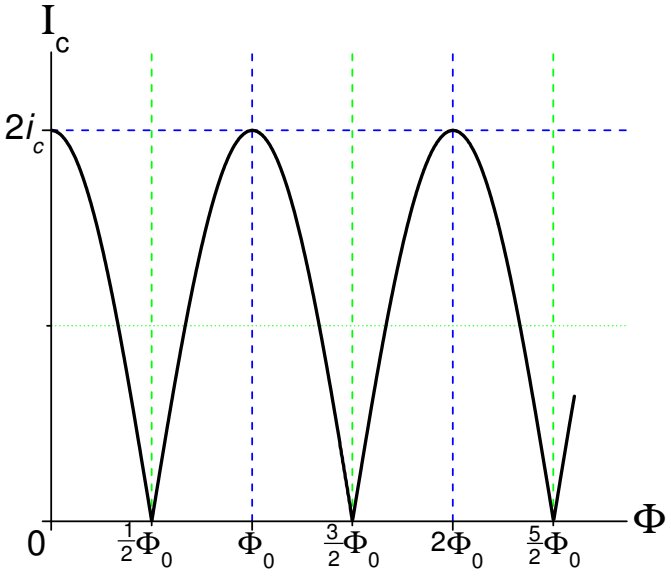

Fig. IV-5. Critical measuring current I_c as a function of the magnetic flux Φ.

Fabrication

Micro/nano-SQUIDs [42] were fabricated using EBL and thermal evaporation. PMMA film masks defining the SQUID were created on Si/SiO_2 substrates using EBL. This procedure was performed by the method introduced in Chapter III, Electron Beam Lithography. A dummy pattern was engraved right next to the real pattern. This dummy pattern is an identical design to the real pattern except having none of the legs for the contacting pads that are used for making electrical contacts for measurement. The purpose of this dummy pattern is to examine the core structure by SEM: the superconducting loop containing the two weak links. An electron beam degrades the device (especially the narrow junctions). A thin aluminum film of 300~400Å was deposited onto the substrates with a rate of 4~7 Å /sec. A 99.9% pure aluminum pellet was melted for the evaporation in a vacuum of ~ 6×10^{-6} Torr. As a final step, the samples were dipped into acetone for 60 min for the Lift-off process. If there was an uncleared section observed through an optical microscope, then the sample was sonicated in acetone for less than 60 sec to completely remove all the unwanted material. After the lift-off process, the sample was observed through an optical microscope and the real device was compared to the dummy device to confirm that these two devices are identical within the resolution of the optical microscope. The dummy pattern was scanned with a SEM. SEM images for the resulting devices are shown in Fig. IV-6.

Measurement and analysis

Au wires were attached to pads which were in turn attached to the core structure of the device. An indium cold pressing technique was employed. A small amount of indium was put on the pad and then it was pressed using a toothpick. An Au wire was put on the flattened indium area and then another piece of indium was pressed from the top. The prepared sample was mounted in a cryogenic system. Because the transition temperature of bulk aluminum from the normal state to the superconducting state is ~1.14K [39], the electric measurements had to be performed at a lower temperature.

Two cryogenic systems [43,44], a 1K-pot cryostat and a ^{3}He-^{4}He dilution refrigerator were available for the purpose. The principle of operation of the two systems is similar in the sense that both use an evaporative cooling technique. For the former, by mechanically pumping the vapor above liquid ^{4}He, the energetic particles in the liquid have a better chance to escape from the liquid system breaking the particle-particle bonding. Through this process the liquid loses the most energetic particles, so its average kinetic energy is reduced and the temperature drops. It is the same mechanism that makes us feel colder when a wet surface on our skin is fanned. In the actual system a small pot that is connected to the pumping line is installed inside a vacuum can. The can will be completely immersed in a liquid ^{4}He bath while the cooling progresses. Liquid ^{4}He is transferred from the bath to the small pot through a feeding tube. A mechanical pump runs to reduce the vapor pressure above the liquid ^{4}He in the pot.

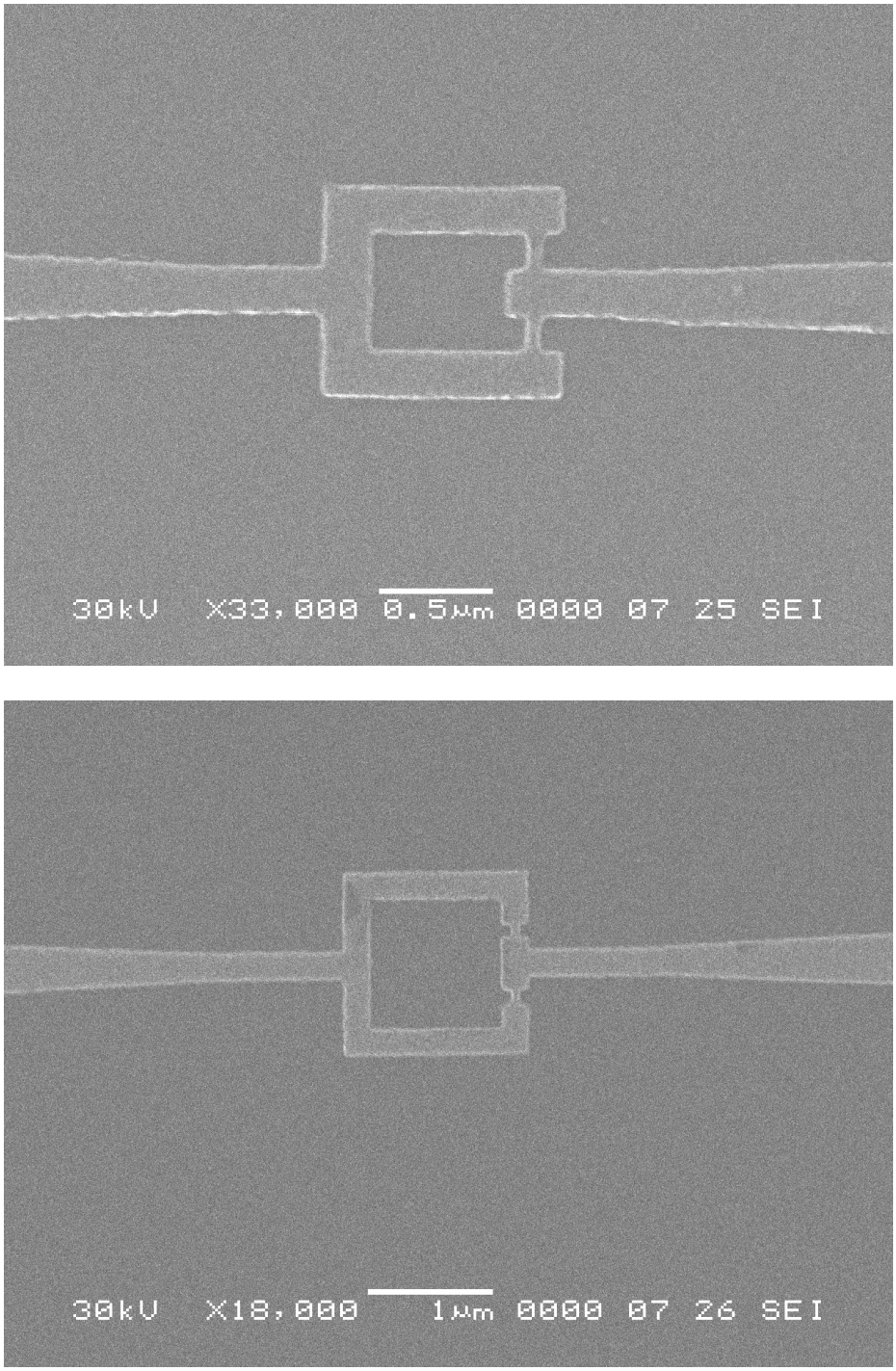

Fig. IV-6.SEM images for the SQUIDs made of aluminum films.

Samples to be measured are mounted on a small holder which is made of a good thermal conductor, and the holder touches the bottom of the pot via a thermal conducting bar, the so-called 'cold finger'. With an ideal vacuum condition in the can and the best pump, the temperature reaches close to 1 K. In practical operation the system could get ~1.1 K which is barely low enough to achieve the superconducting phase transition with an aluminum sample. However, thin film aluminum has a higher transition temperature than that of bulk aluminum. Also, proper oxygen concentration of an aluminum film can increase the transition temperature up to more than 2 K [45, 46]. Therefore, by preparing a controlled oxygen environment inside the evaporation chamber, one can produce aluminum SQUIDs that functions properly with the cryostat.

A ^{3}He-^{4}He dilution refrigerator has much in common with the above discussion. The most significant difference between the 1K-pot cryostat and the ^{3}He-^{4}He dilution refrigerator is the two phases of helium divided by an interface where a diffusion process happens. In the latter a ^{3}He rich phase and a ^{3}He dilute phase play the role of the liquid ^{4}He and the vapour in the 1K-pot cryostat, respectively. Two important facts regarding the properties of ^{3}He and^{4}He are that liquid ^{4}He is a Bose liquid and liquid ^{3}He is a Fermi liquid. Pure liquid ^{4}He transits to a superfluid state below 2.18K and pure ^{3}He also becomes a superfluid at a few mK. Thus, at temperatures below 2.18K and above the transition temperature of ^{3}He, the pure liquid ^{4}He acts like empty space with no impedance to the flow of ^{3}He, which is still a highly viscous liquid. For a mixture of these two liquids, ^{3}He and ^{4}He, the aspect of the transition for the liquid ^{4}He is modified. As the concentration of the liquid ^{3}He is increased the temperature of the superfluid

phase transition of liquid ^{4}He is lowered. With a ^{3}He concentration of 67.5% the transition temperature of liquid ^{4}He becomes 0.87K, and below this temperature the mixture of liquid ^{3}He and ^{4}He is separated into two liquid phases (see appendix A). In one phase ^{3}He is more abundant than ^{4}He, so it is called as the ^{3}He rich phase. The other phase is just the opposite and is therefore called either the ^{4}He rich phase or the ^{3}He dilute phase. The concentration of ^{3}He in each phase depends on the temperature, and at the lowest temperature the ^{3}He rich phase contains almost pure ^{3}He. However, even at the lowest temperature the ^{4}He rich phase is not pure but contains about 6.6% ^{3}He. This non-zero residual concentration of ^{3}He at the lowest temperature is the crucial point for the operation of a dilution refrigerator. With the general picture of the phase separation in the ^{3}He and ^{4}He mixture, the cooling mechanism of a dilution refrigerator is very much similar to the previous system. ^{3}He and ^{4}He gases which are properly mixed are liquefied and collected in a chamber, the so-called mixing chamber, forming a phase boundary inside the chamber. Because ^{3}He is lighter than ^{4}He, the ^{3}He rich phase will be floating on top of the other phase. In the situation where the liquid ^{4}He is superfluid, the ^{3}He impurities in the ^{4}He rich phase feel an almost free space, like water molecules in the air above a surface of water. In the other liquid phase, the ^{3}He rich phase, the major particles are fermions repulsing each other. Thus, the energetic ^{3}He atoms in the upper phase evaporate or diffuse across the phase boundary downward into the dilute phase, breaking the bonding between the ^{3}He atoms. This process results in cooling of the mixing chamber. Like in a 1K-pot cryostat, the diffusion of the ^{3}He atoms across the phase boundary in a dilution refrigerator will be promoted by reducing the density of the

^{3}He in the dilute phase. This can be achieved by removing the ^{3}He atoms from the dilute phase somehow. In order to perform this work a tube is attached to the ^{3}He dilute phase, and the tube is connected to a small chamber, the so-called still, via several heat exchangers. In the heat exchangers the tube is thermally coupled with another pipe that is used for liquefying the ^{3}He and ^{4}He mixture gas to condense it into the mixing chamber. Therefore, while the liquid of ^{3}He dilute phase moves from the coldest spot to the still, it gains a heat from the exchangers. When it reaches the still, the ^{3}He atoms are removed from the liquid surface by a mechanical pumping process. The temperature of the still is around 0.3K due to the evaporative cooling of the ^{3}He. In order to improve the power to remove the atoms the still is electrically heated to about 0.7K where the vapor pressure of the ^{3}He is two orders of magnitude larger than the vapor pressure of ^{4}He. As a result, this pumping process in the still makes the density of the ^{3}He in the ^{3}He dilute phase in the mixing chamber lower, promoting the diffusion of ^{3}He atoms from the ^{3}He rich phase to the dilute phase. The ^{3}He removed from the still is returned to the mixing chamber through a circulating loop by a specially designed pumping system, keeping the cooling process continuous. With the best performance, a commercial dilution refrigerator can reach down to a few millikelvin.

A SQUID sample was mounted in a home-built dilution refrigerator system. In order to examine the relation of the critical measuring current to an applied magnetic field, a lock-in amplifier was used to generate AC-currents (f=5~7Hz) on the SQUID sample. The circuit diagram for the I-V measurement is shown in Fig. IV-7.

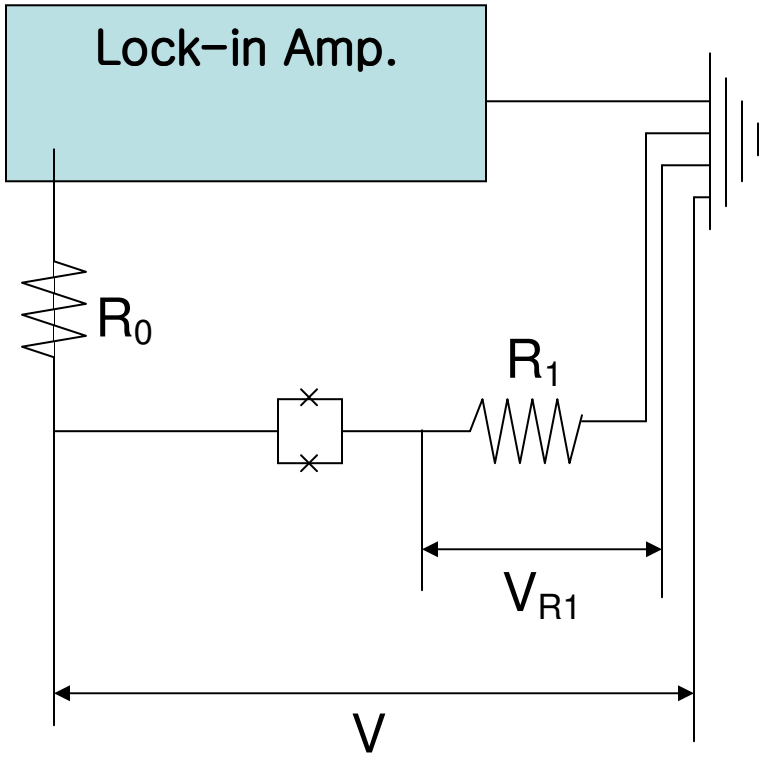

Fig. IV-7. A block diagram for the circuit to measure the critical current of the SQUID. The square loop including two x-marks is the SQUID.

The two resistors, R_0 and R_1, were used to limit the current on the SQUID and to measure the current, respectively. The I-V characteristic graph of the SQUID is shown in the oscilloscope image [Fig. IV-8]. In the graph the y-axis indicates the voltage (V_{R_1}) across the reference resistor (R_1) that defines the current passing through the device (V_{R_1} / R_1), and the x-axis gives the voltage (V) across the device, the reference resistor (R_1), and the wires. The origin was off by intention to observe the transition clearly. The measurement was performed at 600mK.

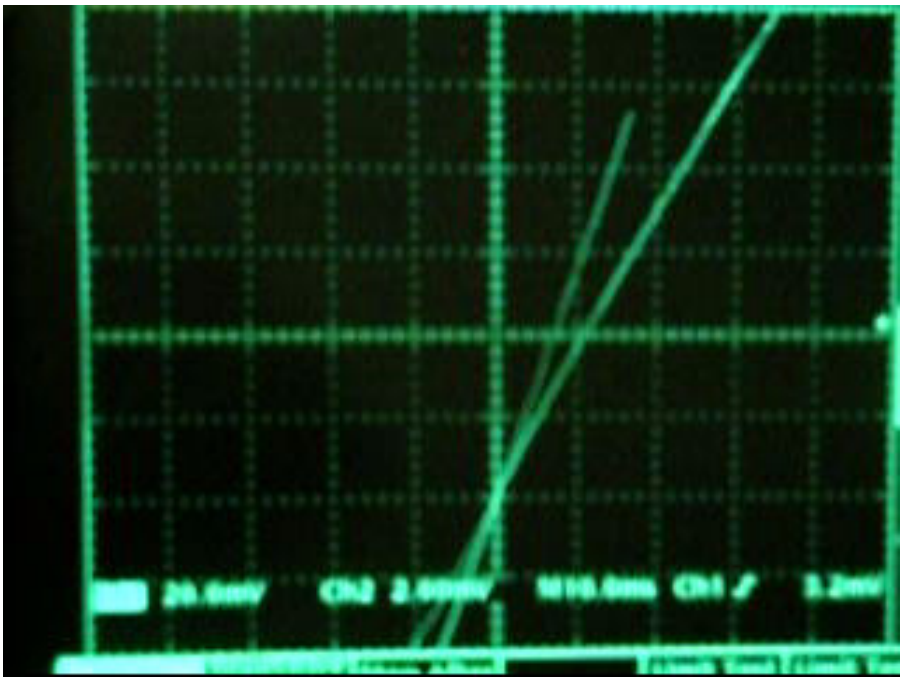

Fig. IV-8. The oscilloscope image for the I-V characteristic of SQUID measured with the setup shown in Fig. IV-7

As an applied magnetic field perpendicular to the SQUID loop was slowly increased the critical current, V_{R_1} / R_1 with the V_{R_1} where the straight horizontal line appears in the oscilloscope graph, was oscillating up and down as shown in Fig. IV-9. This changing critical current was monitored by a critical current measurement box (see appendix B), which measures the current value corresponding to a chosen voltage in an I-V curve of a samples. The threshold voltage on the box, V_{th}, was set between the two vertical lines shown in Fig. IV-9 in order that the box show the changing critical current $I_{c.}$ The first graph of the critical current measured with the box was plotted as a function of the applied magnetic field in Fig. IV-10.

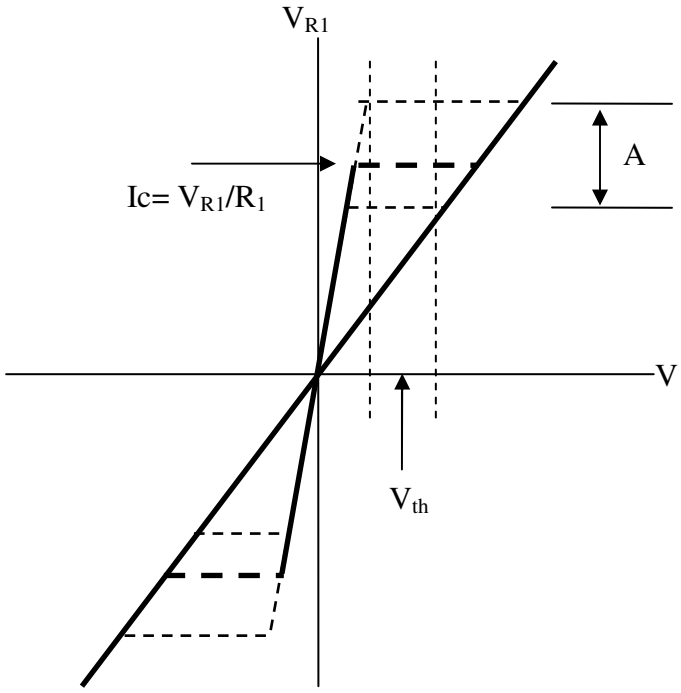

Fig. IV-9. I-V curve of SQUID in the presence of an applied magnetic field. The *A* means the modulation amplitude of the critical current I_c.

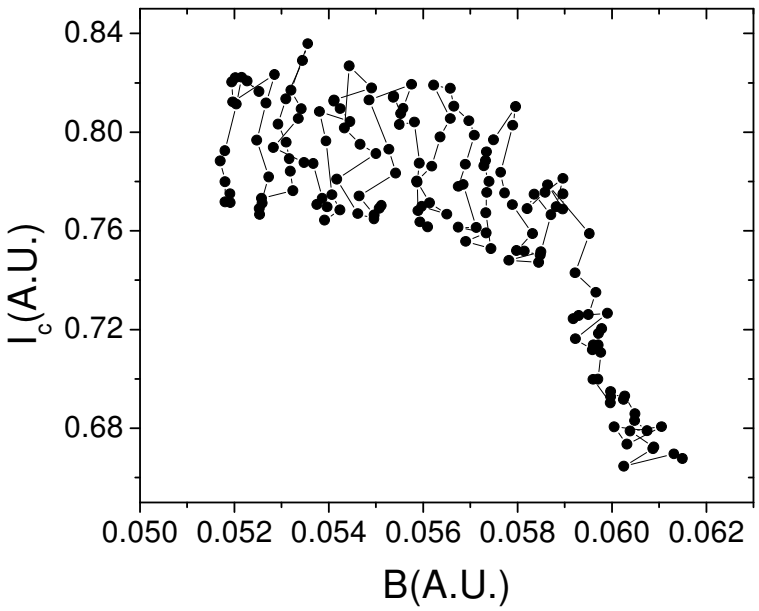

Fig. IV-10. The critical current I_c vs. magnetic flux density B for a SQUID.

In this graph the data acquired from the critical current measurement box are used for the critical current I_c with an arbitrary unit and the current flowing through the superconducting magnet acquired simultaneously are used to define the magnetic field. The chaotic result is due to the noisy data for the current on the magnet. In order to get the current on the magnet the voltage across a shunt resistor (R=$10^{-4}\Omega$) connected in series to the magnet was measured. The data for the current on the magnet is shown in Fig. IV-11. In the figure, the current was calculated with the voltage across the shunt resistor, and was plotted as a function of the sampling time.

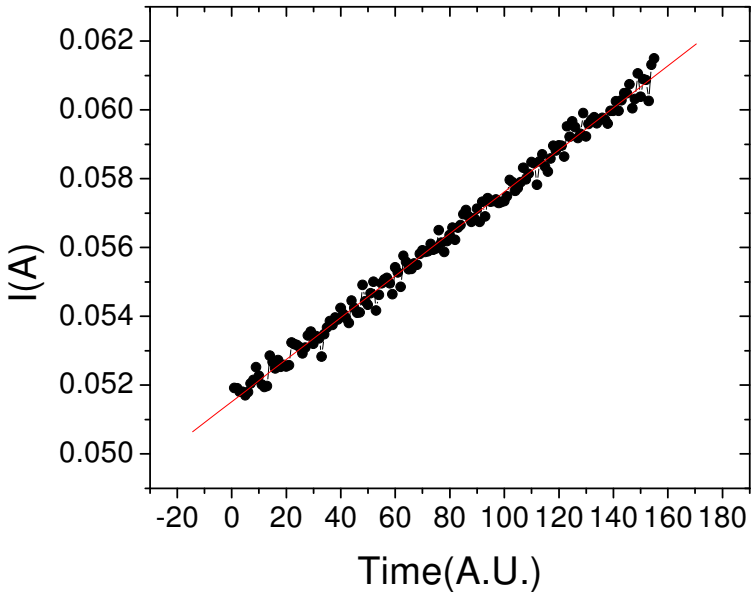

Fig. IV-11. The current *I* on the superconducting magnet as a function of the sampling time. The straight line is fitted to a linear function.

The commercial superconducting magnet used in this experiment had a characteristic that the current flowing through the magnet of 8.13A creates a magnetic field of 1T. With the magnet feature and a linear function fitted to the I_c-*Time* data shown in Fig. IV-11 the chaotic graph, Fig. IV-10, was redrawn in Fig. IV-12 with a magnetic field in gauss. The oscillating critical current with a period of ~13gauss clearly appears in the figure. However, the final result revealed a problem regarding the magnet. Because the magnet is not designed for such a small magnetic field, it was very difficult to control

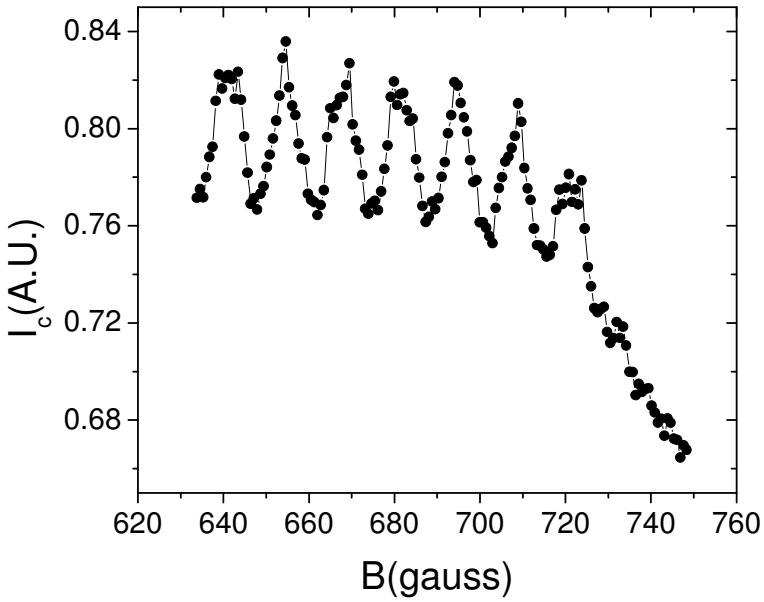

Fig. IV-12. The critical current I_c vs. magnetic flux density B in gauss.

the magnet at the small scale and to remove the residual magnetic field completely. Therefore, the graph shows a large offset at the beginning of the magnet charging. A small superconducting magnet was built to solve this problem. The design of the magnet was a simple solenoid type with two additional coils at the ends of the solenoid to compensate for the weak flux density at the edges. NbTi wire was used and a phenolic tube which has a dimension comparable with the cryogenic system was chosen for the magnet former. The number of turns and the optimum location of the additional coils for an intended uniform magnetic flux density were calculated using a computer simulation program (Visimag. v3.15, 30 day trial version). The turns were wound using a coil

winder with a properly adjusted tension in order that kinks and twists do not appear. Each layer of the multilayer coils was glued down with a thin layer of Stycast. Characteristics of the small magnet were investigated at room temperature using a Hall probe. A magnetic flux density at the center of the solenoid was measured while a current on the solenoid was increased and plotted as a function of the current in Fig. IV-13. The current was estimated from the voltage across a shunt resistor ($50mV/1.5A$) which is connected to the solenoid magnet in series, and the background magnetic field was compensated using an offset controlling knob in the Hall probe before the measurement. The linear function fitted to the acquired data gives the relation of magnetic flux density B to current I, $B(\text{gauss})=133.3\times I(\text{A})$. The homogeneity of the magnetic flux density inside the solenoid was inspected by moving the Hall probe 2 cm above the center, 2 cm below the center, to one side and to the opposite side of the solenoid, sequentially, while the magnetic flux was measured at a constant current. The resulting data is shown in Fig. IV-14. The largest magnetic flux density (-12.97 gauss) among the data points is ~0.5% different from the magnetic flux density (-13.04 gauss) measured at the center of the magnet.

The small magnet was installed in a dilution refrigerator with a SQUID. The same circuit as shown in Fig. IV-5 was constructed for a critical current measurement. 10 kΩ and 71 Ω resistors were used for R_0 and R_1. At a fixed B that was perpendicular to the SQUID loop, the critical current was measured using an oscilloscope. The two periodic waves for the voltage V and V_{R1} in Fig. IV-5 were monitored on the oscilloscope as a function of time.

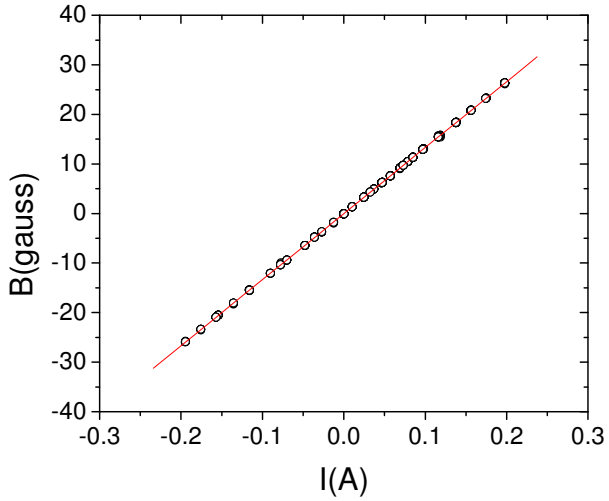

Fig. IV-13. The magnetic flux density at the center of a solenoid magnet vs. the current on the magnet.

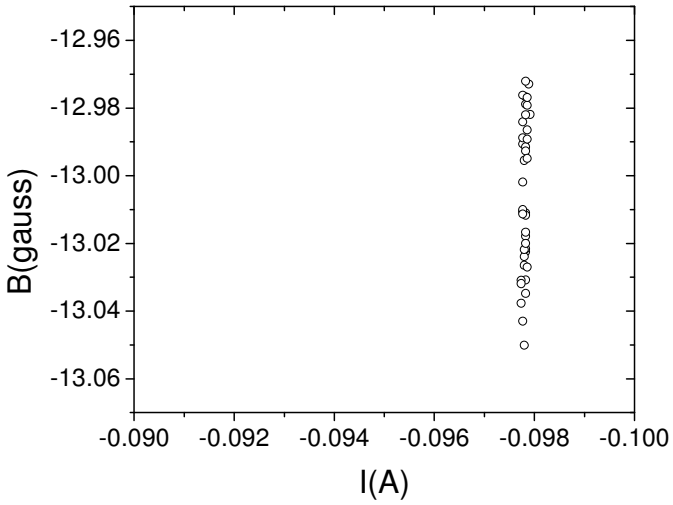

Fig. IV-14. The deviation of the magnetic flux density inside a solenoid magnet at a constant current.

A sudden surge of voltage on the graph for V was observed at a certain voltage of V_{RI}, as shown in Fig. IV-15. This sudden change of the amplitude indicates a transition of the device, and the current at the point (V_{RI}/R_1) corresponds to the maximum measuring current I_c. Because the generated AC-current is sinusoidal, the time t_T where the transition happens is related to the I_c as

$$I_c = \frac{V_m}{R_1}\sin(2\pi f \cdot t_T), \tag{IV-24}$$

where V_m is the maximum amplitude of the voltage V_{RI} and f is the frequency of the AC-current. The graph in Fig. IV-16 shows the relation of the critical measuring current (I_c) to the applied magnetic flux density (B). The interval between the data points along the magnetic flux density (B) was ~2 gauss and the background magnetic field was not subtracted. The measurements were performed with a SQUID that has an area inside of the loop of $1\times 1\mu m^2$ at 70mK. From IV-15 a period of the oscillation expected with the SQUID was ~21 gauss, but the result shown in Fig. IV-16 is 15 gauss. A possible explanation of this discrepancy is that, because of the penetration depth, there could be an additional region where a magnetic flux can penetrate through the superconducting film, creating a larger flux passing area. The depth of modulation of the critical current is also smaller than would be expected. This is probably because of the appreciable screening current in a real device. In the theory, the self induced magnetic flux by a screening current was ignored.

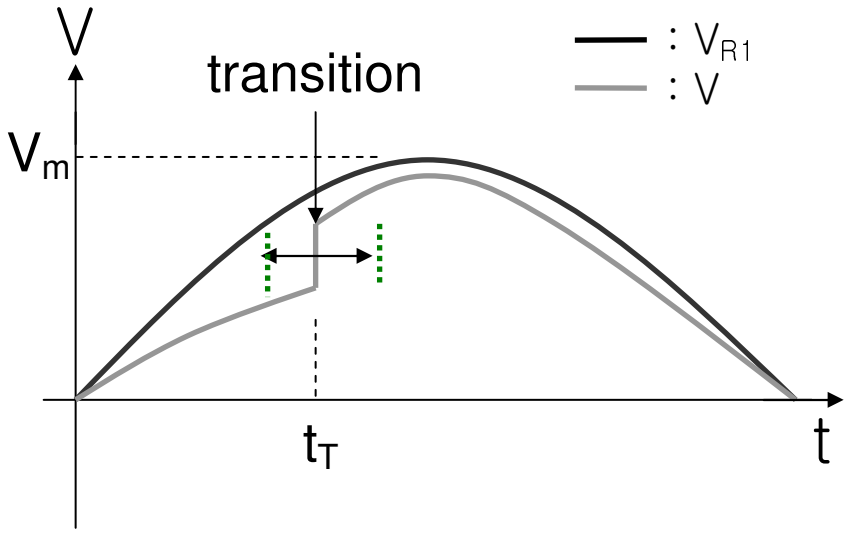

Fig. IV-15. The voltages V and V_{R1} plotted simultaneously as a function of time t.

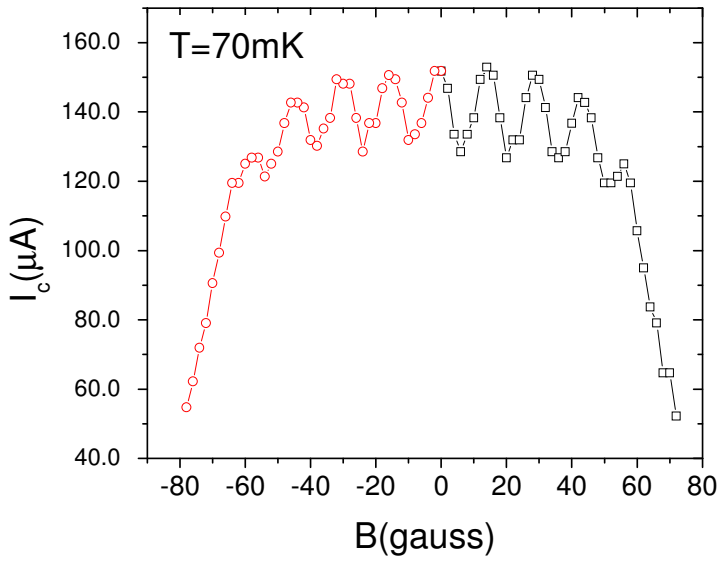

Fig. IV-16. Critical measuring current I_c vs. applied magnetic field **B** measured at 70mK.

However, in reality the induced flux could be comparable with the flux quantum depending on the design of the device. In this case the depth of modulation of the critical current is reduced. [38]

A direct magnetic measurement of the patterned structures of Mn_{12}-acetate, will be developed by a well known approach [47]. Once a reliable SQUID with a proven analysis scheme is ready to operate, the device is mounted such that an applied magnetic field is parallel to the SQUID loop. This configuration is crucial in a real measurement of a small magnetic system using an Al-SQUID. The thin film superconducting device will reach the regime where it does not work properly even with a very small applied magnetic field if the field is perpendicular to the loop as shown in Fig. IV-16. However, a thin superconducting film can withstand a fairly high magnetic field in parallel to the surface [48], and this property allows one to have a wide range of magnetic field for operation of a SQUID, as long as the alignment of the magnetic field is successfully achieved. In addition, the perfectly aligned magnetic field will not pass through the loop providing modulation of the critical current. Therefore, any change of the critical current observed while the applied field is increased can be interpreted as a variation of magnetic flux purely due to the change of magnetic state of the test magnetic systems near the loop. A characterization of the critical measuring current for a SQUID loop in parallel to the applied field will be acquired to learn about the background flux. A portion of the SQUID loop will be covered with a Mn_{12}-acetate film pattern using the technique introduced earlier. Finally, the critical measuring current will be monitored

while a magnetic field is increased, and then the data will be compared with the background signal for the magnetic study of the film structure.

Thus far an overview of theoretical working principle for SQUIDs, a method to fabricate the device, and some data on the sample devices have been presented. Although the analysis required for the direct magnetic measurement on a Mn_{12}-acetate film structure have not yet been performed, the devices which were generated by the EBL technique showed a varying critical measuring current that is coupled with the magnetic flux inside the SQUID loop. As mentioned in the earlier chapter, a film of molecular magnet could be deposited on the micro/nano-device using EBL. By virtue of an advanced system, such as a laser stage for SEM, a more delicate alignment of the PMMA film mask could be accessible. Therefore, a positioning of the test magnetic system on the devices will become more flexible, providing an active way to construct a strongly coupled structure. As a conclusion, this project to perform a direct magnetic measurement on an artificially isolated SMMs pattern will, in principle, proceed toward the ultimate goal. In addition the inconsistency between the theory for an ideal case and the practical data from a real sample motivates one to examine the device more rigorously as a side project. First, as mentioned above one needs to produce the extremely weak link. This will impose a strong limitation on the circulating current and therefore one can expect a larger depth of modulation. This will be achieved by reducing the width and increasing the length of the junction. In order to study a dependency of the flux passing area to the penetration depth, one can change parameters that affect the basic properties of superconducting materials. The thickness and the concentration of an

impurity of the superconducting film are suitable parameters. Comparative experiments on two identically designed SQUIDs but containing different parameters is a proper approach for the study. A choice of design and location for the weak links and the dimensions of the loop are also interesting parameters for the basic study of SQUIDs.

In the next chapter a couple of experiments are performed to investigate an interaction between superconducting films and SMMs. The topic is quite interesting not only because this type of coupled system could be an important issue in the future study of molecular magnets using a superconducting device, but also because the interaction of magnetism and superconductivity has been a topic of fundamental interest.

CHAPTER V

THE INTERACTION BETWEEN SUPERCONDUCTORS AND SINGLE-MOLECULE MAGNETS

Introduction

Superconductivity and magnetism are two major areas of importance in condensed matter physics. There has been innumerable work considering their relationship based on the phenomenological fact that superconductors in a weak magnetic field act as perfectly diamagnetic bodies. The transition from the superconducting phase to the normal phase at the so-called critical field, one of the empirical observations of superconductors from the beginning, was a big obstacle to use these unusual non-dissipative systems in various applications. Therefore, it has been an important issue to figure out the origin of this transition and to discover advanced materials, which have higher critical fields. It became clear that the preferential spin configuration of the paired electrons in the condensed phase could be linked to a mechanism to destroy the superconductivity. Actually, the central aspect of the spin configuration for the paired electrons in the superconducting state is mainly opposite of ferromagnetic systems in which adjacent spins are aligned in the same direction. Nevertheless, more recently people have started thinking of physical phenomena which appear when these two mutually exclusive states of matter, superconductivity and ferromagnetism, are combined in a unified system, a so-called Ferromagnet-Superconductor Hybrid system (FSH) [49]. They have inferred from theoretical and experimental studies that there is a possible interaction between the

two subsystems provided by magnetic flux in the magnetic system and supercurrents in superconductors. Already many interesting phenomena arose from the ferromagnet-superconductor systems. In particular, strong vortex pinning has been reported for superconducting film covering ferromagnetic layer [50~52] and arrays of ferromagnetic dots [53~55]. They argue that the magnetic domain structure in the ferromagnetic layer enhance the pinning of vortices in the superconducting layer. The recent experimental work demonstrated that in a hybrid system where a Pb film covers a Co/Pt multilayer with perpendicular magnetic anisotropy the pinning properties of the Pb film can be controlled by tuning the size, density, and magnetization direction of the domains. This vortex pinning effect is more clearly observed in a hybrid system including arrays of ferromagnetic dots. It has been observed that the superconducting state of Nb films is modulated by magnetic field generated by the two-dimensional square/triangular arrays of ferromagnetic dots (Ni and Co) which are lithographically fabricated. The periodically modulating magnetoresistance (depending on the dimension of the array structure) is a clear evidence of the vortex pinning effect.

Observing the motion of supercurrents in superconductors coupled with a system consisting of SMMs should be another exciting challenge because of the abnormal variation of magnetic flux from the SMMs, which are discriminated from a normal ferromagnet in magnetic ordering. For now it is not achievable to organize the molecules in an oriented state, so the study on any elegantly coupled system where the oriented magnetic molecules are arranged in an artificial way is not possible. However, the technique to fabricate thin films of SMMs [34] allows us to perform some

experiments on a new type of hybrid system. In this chapter the first try attempt to understand the behavior of paired electrons in a superconducting system coupled with SMMs is introduced.

Approach

As an elementary step to study the mutual interactions between two subsystems, one can observe physical properties of a primary system, which is coupled with a secondary constituent and compare them with results coming from the pure primary system. If there is any dissimilarity found between the two cases, it would be a clue towards interpreting the interaction. For the purpose of this argument, in this experimental work magnetoresistances, critical currents and critical temperatures of two identical aluminum films playing the role of the primary system are measured at various temperatures in the presence of magnetic field. Importantly, one of the aluminum films makes a contact either directly or indirectly with the Mn_{12}-acetate film, unlike the other as shown in the next section.

Sample preparation

First, two pieces of substrate cut from a Si/SiO_2 wafer were prepared via a cleaning process in which acetone, 2-propanol and N_2 gas were sequentially sprayed onto the surface of the substrates. The solution evaporation technique [34] to deposit Mn_{12}-acetate on Si/SiO_2 surfaces was chosen. A droplet of the liquid, which was prepared by

sonicating the Mn_{12}-acetate powder in 2-propanol, was transported onto the surface of the prepared substrate using a pipette. The liquid film formed on the substrate was dried in air completing the creation of a thin film layer consisting of the Mn_{12}-acetate molecules and clusters. Then the sample was mounted on a sample holder inside an evaporation chamber together with the other piece of the pristine substrate. Each sample was then covered with shadow masks which are identical. As a final step, a thin aluminum film of ~250Å was simultaneously deposited onto the two substrates by thermal evaporation with a rate of ~4 Å /sec. A 99.9% pure aluminum pellet was melted for the evaporation in a vacuum of ~ 6×10^{-6} Torr. One of the aluminum films made a direct contact with the Mn_{12}-acetate film. The whole procedure is depicted obviously in Fig. V-1. Two scanning electron microscope images for the resulting samples are shown in Fig. V-2, indicating in a brighter tone the aluminum film patterns which are almost identical in dimension. The right image shows a more inhomogeneous surface because it is covered with the Mn_{12}-acetate molecules and clusters which contact with the aluminum film directly. In another experiment, investigating an indirectly coupled hybrid system in which the Mn_{12}-acetate film did not have direct contact with an aluminum film, two aluminum films of ~100Å were evaporated simultaneously on two separate substrates that were covered with the identical PMMA film masks created by EBL [See Chapter III]. A 99.9% pure aluminum pellet was melted for the evaporation in a vacuum of ~ 4×10^{-6} Torr. Both samples were dipped into acetone for a lift-off of the PMMA.

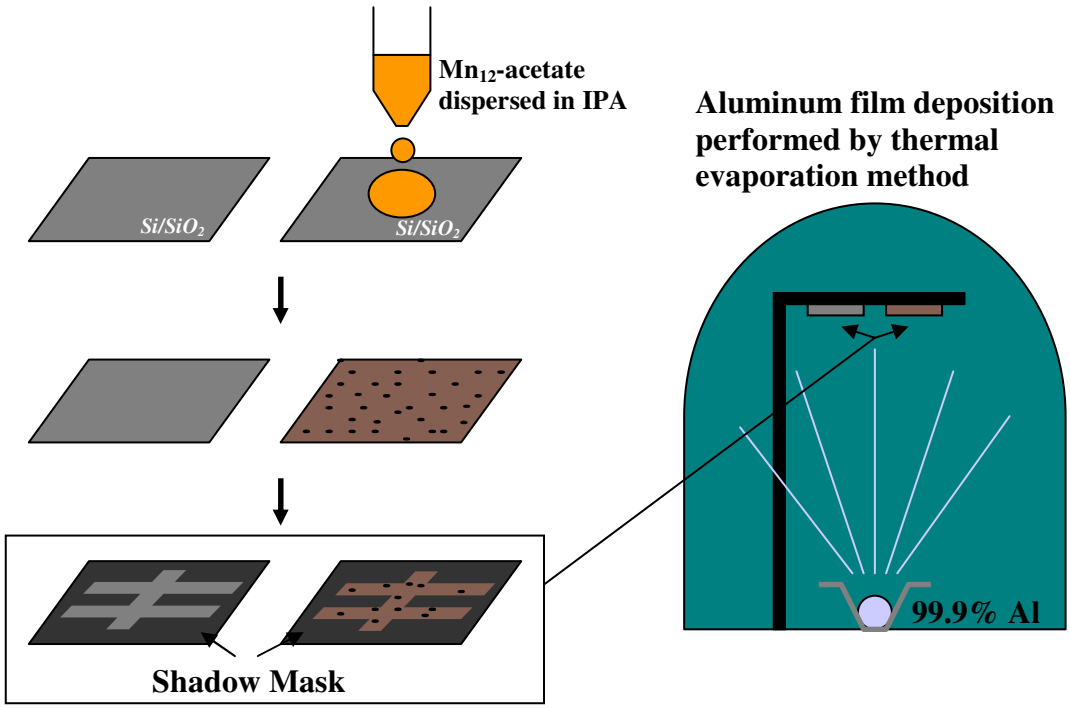

Fig. V-1. Schematic diagram for the procedure of sample preparation.

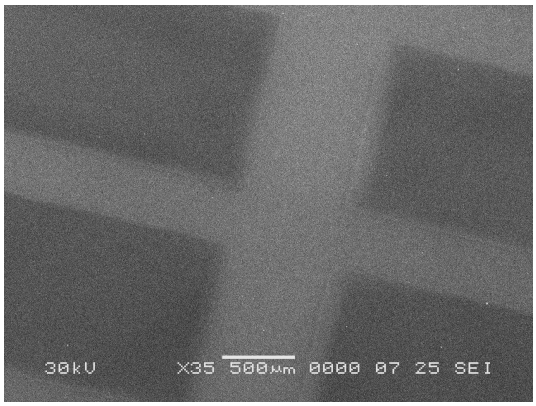

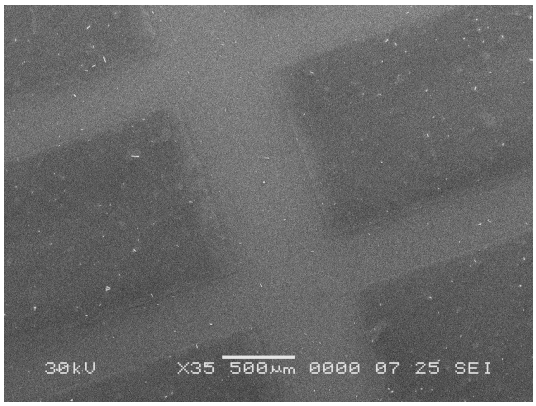

Al/Al_2O_3 Mn_{12}-ac/Al/Al_2O_3

Fig. V-2. SEM images of the aluminum film patterns generated by the procedure described in Fig. V-1.

The shape of the patterned aluminum film device is shown in Fig. V-3. As a final step, a Mn_{12}-acetate film was deposited on one of the two identical patterned devices by the dropping and drying process. Because of the native oxide layer grown on the aluminum film surface, the expected cross-sections of the resulting samples are like Fig. V-4. In the superconductor/SMMs hybrid sample the aluminum oxide layer prevents the molecular magnets from directly coupling with the superconducting layer.

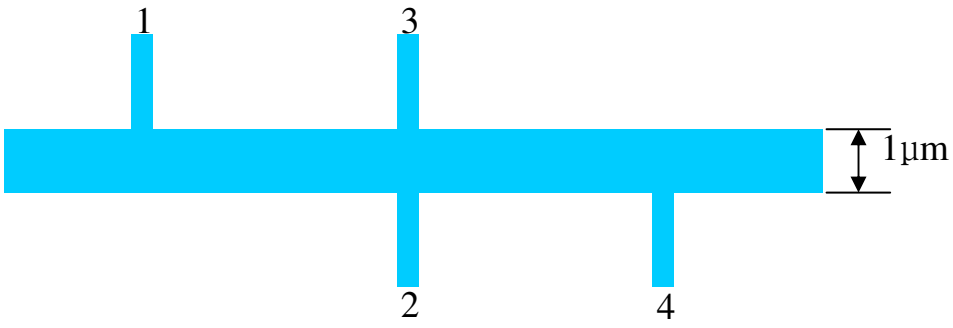

Fig. V-3. Aluminum film pattern for 4-contact measurements. The narrow stripes with numbers are the voltage probes.

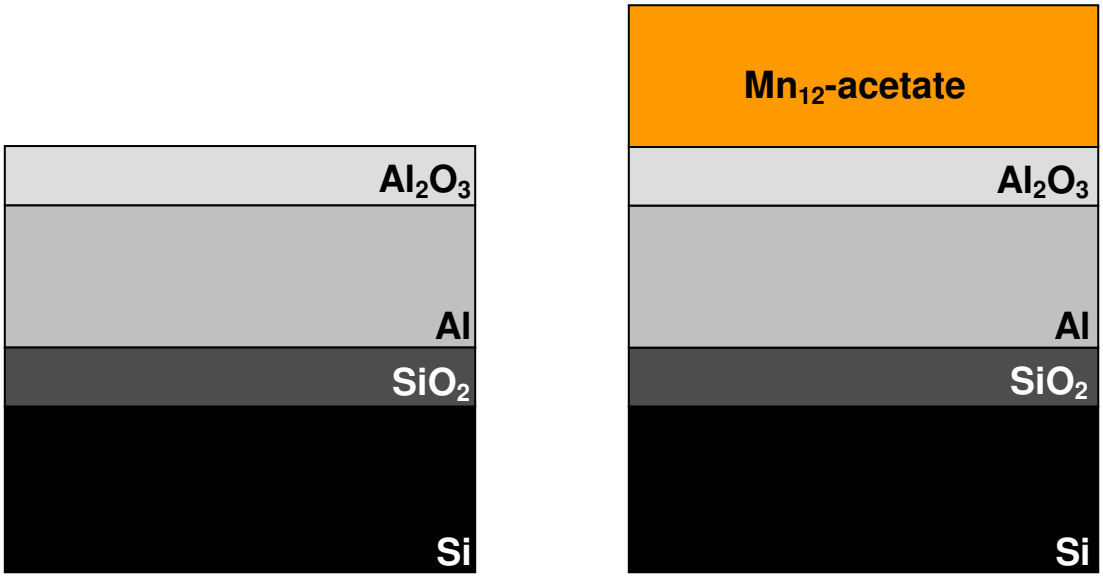

Fig. V-4. The cross-sections of two aluminum film samples for a control experiment. In the coupled sample (right) the molecular magnet film is separated from the aluminum film by an aluminum oxide layer.

Measurements

Measurements for the directly coupled hybrid system were performed using the conventional 4-contact AC method in the experimental setup described in Fig. V-5. Two lock-in amplifier were used to generate AC-currents (f=13Hz) on each sample separately. Resistors of 100kΩ were connected to each circuit in series to define currents ($I=V_{out}/10^5\Omega$) flowing thorough the main channels of the samples whose resistance values are ~5Ω at room temperature. Samples were mounted inside a home-built dilution refrigerator for low temperature measurements. The samples were mounted perpendicular to the applied magnetic field H. V_{21}, the voltage between the leg 2 and 1, and V_{24}, the voltage between the leg 2 and 4, were measured while varying temperature from 200mK to room temperature and magnetic field up to 3T. In this experimental setup V_{21} is converted to the longitudinal resistance ($R=V_{21}/I$) of the film stripe and V_{24} is the Hall voltage V_H. The resistance of a nearby ruthenium oxide thermoresistor and a calibrated germanium thermoresistor were recorded during the measurements in order to define the experimental temperature. Similarly, measurements on the indirectly coupled hybrid system were also performed using this conventional 4-contact AC method. $V_{12,}$ the voltage between the leg 1 and 2 in the Fig. V-3 was measured for the control experiment.

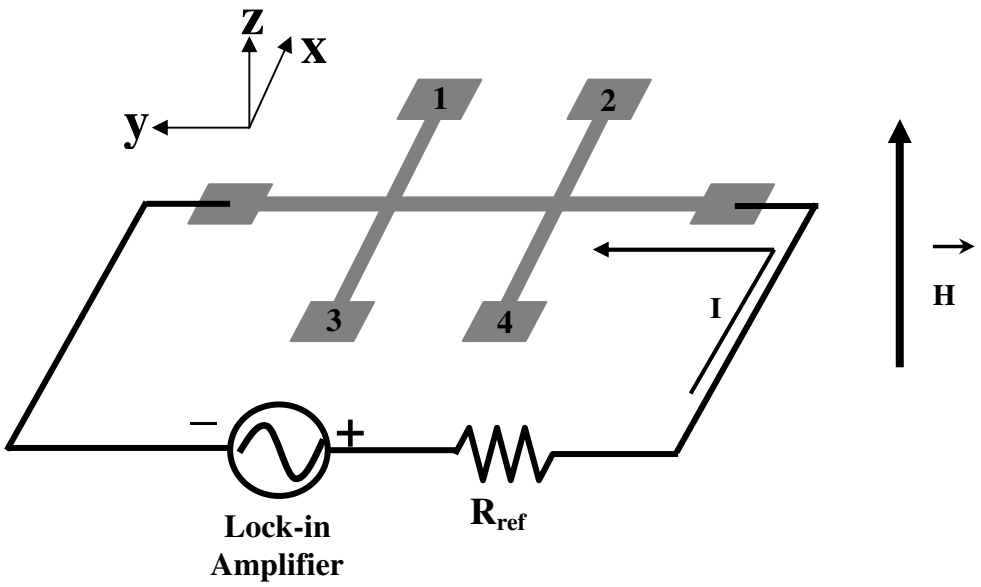

Fig. V-5. Diagram of the circuit for the 4-contact AC measurement.

Analysis

The longitudinal resistance of the samples obtained from V_{21} measured at 200mK is plotted as a function of the applied magnetic field H in Fig. V-6. The magnetic field was swept from 0 to 3T with a ramping rate of 4.8mT/sec. Two different AC measuring currents, 10^{-5}A and 10^{-6} A, were generated for the measurements. Above the saturation point (~1.7T) the two samples behaves as normal ohmic materials and the resistances for different currents are in good agreement for both samples.

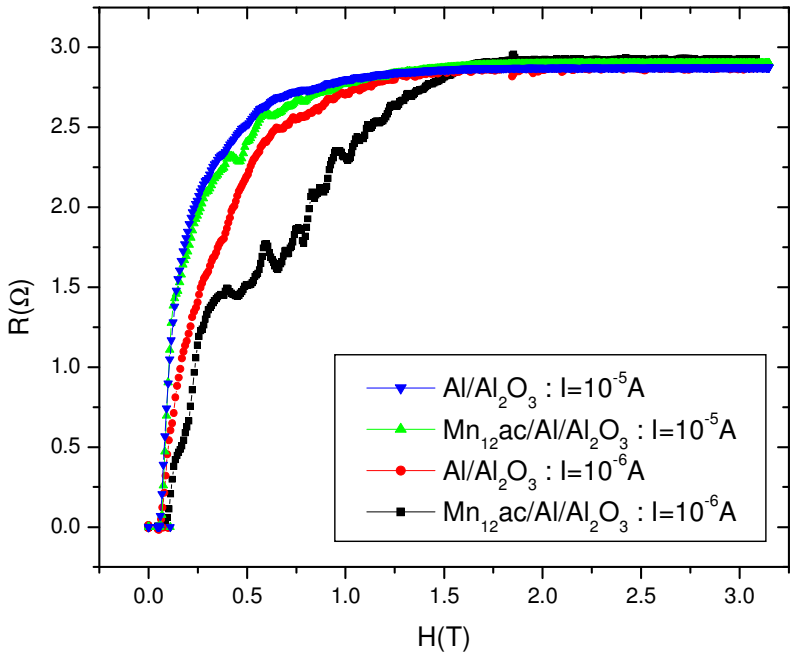

Fig. V-6. Longitudinal resistance R vs. magnetic field H up to 3T for the two samples measured with two different AC currents.

Both samples show zero resistance at low H before a sharp transition that occurs at magnetic fields below 0.1T for all the cases. The zero resistance was confirmed by observing the values of V_{21} at several different scales (full scale of 2μV~100μV). It is clear from the results that there exist three distinguishable regions, superconducting (H<~0.07T), normal (H>~1.7T), and an intermediate region. The last phase is known in general as an intermediate state or a mixed state depending on what types of superconductor they are. For type I materials it is called intermediate state and for type II

materials it is called mixed state or vortex state. Sometimes, the latter is also called the Abrikosov vortex state.

The origin of the intermediate state for type I superconductor is due to the non-zero demagnetizing factor which strongly depends on the geometry of the system. With the perfect diamagnetic property of superconductors this factor yields local points in superconducting systems where the local magnetic field intensity is the same as the thermodynamic critical field H_c even with the applied field weaker than H_c. As a result of that, it is possible for superconductors to be in a state in which the systems are formed into the coexistence of superconducting and normal phase in equilibrium having the free energy lower than the cases of pure phase. Meanwhile, it is known that the mixed state originates from the negative surface energy and appears even if the system has a zero demagnetizing factor. Unlike type I superconductors, certain superconductors have a penetration depth λ longer than the coherence length ξ and these kinds of superconductor are classified as type II superconductors. It has been proved that the exact breakpoint between two regimes is at κ=0.707, where κ is the Ginzburg-Landau constant defined by the ratio of λ to ξ and the type II material (κ>0.707) has a negative surface energy between normal and superconducting regions. Due to the negative surface energy, it is more energetically favorable for type II materials to create the surfaces forming normal domains in order that the ratio of surface to volume of the normal domains is a maximum in the presence of magnetic field. It turns out that a favorable configuration is one in which the superconductor is threaded by cylindrical geometry of normal domains so-called normal core lying parallel to the applied magnetic

field and including one flux quantum generated by a vortex of supercurrent that circulates around the core. As mentioned earlier, the Ginzburg-Landau constant κ is an important value to determine whether a superconductor is type I or type II. The parameter κ, of course, varies for different materials, and it also depends on the purity as well as the temperature. In addition to these prime factors, the geometry of a specimen is in general another significant factor to determine the type of materials. Tinkham [56] suggested that a vortex state exists in a sufficiently thin film geometry of a type I superconductor below a critical thickness d_c, and many theoretical studies and experiments to determine d_c have been done on various materials [57, 58]. More recently, direct observation of vortices in Al film using Micro-SQUID microscopy [59] has been realized. The critical thickness for aluminum determined by critical field studies [58] is ~ 2μm around the critical temperature T_c, and the thickness of aluminum films provided in our experiments is ~25nm, which is far below the critical value. Therefore, we conclude that these aluminum films more likely behave as type II superconductors rather than type I, and thus the system is filled with vortices in the mixed regime. It is shown in Fig. V-6 that the longitudinal resistances of the aluminum film coupled with the Mn_{12}-acetate layer are quite different from the values for the other sample particularly in the mixed state. They are generally lower and fluctuate appreciably. This discrepancy is more obvious for the case of less energetic measuring current. For the purpose of observing it in more detail, similar additional measurements were done at the same temperature (200mK) generating more various values of measuring currents and sweeping magnetic field from 0T to 1T where the differences are most relevant. The results for the two

Al/Al_2O

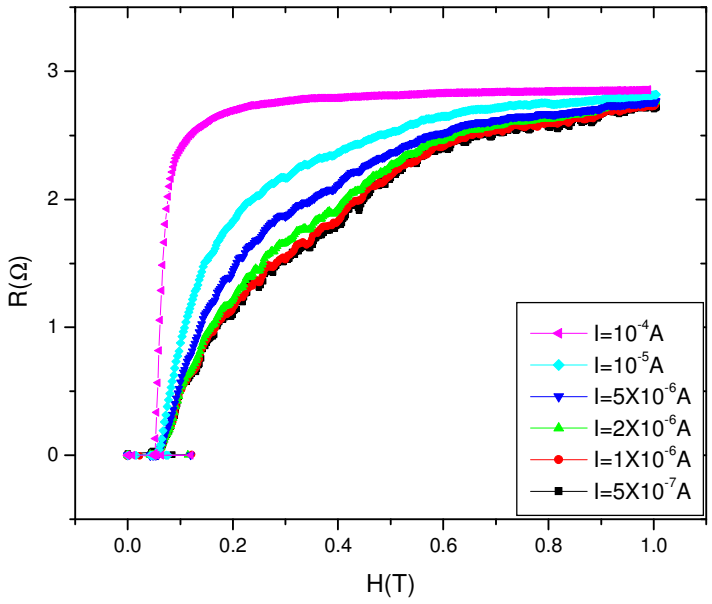

Mn_{12}-ac/Al/Al_2O_3

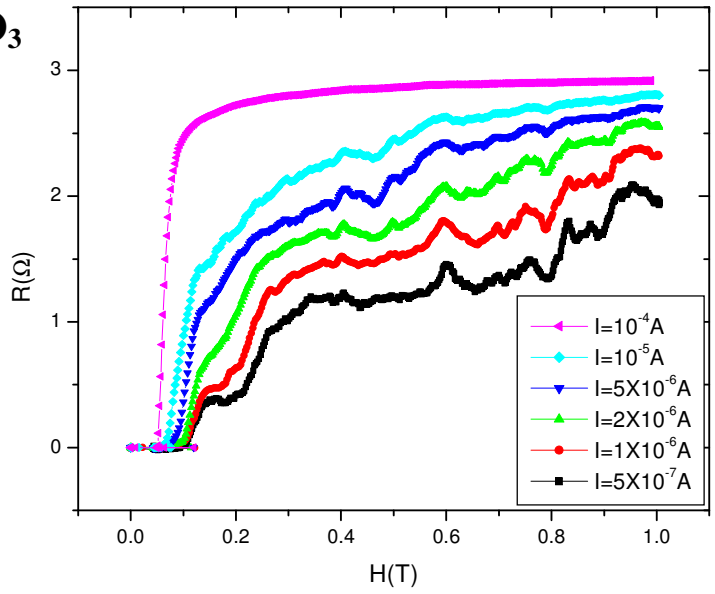

Fig. V-7. Longitudinal resistance R vs. magnetic field H up to 1T for the two samples measured with six different AC currents.

samples are plotted separately in Fig. V-7. For both samples it is observed that the resistances generally decrease as the measuring currents are reduced. This is possibly because of dissipative processes originating from the motion of the vortices in the mixed state. By the basic electromagnetic theory the vortices or the flux lines feel a force known as the Lorentz force when a current flows through the space where they are existing, and the magnitude of the force acting on the vortices is directly proportional to the current density. This force will make the flux lines tending to move transverse to the current. Then the electric charges leading the current feel, by the motion of the flux lines, an induced electric field that has a direction exactly to resist the stream of the current. Because the magnitude of the electric field is proportional to the velocity of the motion and the magnetic flux density, the resistivity from the induced field will become strengthened as the current increases. The fluctuating magnetoresistances for the sample including the Mn_{12}-acetate layer are clearly revealed in the graph. The reason for the distinctively appearing resistance of the sample is not clear at this point, but it is possibly related to the pinning of vortices. The molecular magnets and the crystals in the Mn_{12}-aceate layer underneath the aluminum film may act as sources to cause local variations of magnetic field, creating some local areas where the magnetic energy is low enough for the vortices to be trapped. These pinned flux lines, therefore, will hardly move in response to the Lorentz force. As a result of that, from the preceding argument the induced electric field that disturbs the current motion becomes smaller. This vortex pinning process surely depends on the variation of the free energy in the system, and presumably the unusual local distribution of the magnetic state in the Mn_{12}-acetate layer

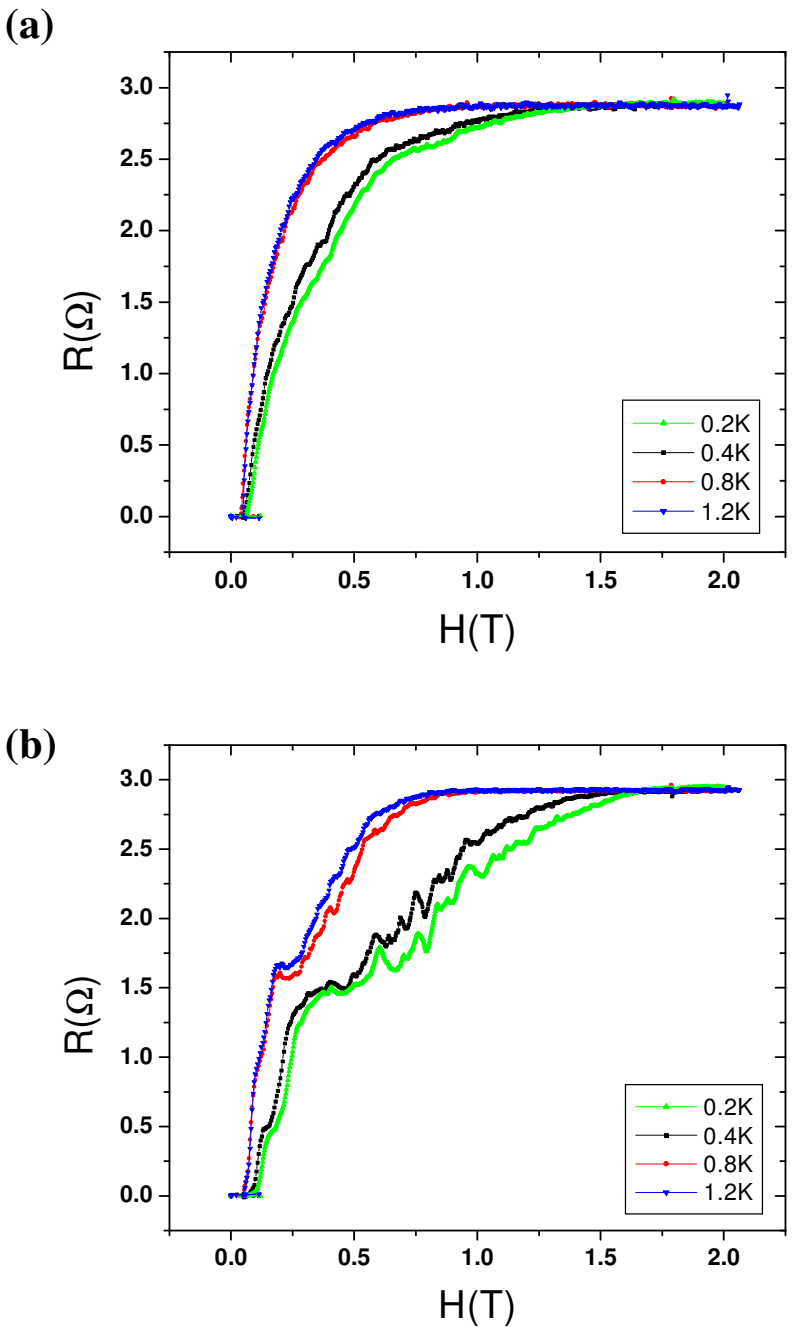

Fig. V-8A. Longitudinal resistance R vs. magnetic field H up to 2T measured at four different temperatures for (a) the Al/Al_2O_3 sample and (b) the Mn_{12}-acetate/Al/Al_2O_3 sample.

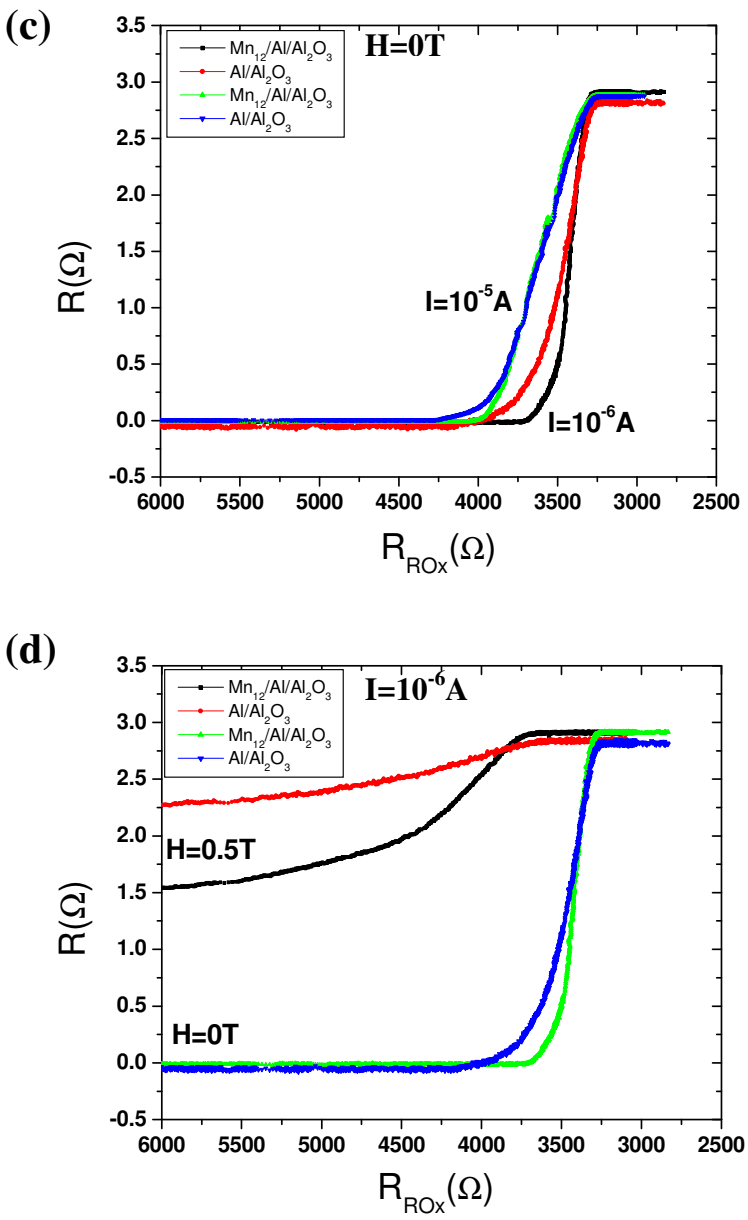

Fig. V-8B. Longitudinal resistance R vs. the resistance of the ruthenium oxide thermoresistor R_{ROx} for the two samples acquired during warming-up process (c) for two different measuring currents without magnetic field and (d) in the presence of a magnetic field of 0.5T (shown together with the case of zero magnetic field).

will affect the formation of the energy variation in addition to the inhomogeneous surface morphology, one of the prime factors for the vortex pinning.

The graphs in Fig. V-8 show the dependence of the longitudinal resistance R on the temperature. The longitudinal resistances for the two samples were measured with flowing currents of 1μA at four different temperatures changing magnetic field from 0T to 2T. The resistance of the coupled system is fluctuating in the mixed regime through all the temperature range as shown in Fig. V-8 (b). On the other hand, the resistance for the pure superconducting system is still showing monotonously changing curves in Fig. V-8 (a). The longitudinal resistances were measured continuously during the warming up process with two different transport currents without magnetic field [Fig. V-8(c)] and in the presence of the magnetic field of 0.5T [Fig. V-8(d)]. In all the cases the graphs indicate the transition behavior of the superconducting samples and the differences between the resistances in the mixed regime. In order to determine the critical currents for the samples, DC I-V characteristics of the samples are compared in Fig. V-9. DC current swept from 1mA to –1mA was generated on each sample at 200mK without magnetic field for the measurements. The graphs point out that the critical current density of the coupled system is lower than the one for the pure aluminum sample. Superconductors lose their zero resistance when the total magnetic field intensity H_T due to transport current and external applied magnetic field, exceeds the thermodynamic critical field intensity H_c. Therefore, it may be possible that the magnetic field from the Mn_{12}-acetate layer assists the aluminum strip in becoming a normal metal under the influence of the current. As defined earlier, the Hall voltages V_{24} were measured flowing

three different currents on each sample at 200mK and plotted as functions of applied magnetic field H from 0T to 3T in Fig. V-10.

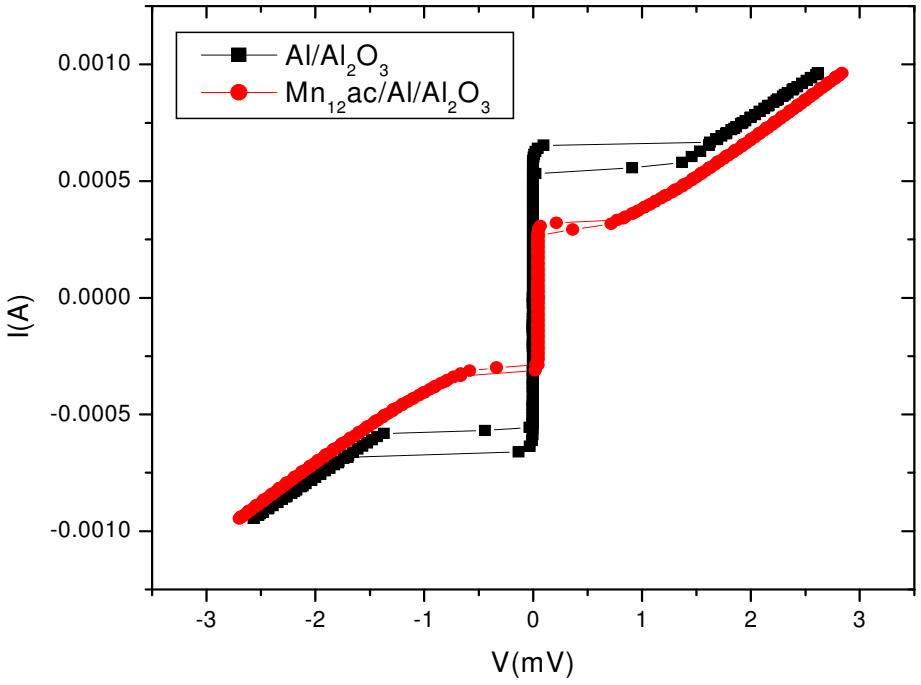

Fig. V-9. I-V characteristic curves for the two samples acquired at 200mK without magnetic field.

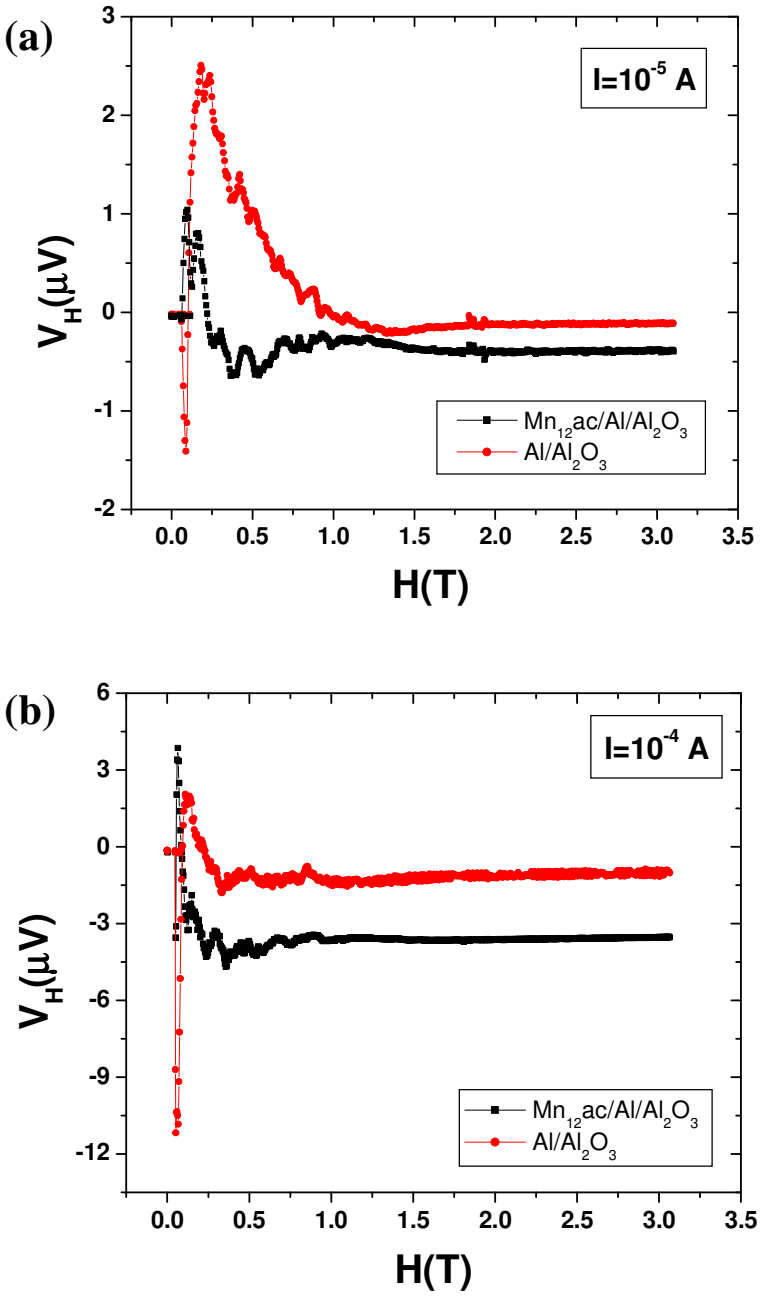

Fig. V-10. The hall voltage V_H vs. magnetic field H up to 3T for the two samples with three different measuring currents: (a) 10^{-5} A, (b) 10^{-4} A, and (c) 10^{-3} A.

(c)

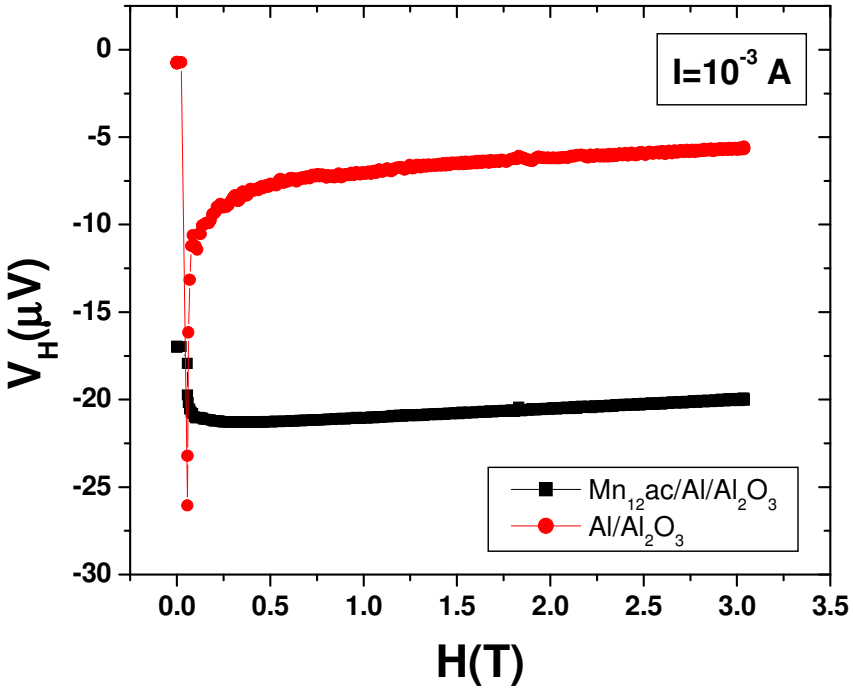

Fig. V-10 Continued.

Therefore, it may be possible that the magnetic field from the Mn_{12}-acetate layer assists the aluminum strip in becoming a normal metal under the influence of the current. As defined earlier, the Hall voltages V_{24} were measured flowing three different currents on each sample at 200mK and plotted as functions of applied magnetic field H from 0T to 3T in Fig. V-10. The relationship between the Hall voltage V_H ($=V_{24}$) and the applied magnetic field H is written by $R_H = V_H d/IB$, the definition of the Hall coefficient R_H where d is the thickness of the system, I is the transport current and B is the magnetic flux density imposed on the system. The first two graphs in Fig. V-10 show zero V_H before the first sharp transition at around 0.05~0.07T. After that, they fluctuate starting from big jumps and then reach to stable regions where the Hall voltages are matched in nearly straight lines, so that the Hall coefficients R_H are pertinently defined. The differences in the voltages between the two samples over the stable regions are mainly due to the misalignments of the legs in the patterned samples. It is found in the third graph that the Hall voltages start from non-zero values and this is because the measuring current (10^{-3}A) is already over the critical currents for the samples. More particularly, all these three graphs include an unstable region where the Hall voltages are not simply straight but wildly fluctuating depending on the strength of currents. Maybe, these regions are reflecting the abnormal motion of electrons in the mixed state where the distribution of the magnetic flux density is not clearly defined.

Thus far, the results from the first experiment to investigate the interaction between superconductors and SMMs have been described. Both samples show three distinct ranges of magnetic field where the materials are in normal, superconducting and the

mixed phase, and notably the resistances of the two samples in the mixed region are distinguishable from each other. However, there are still many things remaining unclear. The layer of Mn_{12}-acetate was created before the aluminum deposition to produce a coupled system in this first attempt. Due to the inhomogeneous surface of the Mn_{12}-acetate layer, this approach potentially produces an additional factor affecting the surface roughness of the aluminum film as well as the interface between the layers. The surface morphology could be a possible source to influence the magnetoresistance in various ways. The second experiment in which the indirectly coupled hybrid samples were examined eliminates this additional factor. Since the Mn_{12}-acetate was deposited later on top of the aluminum film pattern, the surface roughness of the primary systems (aluminum films) are not appreciably different from each other. By doing the second experiment with the inversely built sample, one not only can exclude any strong interface effects, but also can observe the interaction which is purely magnetic because the aluminum film will be naturally oxidized before the layer of Mn_{12}-acetate forms on it, separating the subsystem electronically from the aluminum film via the insulating layer.

Table V-1 shows V_{12}, V_{34}, and V_{14} of the two samples for the second control experiments measured at the room temperature (~300K), liquid nitrogen temperature (~77K), and liquid helium temperature (~4.2K), respectively, where the subscripts of V mean the legs in Fig. V-3. An AC-current of 10μA was used for the measurement and the voltages were measured in mV. Sample #1 was the pure aluminum film pattern and sample #2 was the hybrid system.

Table. V-1. The $V_{12,}$ $V_{34,}$ and V_{14} of the two samples measured at three different temperatures in a cooling process, where DAD means the dropping and drying process to deposit a Mn_{12}-acetate film.

	Room Temp. (300K)						Liquid Nitrogen Temp. (77K)			Liquid Helium Temp. (4.2K)		
	Before DAD			After DAD								
	V_{12}	V_{34}	V_{14}	V_{12}	V_{34}	V_{14}	V_{12}	V_{34}	V_{14}	V_{12}	V_{34}	V_{14}
#1	0.482	0.424	0.888	0.483	0.430	0.899	0.335	0.333	0.667	0.316	0.314	0.630
#2	0.477	0.480	0.955	0.485	0.500	0.977	0.350	0.352	0.703	0.331	0.333	0.663

In order for the two samples to have an identical background substance, a pure solvent (2-propanol) used to dissolve Mn_{12}-acetate powder was dropped and dried on the surface of sample #1, while the Mn_{12}-acetate solution was dropped and dried on sample #2. The voltages were measured twice at the room temperature (before and after the dropping and drying process). The different result between the two native aluminum film samples that is shown in the data acquired before the process is due to an additional conductive path on the substrate. Probably the naturally grown oxide layer at the top of the silicon substrate was not thick enough, therefore, when a lump of indium was pressed on the substrate to make the connection of a gold wire, the indium broke through the oxide layer making a contact with the silicon surface which is not a good insulator at room temperature. In addition the sum of V_{12} and V_{34} is different from voltage V_{14} for the same reason. However, the disagreement mostly disappeared when the experimental

temperature was lowered. It indicates that the additional conductive paths become insulating at low temperatures. The critical temperature of the samples was investigated. For the measurement an AC-measuring current, 10μA, was generated and the resistance of the calibrated germanium thermoresistor was monitored to define the experimental temperature. The resistances are shown in Fig. V-11 as a function of temperature. Both samples show the transition from a normal state to the superconducting state at the temperature of ~1.55K.

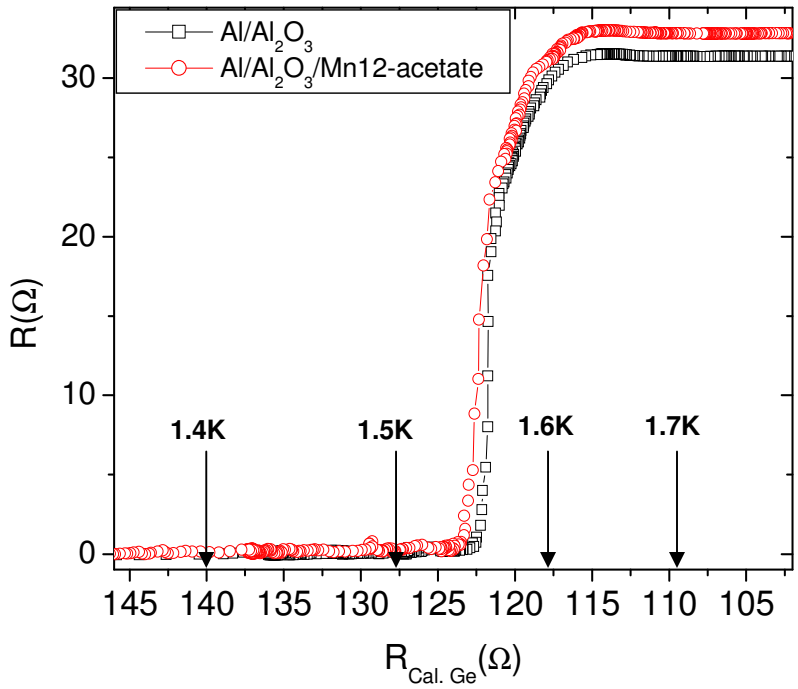

Fig. V-11. Longitudinal resistance R vs. temperature. The arrows including numbers indicate the temperatures converted from the resistance of the thermoresistor.

The longitudinal resistance of the samples obtained from V_{12} [See Fig. V-3] was measured at four different temperatures, 0.06K, 0.4K, 0.8K, and 1.0K. The resistance, R, was plotted as a function of the applied magnetic field H in Fig. V-12. The small magnet which was introduced in the previous chapter was employed. The measuring current was 10μA. The samples were mounted perpendicular to the direction of the magnetic field. For both of the samples it is observed that the resistances are fluctuating in the intermediate state particularly at a lower temperature. The critical magnetic fields decrease as the temperature increases. It is obvious that the critical magnetic fields of the aluminum film sample coupled with the Mn_{12}-acetate film are generally smaller than the critical field of the other sample. The resistances were measured with various measuring currents at the highest temperature (1.0K) [Fig. V-13]. For all of the cases the hybrid system shows the smaller critical fields than those of the pure aluminum sample. The magnetoresistances decrease as the measuring current is reduced. That is probably because of the motion (created by the current) of the magnetic flux lines formed through the system. As mentioned earlier, the resistivity attributing to the induced electric field by the motion of the magnetic flux lines is weakened as the current becomes less energetic. In this control experiment the vortex pinning effect by the magnetic clusters does not appear. It is quite possible that the additional magnetic flux lines from the molecular magnets are penetrating through the aluminum film making domains of a normal phase, hence the overall resistivity of the hybrid system is higher than of the pure aluminum film sample at a constant applied magnetic field. Magnetoresistances

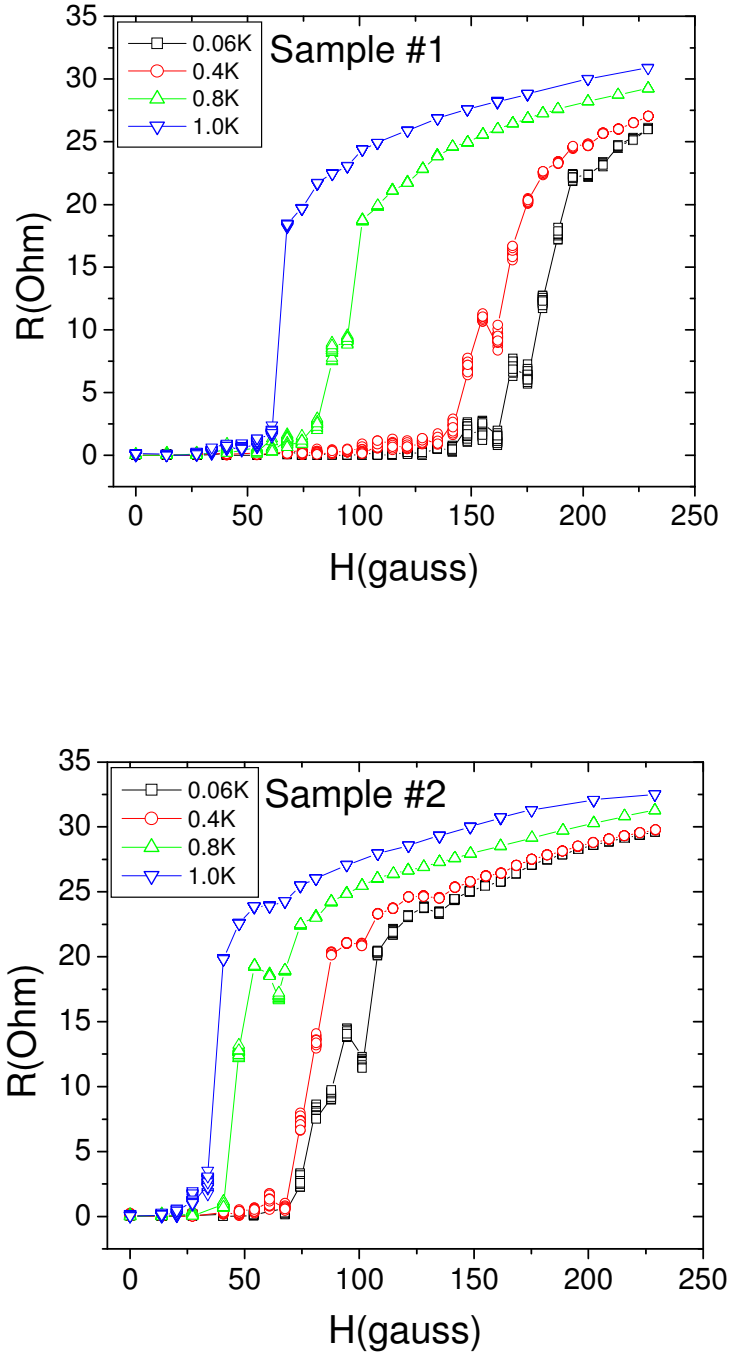

Fig. V-12. Longitudinal resistance R vs. magnetic field H up to ~230 gauss for the two samples measured at four different temperatures. (Sample #1: Pure aluminum film, Sample #2: Hybrid system)

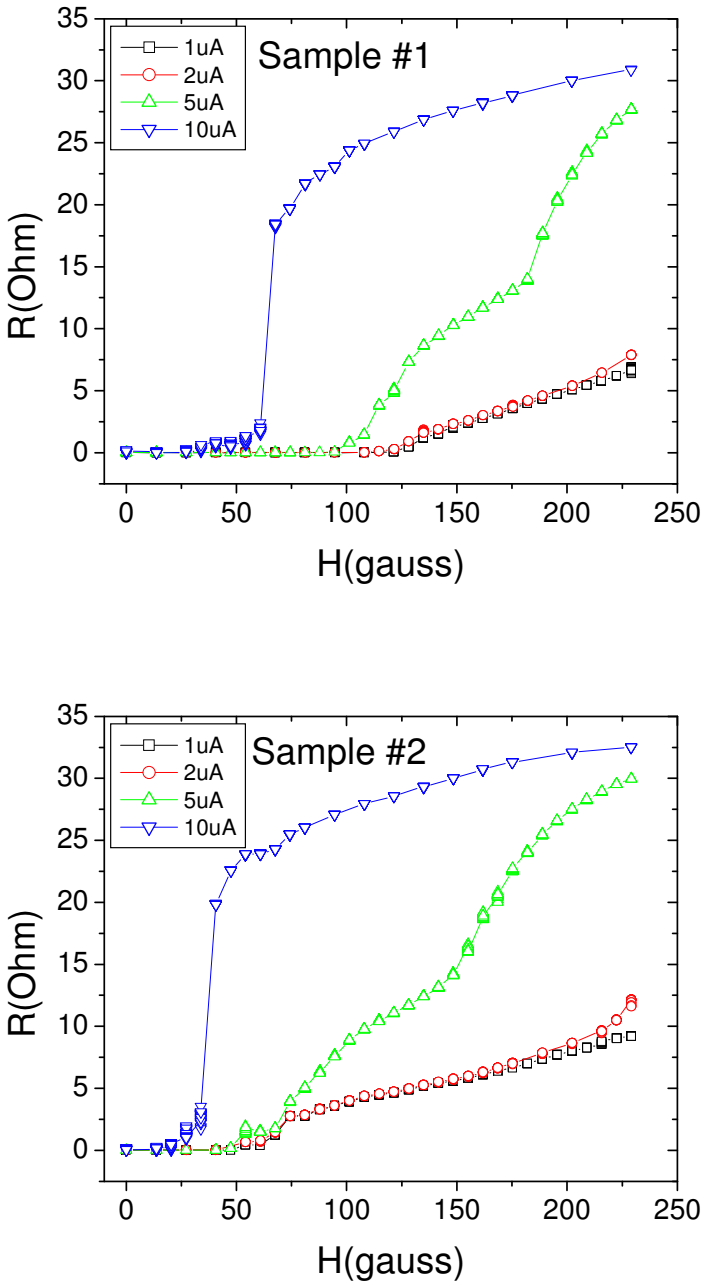

Fig. V-13. Longitudinal resistance R vs. magnetic field H up to ~230 gauss for the two samples measured with four different measuring currents. (Sample #1: Pure aluminum film, Sample #2: Hybrid system)

measured with the measuring current of 2μA are very close to the magnetoresistances measured with the current of 1 μA for both of the samples. More clearly, the critical fields where the samples start getting a resistive character are almost identical for the two measuring current. The observation of the experimental data concludes that a measuring current of 1 μA is suitable to define the critical magnetic field of the superconducting system. The maximum magnetic field (~230gauss) was not enough to transform the samples completely into a normal state. In order to examine the overall trend of the transition from the superconducting phase to the normal phase, the magnetic field was increased up to 700gauss. A power supply and a shunt resistor which could handle more current were used to increase the magnetic field. The magnetoresistances of the hybrid system are compared with the resistances of the pure aluminum sample in Fig. V-14. This data was acquired at 60mK with the measuring current of 1 μA. The magnetic field was increased step by step manually. It is observed that the hybrid system shows an earlier start of the transition and both of the samples transit to a normal state at almost the same magnetic field (~560gauss).

The maximal difference of thickness between the two aluminum films is estimated in order to investigate if it could be the cause of the difference in critical field. In the thermal thin film evaporation process one of the substrates was mounted ~30cm directly above the aluminum source and the other film was mounted right next to it at a distance of ~1cm. Since film thickness is inversely proportional to $r^2 \cos\theta$ where θ is the angle between the two straight lines which connect the source to the centers of the film

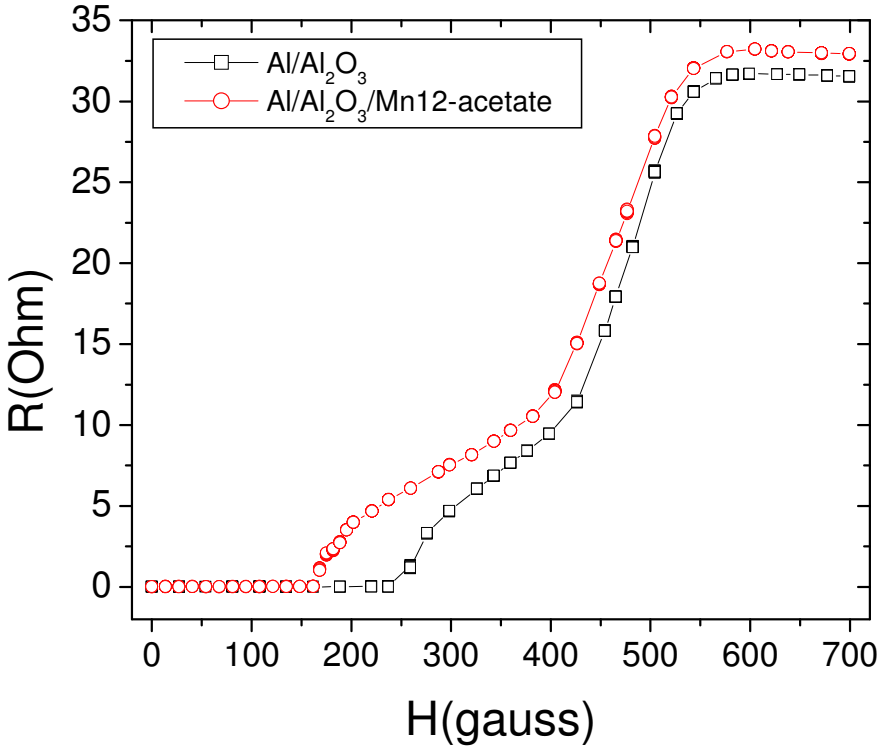

Fig. V-14. Longitudinal resistance R vs. magnetic field H up to 700 gauss for the two samples measured with a measuring current of 1 μA at 60mK.

patterns, the ratio of the thickness of a thinner film (d') to the thickness of a thicker film (d) is $d'/d = 0.9994$. From ref. [52] it results that the upper critical magnetic field (H_{c2}) is inversely proportional to the film thickness. Thus, the critical field discrepancy (~33.3%), which is shown in Fig. V-14, can not be explained by the potential thickness difference due to the thermal evaporation process.

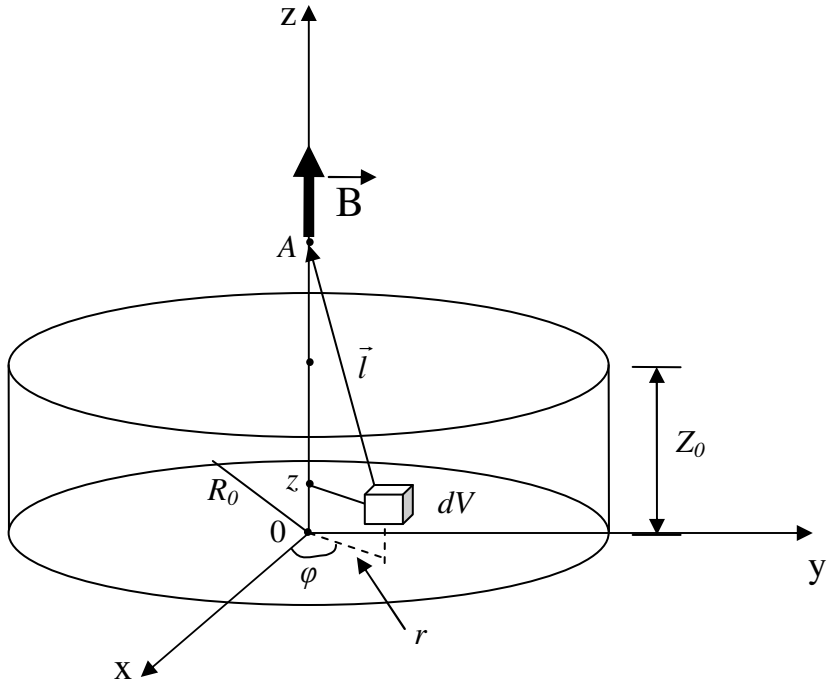

Fig. V-15. Magnetic flux density $\vec{B}$ at an arbitrary point *A* on the z-axis produced by a cylindrical single crystal which has the radius R_0 and the height Z_0.

In order to estimate the magnetic flux density produced by a Mn_{12}-acetate single crystal an idealized cylindrical crystal structure shown in Fig. V-15 was considered. The magnetic flux density $\vec{B}$ at an arbitrary point *A* on the z-axis is given by

$$\vec{B} = \frac{\mu_0}{4\pi} \int \frac{\{3\vec{l}\,(\hat{l} \cdot d\vec{\mu}) - d\vec{\mu}\}}{l^3} \qquad \text{(V-1)}$$

assuming that the spin of each single-molecule in the crystal is aligned to the z-axis. Namely, $d\vec{\mu} = \frac{20\mu_B}{\delta} \cdot dV\hat{z}$, where dV and δ are an infinitesimal volume and the unit volume for a single-molecule magnet, respectively. The expression of the magnetic flux density in cylindrical coordinates is then

$$\vec{B} = \frac{20\mu_B\mu_0}{4\pi\delta} \iiint \frac{\{3\vec{l}\,(\hat{l}\cdot\hat{z}) - \hat{z}\}}{l^3} r d\varphi dr dz \,. \tag{V-2}$$

The final result for the magnetic flux density is

$$\vec{B} = \frac{10\mu_B\mu_0}{\delta} \left\{ \frac{A}{\sqrt{A^2 + R_0{}^2}} - \frac{(A - Z_0)}{\sqrt{(A - Z_0)^2 + R_0{}^2}} \right\} \hat{z} \,. \tag{V-3}$$

This result is plotted in Fig. V-16 as a function of R_0. We assume that $\delta = 8\times10^{-27}\, m^3$, $A = Z_0 + 5nm$, and $Z_0 = R_0$, hence the graph indicates the magnetic flux density at the point 5*nm* above the center of the cylindrical single crystal (5*nm* was chosen because the thickness of the aluminum film in the hybrid system was ~10*nm*). It is recognized from the graph in Fig. V-16 that the magnetic flux density is almost saturated at a crystal size R_0=200*nm* and the saturated value is ~100 gauss which is about forty times bigger than the value from a single-molecule (~3 gauss). A crystal which has a size of R_0=10*nm* creates ~56 gauss at the surface [inset in Fig. V-16].

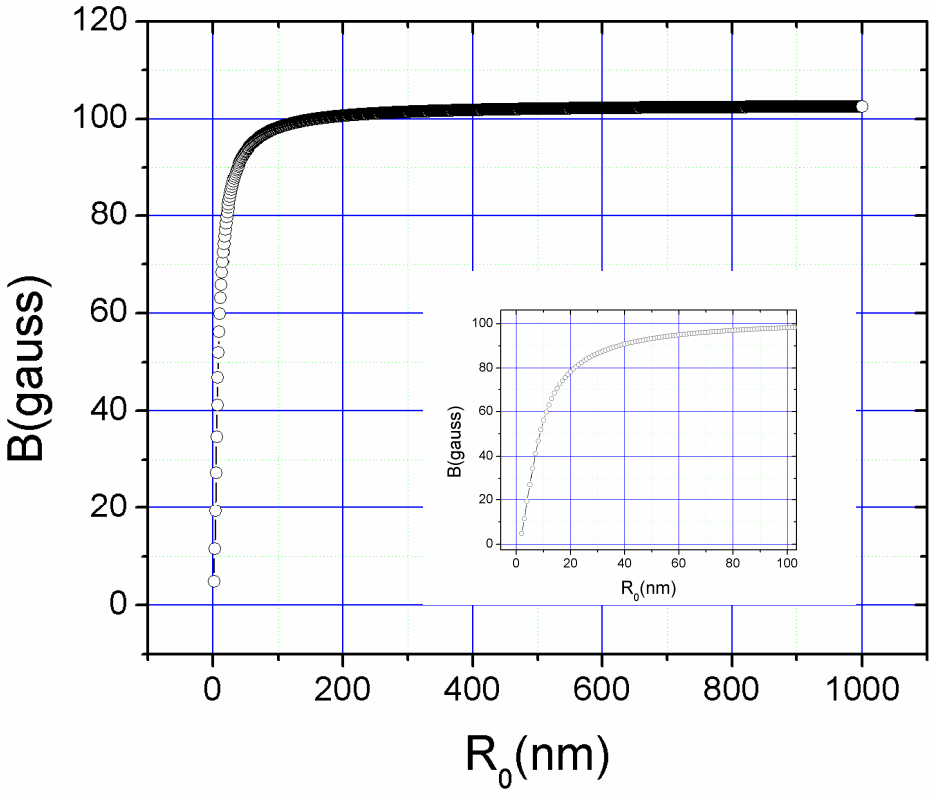

Fig. V-16. Magnetic flux density $\vec{B}$ at 5*nm* above the surface of a single crystal vs. the size of the crystal.

These magnetic fields are comparable to the difference in critical field discussed earlier, which is ~80 gauss, i.e. the hybrid sample had a critical field about 80 gauss smaller than the bare aluminum film sample [Fig. V-14]. This estimation concludes that, unlike a single-molecule, oriented single crystals and conglomerates of dozens of molecules which are possibly contained in the magnetic layer could be the source that suppresses the superconductivity of the aluminum film.

CHAPTER VI

SUMMARY AND DISCUSSION

The main purpose of this research project is to develop a means to manipulate Mn_{12}-acetate SMMs for the application and further study of the unusual magnetic system. The multiple transitions in the magnetic hysteresis, the slow relaxation process, and the well defined size of the molecular magnet unit attract scientists because of the possible application, such as quantum computation, ultra high density magnetic information storage device, and molecular electronics. Therefore, it has been an important common topic for the scientific community to invent a suitable way to localize and to control the molecular magnets for this purpose. A simple and reliable technique to create an artificial structure of Mn_{12}-acetetate thin film on a Si/SiO_2 substrate has been introduced in this dissertation. The solution evaporation technique to generate a Mn_{12}-acetetate thin film combined with conventional lithography, such as Photo-lithography and EBL, allows us to minimize the width of the film structure down to about 50 nm. By a series of analyses performed with AFM, XPS, and SQUID magnetometry, we studied the nature of the resulting materials of which the film patterns were made, and the studies proved that the materials in the film structure were intact SMMs. Nowadays many devices are created on silicon surfaces using EBL not only for commercial purpose, but also for a fundamental study. The technique introduced in this dissertation is comparable with the modern process, thus it will provide a useful tool for the further development of SMMs.

Although the various analyses prove the reliability of this new patterning process for the unusual magnetic material, the ultimate completion of this research project must be with any direct observation of the novel magnetic properties from the artificial structures. For the purpose aluminum film SQUIDs having a loop area of $1\times1\mu m^2$ were developed using EBL and thermal evaporation. It has been demonstrated that the measuring critical current on the device measured at a temperature far below the critical temperature of bulk aluminum oscillates depending on the magnetic flux inside the SQUID loop as expected from the theory. A proper experimental setup for future study of SMM film structures has been introduced. In the experimental configuration the critical current is coupled with the magnetic flux lines generated by the Mn_{12}-acetate film, thus it is possible to examine the magnetic state of the film structure. The inconsistency between the theory and the practical data has suggested additional experiments. With these additional efforts this SQUID project will provide a suitable system in which a more rigorous study of the Mn_{12}-acetate film patterns is possible

The study to investigate the interaction between aluminum superconducting films and SMMs has been presented in the previous chapter. An effect of a Mn_{12}-acetate film on the superconductivity of an aluminum film was observed. For this investigation magnetoresistance, critical current, Hall voltage, critical magnetic field, and critical temperatures of the Hybrid systems were measured at various temperatures, and they were compared with the results from the pure aluminum films. Several interesting phenomena appeared in the hybrid system. The results, such as appreciably fluctuating magnetoresistance in the intermediate state of the superconductor and a lowered critical

magnetic field, propose two potential areas for future research. One is the influence of the SMMs on the low-dimensional superconducting device's functionality and the second is the basic physics of superconductivity in the presence of SMMs, a new type of magnetic system.

REFERENCES

[1] T. Lis, Acta Cryst. B **36**, 2042 (1980).

[2] R. Sessoli, D. Gatteschi, A. Caneschi and M. A. Novak, Nature **365**, 141 (1993).

[3] A. Caneschi, D. Gatteschi, C. Sangregorio, R. Sessoli, L. Sorace, A. Cornia, M. A. Novak, C. Paulsen and W. Wernsdorfer, J. Magn. Magn. Mater. **200**, 182 (1999).

[4] B. Barbara, L. Thomas, F. Lionti, I. Chiorescu and A. Sulpice, J. Magn. Magn. Mater. **200**, 167 (1999).

[5] J. M. North, L. J. van de Burgt and N. S. Dalal, Solid State Commun. **123**, 75 (2002).

[6] D. Gatteschi and R. Sessoli, Angew. Chem. Int. Ed. **42**, 268 (2003).

[7] J. M. Hernandes, X.X. Zhang, F. Luis, J. Tejada, J. R. Friedman, M. P. Sarachik, and R. Ziolo, Phys. Rev. B. **55**, 5858 (1997).

[8] C. Paulsen and J. G. Park, in *Quantum Tunneling of Magnetization*, edited by L. Gunther and B. Barbara (Kluwer, Dordrecht, The Netherlands 1995), p. 189.

[9] E. M. Chudnovsky, Science **274**, 938 (1996).

[10] J. R. Friedman and M. P. Sarachik, J. Tejada and R. Ziolo, Phys. Rev. Lett. **76**, 3830 (1996).

[11] W. Wernsdorfer, R. Sessoli, Science **284**, 133 (1999).

[12] L. Thomas, F. Lionti, R. Ballou, D. Gatteschi, R. Sessoli, and B. Barbara, Nature **383**, 145 (1996).

[13] E. del Barco, A. D. Kent, E. M. Rumberger, D. N. Hendrickson, and G. Christou, Europhys. Lett. **60**, 768 (2002).

[14] M. A. Novak and R. Sessoli, in *Quantum Tunneling of Magnetization*, edited by L. Gunther and B. Barbara (Kluwer, Dordrecht, The Netherlands 1995), p. 171.

[15] L. Thomas, A. Caneschi, and B. Barbara, Phys. Rev. Lett. **83**, 2398 (1999).

[16] M. N. Leuenberger, D. Loss, Nature **410**, 789 (2001).

[17] L. Krusin-Elbaum, T. Shibauchi, B. Argyle, L. Gignac, D. Weller, Nature **410**, 444 (2001).

[18] E. Del Barco, N. Vernier, J. M. Hernandez, J. Tejada, E. M. Chudnovsky, E. Molins and G. Bellessa, Europhys. Lett. **47**, 722 (1999).

[19] J. Tejada, E. M. Chudnovsky, E. Del Barco, J. M. Hernandez, and T. Spiller, Nanotechnology **12**, 181 (2001).

[20] G. -H. Kim and T. -S. Kim, Phys. Rev. Lett. **92**, 137203 (2004).

[21] H. B. Heersche, Z. de Groot, J. A. Folk, H. S. J. van derZant, C. Romeike, M. R. Wegewijs, L. Zobbi, D. Barreca, E. Tondello, and A. Corina, Phys. Rev. Lett. **96**, 206801 (2006).

[22] M.-H. Jo, J. E. Grose, K. Baheti, M. M. Deshmukh, J. J. Sokol, E. M. Rumberger, D. N. Hendrickson, J. R. Long, H. Park, and D. C. Ralph, Nano Lett. **6**, 2014 (2006).

[23] M. Cavallini, F. Biscarini, J. Gomez-Segura, D. Ruiz, and J. Veciana, Nano Lett. **3**, 1527 (2003).

[24] D. Ruiz-Molina, M. Mas-Torrent, J. Gomez, A. I. Balana, N. Domingo, J. Tejada, M. T. Martinez, C. Rovira, and J. Veciana, Adv. Mater. **15**, 42 (2003).

[25] A. Cornia, A. C. Fabretti, M. Pacchioni, L. Zobbi, D. Bonacchi, A. Caneschi, D. Gatteschi, R. Biangi, U. D. Pennino, V. D. Renzi, L. Gurevich and H. S. J. Van der Zant, Angew. Chem. Int. Ed. **42**, 1645 (2003).

[26] M. Clemente León, H. Soyer, E. Coronado, C. Mingotaud, C. J. Gómez-García and P. Delhaès, Angew. Chem. Int. Ed. **37**, 2842 (1998).

[27] M. Cavallini, J. Gomez-Segura, D. Ruiz-Molina, M. Massi, C. Albonetti, C. Rovira, J. Veciana, and F. Biscarini, Angew. Chem. **117**, 910 (2005).

[28] E. Coronado, A. Forment-Aliaga, F. M. Romero, V. Corradini, R. Biagi, V. De Renzi, A. Gambardella, and U. del Pennino, Inorg. Chem. **44**, 7693 (2005)

[29] J. Gómez-Segura, O. Kazakova, J. Davies, P. Josephs-Franks, J. Veciana and D. Ruiz-Molina, Chem. Commun.**45**, 5615 (2005)

[30] M. Mannini, D. Bonacchi, L. Zobbi, F. M. Piras, E. A. Speets, A. Caneschi, A. Cornia, A. Magnani, B. J. Ravoo, D. N. Reinhoudt, R. Sessoli, and D. Gatteschi, Nano Lett. **5**, 1435 (2005).

[31] M. Cavallini, J. Gomez-Segura, C. Albonetti, D. Ruiz-Molina, J. Veciana, and F. Biscarini, J. Phys. Chem. B. **110**, 11607 (2006).

[32] J. Means, R. Srivastava, V. Meenakshi, W. Teizer, H. Zhao, K. Dunbar, A. Kolomenskii and H. A. Schuessler, J. Mag. Mag. Mat. **284**, 215 (2004).

[33] V. Meenakshi, W. Teizer, D. Naugle, H. Zhao and K. Dunbar, Solid State Comm. **132**, 471 (2004).

[34] D. M. Seo, M. Viswanathan, W. Teizer, H. Zhao, K. Dunbar, J. Mag. Mag. Mat. **301**, 31 (2006).

[35] M. A. McCord and M. J. Rooks, in *Handbook of Microlithography, Micromachining and Microfabrication*, edited by P. Ray-Choudhury (SPIE, London, 1997), Vol. 1. p. 139

[36] R. D. Deegan, O. Bakajin, T. F. Dupont, G. Huber, S. R. Nagel and T. A. Witten, Nature **389**, 827 (1997).

[37] J. S. Kang, J. H. Kim, Y. J. Kim, W. S. Jeon, D. Y. Jung, S. W. Han, K. H. Kim, K. J. Kim, B. Kim, J. Korean Phys. Soc. **40**, L402, (2002).

[38] A. C. Rose-Innes and E. H. Rhoderick, *Introduction to Superconductivity*, 2nd Ed. (Pergamon, Oxford, 1978), p. 153.

[39] C. Kittel, *Introduction to Solid State Physics*, 7th Ed. (Wiley, New York, 1996), p. 334.

[40] M. Tinkham, *Introduction to Superconductivity*, 2nd Ed. (Dover Publications, Inc., New York, 2004), p. 196.

[41] R. P. Feynman, *Lectures on Physics-III*, 11th Printing (Addison-Wesley, Reading, Massachusetts, 1979), p. 21-1.

[42] K. Hasselbach, D. Mailly, and J. R. Kirtley, J. Appl. Phys. **91**, 4432 (2002).

[43] F. Pobell, *Matter and Methods at Low Temperatures*, 2nd Ed. (Springer, Heidelberg,1996).

[44] G. K. White and P. J. Meeson, *Experimental Techniques in Low-Temperature Physics*, 4th Ed. (Oxford Science Publications, New York, 2002).

[45] J. P. Carbotte and R. C. Dynes, Phys. Lett. **25A**, 685 (1967)

[46] R. B. Pettit, Phys. Rev. B **13**, 2865 (1976).

[47] W. Wernsdorfer, K. Hasselbach, D. Mailly, B. Barbara, A. Benoit, L. Thomas, and G. Suran, J. Mag. Mag. Mat. **145**, 33 (1995).

[48] P. M. Tedrow and R. Meservey, Phys. Rev. B **25**, 171 (1982).

[49] I. F. Lyuksyutov, and V. L. Pokrovsky, Ferromagnet-Superconductor Hybrids (2004). http://arxiv.org/abs/cond-mat/0409137

[50] L.N. Bulaevskii, E.M. Chudnovsky, and M.P. Maley, Appl. Phys. Lett. **76**, 2594 (2000).

[51] A. Garcı´a-Santiago, F. Sa´nchez, M. Varela, and J. Tejada, Appl. Phys. Lett. **77**, 2900 (2000).

[52] M. Lange, M.J. Van Bael, V.V. Moshchalkov, and Y. Bruynseraede, Appl. Phys. Lett. **81**, 322 (2002).

[53] Y. Otani, B. Pannetier, J.P. Nozie`res, and D. Givord, J. Magn. Magn. Mater. **126**, 622 (1993).

[54] J.I. Martı´n, M. Ve´lez, J. Nogue´s, and I.K. Schuller, Phys. Rev. Lett. **79**, 1929 (1997).

[55] M. J. Van Bael, K. Temst, V.V. Moshchalkov, and Y. Bruynseraede, Phys. Rev. B **59**, 14 674 (1999).

[56] M. Tinkham, Phys. Rev. **129**, 2413 (1963).

[57] F. E. Harper and M. Tinkham, Phys. Rev. **172**, 441 (1968).

[58] B. L. Brandt, R. D. Parks and R. D. Chaudhari, J. Low Temp. Phys. **4**, 41 (1971).

[59] C. Veauvy, K. Hasselbach and D. Mailly, Phys. Rev. B **70**, 214513 (2004).

APPENDIX A

THE SCHEMATIC PHASE DIAGRAM OF LIQUID HELIUM MIXTURES (FROM REF .[44])

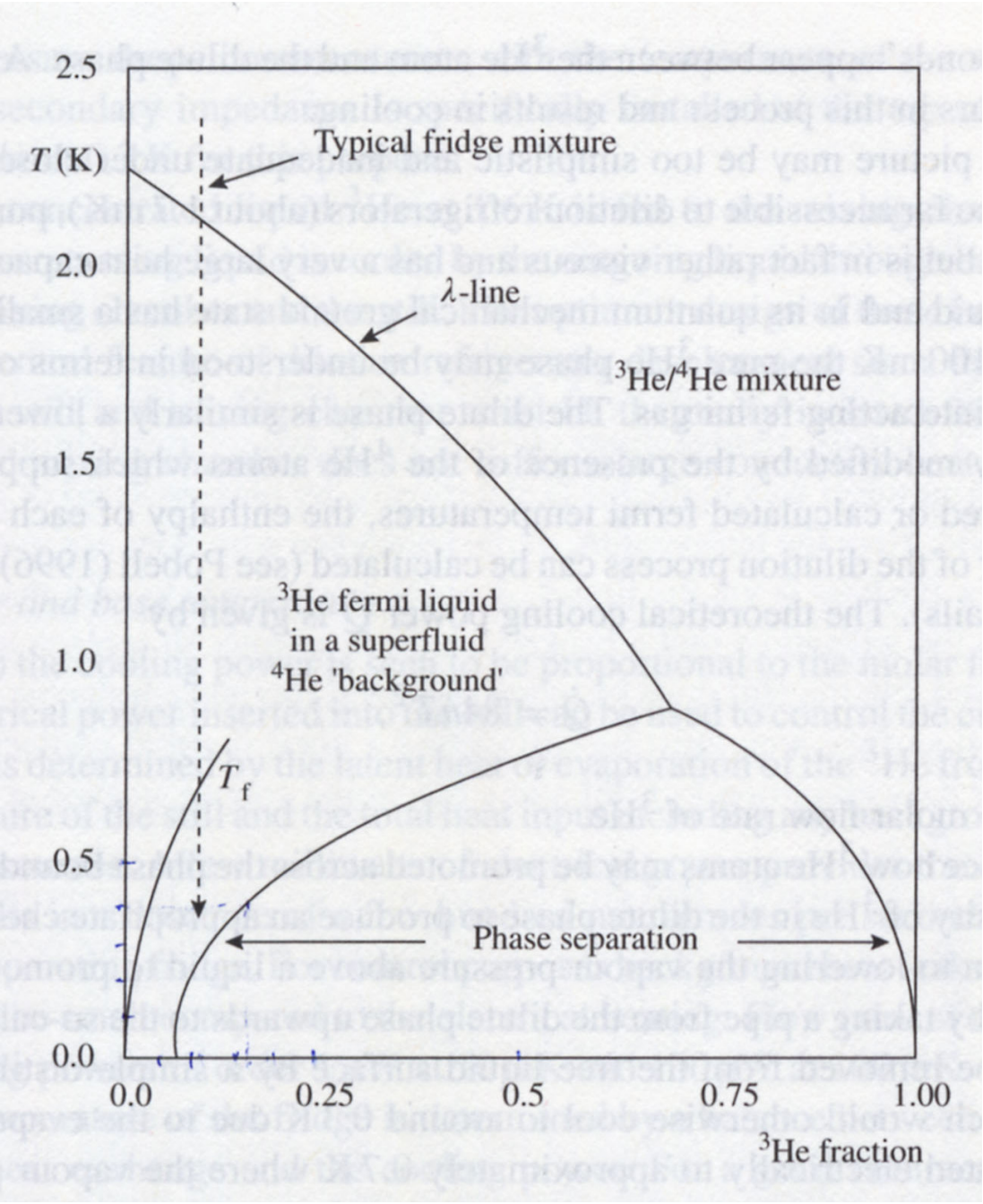

APPENDIX B

THE BLOCK DIAGRAM OF THE CRITICAL CURRENT MEASUREMENT BOX.

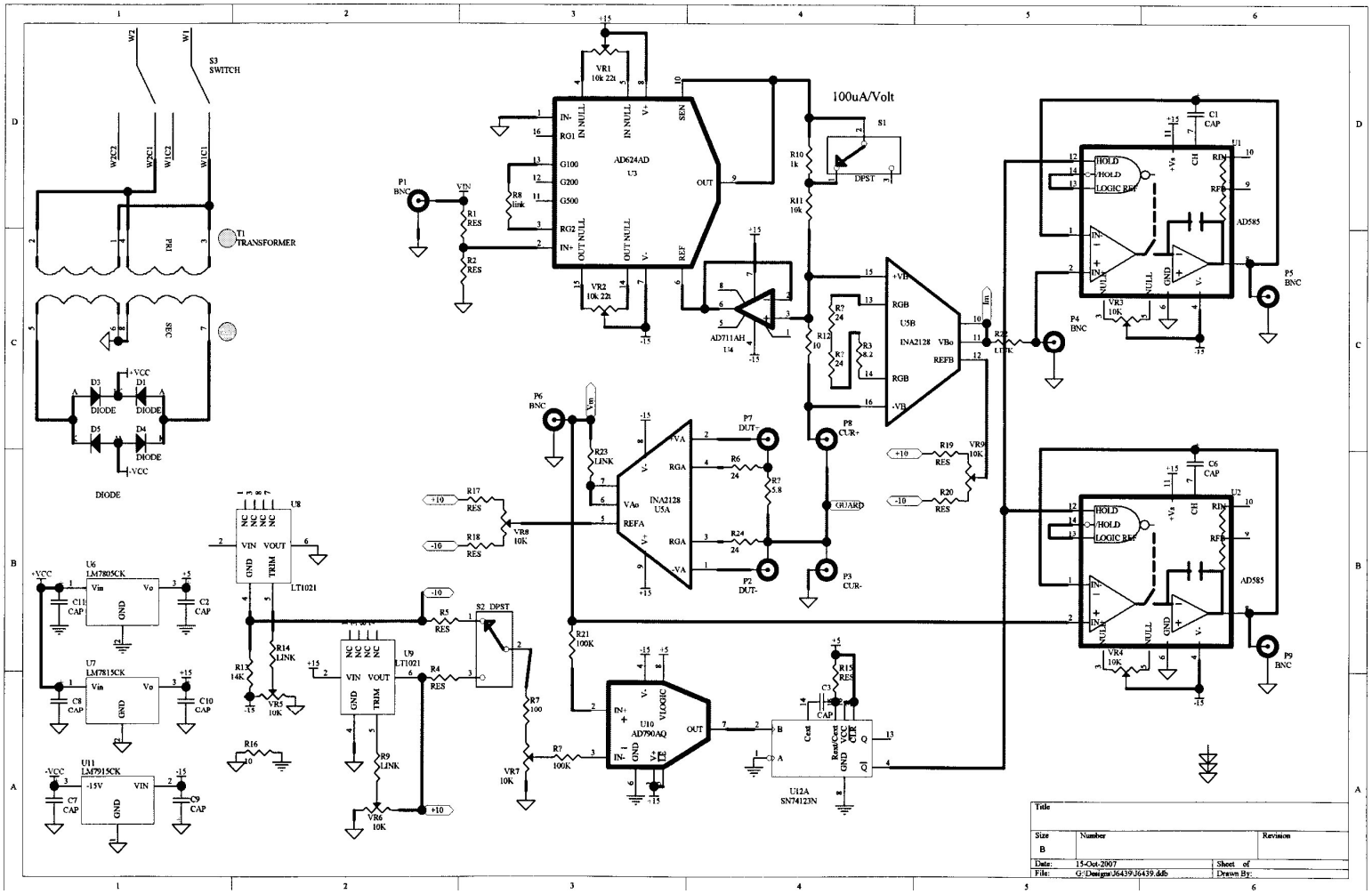

VITA

Kyongwan Kim was born in Seoul, Korea. He is the son of Mr. Dae-sung Kim and Ms. Ok-sun Lee.

The author entered Dankook University in March 1992 and majored in physics. He joined the military service in the Korean Army for three years from 1994 to 1996. Upon completion of a Bachelor of Science in February 1999, the author began his Master of Science program under the direction of Dr. Young-Jae Lee at Dankook University. The author received his Master of Science in physics, with an emphasis in electron-phonon interaction in ternary mixed crystal, in February 2001.

The author began his doctoral program in September 2001. He conducted his research program under the direction of Dr. Winfried Teizer, and received his Ph.D. degree in December 2007, from Texas A&M University.

Department of Physics

c/o Dr. Winfried Teizer

Texas A&M University

College Station, TX 77843-4242